

**Surface and Interface Engineering of Conjugated Polymers and Nanomaterials
in Applications of Supercapacitors and Surface-Functionalization**

Dissertation by

Yuanfang Hou

In Partial Fulfillment of the Requirements

For the Degree of

Doctor of Philosophy

King Abdullah University of Science and Technology

Thuwal, Kingdom of Saudi Arabia

© *May 2016*

Yuanfang Hou

All Rights Reserved

The dissertation of Yuanfang Hou is approved by the examination committee.

Committee Chairperson: Prof. Pierre Beaujuge

Committee Member: Prof. Osman Bakr

Committee Member: Prof. Yu Han

Committee Member: Prof. Zhonghai Zhang

ABSTRACT

Surface and Interface Engineering of Conjugated Polymers and Nanomaterials in Applications of Supercapacitors and Surface-Functionalization

Yuanfang Hou

In this dissertation, three aspects about surface and interface engineering of conjugated polymers and nanomaterials will be discussed.

(i) There is a significant promise for electroactive conjugated polymers (ECPs) in applications of electrochemical devices including energy harvesting, electrochromic displays, etc. Among these, ECPs has also been developed as electroactive materials in electrochemical supercapacitors (ESCs). Compared with metal oxides, ECPs are attractive because they have good intrinsic conductivity, low band-gaps, relatively fast doping-and-undoping process, the ease of synthesis, and tunable electronic and structural properties through structural modifications.

Here, Multiple-branch-chain 3,4-ethylenedioxythiophene (EDOT) derivatives was designed as crosslinkers in the co-electropolymerization of EDOT to optimize its morphology and improve the cycling stability of PEDOT in the supercapacitor applications. High-surface-area π -conjugated polymeric networks can be synthesized via the electrochemical copolymerization of the 2D (trivalent) motifs benzo[1,2-b:3,4-b':5,6-b'']trithiophene (BTT) and tris-EDOT-benzo[1,2-b:3,4-b':5,6-b'']trithiophene (TEBTT) with EDOT. Of all the material systems studied, P(TEBTT/EDOT)-based frameworks

achieved the highest areal capacitance with values as high as 443.8 mF cm^{-2} (at 1 mA cm^{-2}), higher than those achieved by the respective homopolymers (PTEBTT and PEDOT) in the same experimental conditions of electrodeposition (PTEBTT: 271.1 mF cm^{-2} (at 1 mA cm^{-2}); PEDOT: 12.1 mF cm^{-2} (at 1 mA cm^{-2}).

(ii) In electrochemical process, the suitable choice of appropriate electrolytes to enlarge the safe working potential window with electrolyte stability is well known to improve ECPs' performance in ESCs applications. Ionic liquids (ILs) are ion-composed salts and usually fluid within a wide temperature range with low melting points. There are many unique characteristics for these intrinsic ion conductors, including high ionic conductivity, wide electrochemical voltage windows in neutral conditions, fast ion mobility in redox reaction process ($>10^{-14} \text{ m}^2 \text{ V}^{-1} \text{ s}^{-1}$), low vapor pressure, and environmental stability. These properties qualified ambient-temperature ILs to be applied as supporting medium for various devices and materials processing applications in both industry and academia, overcoming the limitation of volatile organic compounds (VOCs). Especially, ILs have been utilized as superior medium to electrodeposit metals, alloys, semiconductors and ECPs in the application of supercapacitors.

Electropolymerization of EDOT and its derivative 4,4'-dimethoxy-3,3'-bithiophene (BEDOT) have been studied in three kinds of imidazolium-based ionic liquids and conducting salt in VOCs with different anions both as the growth medium and the supporting electrolyte, to assess the influence of these anions on their morphology and electrochemical activity. It is found these thiophene polymers grown in ILs with higher viscosity and lower diffusion shows much slower growth rate and orderly morphologies

than in Tetrabutylammonium hexafluorophosphate (TBAPF₆) dissolved in acetonitrile (ACN), and gives better electrochemical performance via cyclic voltammetry (CV) and galvanostatic charge-and-discharge (CD) studies. Polymers displayed multiple redox peaks in several cases, the possible reasons and origins are discussed. The synthesized polymer can be affected greatly by both the ILs with different anion/cation, and its mutual interaction with targeted monomer.. As far as known, there is no systematic study on how the anions of ILs and common organic solution could play a role as a medium both for polymerization and post-polymerization electrolyte for PEDOT and its derivatives. This study can be used as an easy reference and provide experimental diagnostic data when selecting ionic liquids to investigate and optimize thiophene-based electrochemical systems, such as batteries and supercapacitors.

(iii) Another aspect about interface chemistry of direct functionalization of nanodiamond with maleimide has also been addressed. Functional nanodiamonds are promising candidates for extensive practical applications in surface science, photonics and nanomedicine. Here, a protocol of direct functionalization is described by which maleimide-derivatized substituents can be appended to the outer shell of thermally annealed nanodiamonds through Diels-Alder reaction. This protocol can be carried out in room temperature, ambient atmosphere, without catalyst, and provide functionalized nanodiamonds with good solubility in organic solution. Also, this method can be applied for other maleimide derivatives, e.g. maleimide-fluorescence, which can be applied in fluorescence labeling, sensing, and drug delivery. A series of techniques, especially Fourier transform infrared spectroscopy (FTIR), and Solid State Nuclear Magnetic Resonance

(SS-NMR) was conducted for the analysis of surface chemistry and the investigation of the two-point binding strategy in details.

ACKNOWLEDGEMENTS

I would like to express my sincere gratitude to my advisor Prof. Pierre Beaujuge for the continuous support of my Ph.D study and related research.

I would like to thank the rest of my committee members: Prof. Osman Bakr, Prof. Yu Han, and Prof. Zhonghai Zhang, for your kindly guidance, time and patience to go through my dissertation and offer helpful feedbacks.

My sincere thanks also goes to all of the group members, lab colleagues and classmates for your valuable help, support and encouragement in the past and nowadays: Dr. Omar El Tall, Dr. Inam Ulhaq Raja, Dr. Abdulrahman El Labban, Dr. Dr. Adrien Lignie, Dr. Andreas Ringk, Dr. Clément Cabanetos, Dr. Julien Warnan, Dr. Shiming Zhang, Dr. Somnath Dey, Dr. Jannic Wolf, Dr. Hoang X. Dang, Dr. Shengjian Liu, Dr. Kai Wang, Dr. Philipp Wucher, Dr. Daniela Carja, Dr. Qasim Saleem, Dr. Zhipeng Kan, Dr. Yuliar Firdaus, Mr. Yangqin Gao, Mr. Wei Peng, Mr. Federico Cruciani, Mr. Ruze Liang, Mr. Maxime Babics; Dr. Rémi Mahfouz, Dr. Jun Pan, Mr. Wei Peng, Mr. Lutfan Sinatra, Mr. Jiakai liu, Mrs. Lina Abdul Halim, Mrs. Ala'a Ossama El-Ballouli in the group of Prof. Osman Bakr; Dr. Edy Abou-Hamad in KAUST Catalysis Center; Dr. Doddahalli H Nagaraju, Dr. Wei Chen, Mr. Chuan Xia in the group of Prof. Husam N. AlShareef; Mr. Jianfeng Huang in the group of Prof. Yu Han; Mr. Hanlin Hu in the group of Aram Amassian; Mrs. Le Shi in the group of Prof. Peng Wang.

My gratitude needs to go to the people in the KAUST core labs and HSE Safety team. I appreciate it very much that they offered me with kind help and precious support for laboratory and research facilities: Dr. Xianbin Wang, Dr. Kun Li, Dr. Zhihong Wang, Dr. Rachid Sougrat, Dr. Mohamed N. Hedhili, Dr. Ali Reza Behzad, Dr. Dalaver H. Anjum, Dr. Wei Xu, Dr. Liang Li, Dr. Kazuo Yamauchi, Dr. Xianrong Guo, Dr. Zaibing Guo, Dr. Jingqi Li, Dr. Yingbang yao, Dr. Lan Zhao, Dr. Yang Yang, Dr. Tan Hua, Dr. Long Chen, Dr. Jun Li, Dr. Chao Zhao, Dr. Yao He, Dr. Sheng Li, Mr. Elhadj Marwane Diallo, Mr. Qiang Zhang, Mr. Salim Sioud and Ms. Ebtihaj Bukhari.

I would like to dedicate my love to my parents and my family, for their care, love, support, encouragement and the substantial influence on me.

Finally, I would like to give my sincerely thanks to who has worked or has been working in KAUST, who has supported or has been supporting this campus, who has companied or has been companying with me. Days in KAUST will always be memorized and I wish you all of the best.

TABLE OF CONTENTS

ABSTRACT	3
ACKNOWLEDGEMENTS	7
TABLE OF CONTENTS	9
LIST OF ABBREVIATIONS	12
LIST OF SCHEMES	15
LIST OF FIGURES	16
LIST OF TABLES	26
Chapter 1	27
Introduction and Background	27
1.1 Energy Reality and Energy Storage Demanding.....	27
1.2 Electrochemical energy storage: batteries and supercapacitors	28
1.2.1 Classification of Energy Storage Techniques.....	28
1.2.2 Classification of Capacitors.....	30
1.2.3 Classification and General Properties of Supercapacitors.....	32
1.3 Techniques to Synthesis Electronically Conducting Polymer Electrodes for Supercapacitors	38
1.3.1 Chemically oxidation.....	38
1.3.2 Electrochemical polymerization	39
Chapter 2	44
Multiple-Branch-Chain 3, 4-Ethylenedioxythiophene Derivatives Designed as Crosslinkers in the co-Electropolymerization of EDOT Yields High Capacitance ..	44
2.1 Introduction of Conducting Polymers and EDOT in Supercapacitor Applications	44

2.2 9,9'-Spirobi[9H-fluorene] 3, 4-Ethylenedioxythiophene Derivative as Crosslinker in the co-Electropolymerization of EDOT	48
2.2.1 Experimental Section.....	50
2.2.2 Results and Discuss	52
2.2.3 Conclusion	72
Chapter 3	74
How Doping Influences EDOT and its Derivative's Electrochemical Properties – the role of anions in the Electropolymerization process.....	74
3.1 Introduction and Background.....	74
3.2 The Study on Electropolymerization of EDOT and BEDOT and the Post-polymerization Electrochemical Properties	79
3.2.1 Experimental Section.....	79
3.2.2 Results and Discussion	81
3.2.3 Conclusion	98
Chapter 4	99
Direct Functionalization of Nanodiamonds with Maleimide	99
4.1 Introduction	99
4.2 Experimental Section	100
4.2.1 Preparation of the Nanoparticle Precursors	100
4.2.2 Characterization of the Nanoparticle Precursors	102
4.2.3 Synthesis of the Maleimide EHM	103
4.2.4 Functionalization Procedure	105
4.2.5 SS-NMR Analyses.....	106
4.2.6 Preparation and Characterization of F5M-GDNPs.....	107
4.3 Results and Discussion on Direct Functionalization of Nanodiamond with Maleimide.....	109
4.3.1 Thermal Annealing and Characterization of detonation diamond nanoparticles (DDNPs)	109
4.3.2 Functionalization of Annealed DDNPs with Maleimide.....	111

4.3.3 Binding Strategy Investigation through Solid-state NMR (SS-NMR).....	116
4.3.4 Functionalization of Annealed DDNPs with Maleimide-derivatized Fluorescein Dye.....	121
4.4 Conclusion.....	124
REFERENCES.....	126
PUBLICATIONS	153

LIST OF ABBREVIATIONS

[bmim][PF ₆]	1-butyl-3-methylimidazolium hexafluorophosphate
[bmim][Tf ₂ N]	1-Butyl-3-methylimidazolium bis(trifluoromethylsulfonyl)imide
[bmim][TfO]	1-Butyl-3-methylimidazolium trifluoromethanesulfonate
0D	zero-dimensional
1D	one-dimensional
2D	two-dimensional
3D	three-dimensional
AC	activated carbon
BTT	Benzo[1,2-b:3,4-b':5,6-b'']trithiophene
CD	galvanostatic charge-discharge
CE	counter electrode
CNT	carbon nanotube
CP	Carbon paper
CV	cyclic voltammetry
DDNPs	detonation diamond nanoparticles

ECP	electroactive conjugated polymers
ECSs	Electrochemical supercapacitors
EDLC	electrochemical double layer capacitor
EES	Electrochemical energy storage
PEDOT	poly(3,4-ethylenedioxythiophene)
ESR	equivalent series resistance
FS	faradaic supercapacitors
GC	glassy carbon
ITO	indium tin oxide
PAni	polyaniline
PPy	polypyrrole
PTp	polythiophene
RE	reference electrode
RT	room temperature
SEM	scanning electron microscopy
SSA	specific surface area

TBAP	tetrabutylammonium perchlorate
TBAPF ₆	tetrabutylammonium hexafluorophosphate
TEBTT	tris-EDOT-benzo[1,2-b:3,4-b':5,6-b'']trithiophene
TEM	transmission electron microscopy
TGA	thermo gravimetric analysis
WE	working electrode
XPS	X-ray photoelectron spectroscopy
XRD	X-ray diffraction

LIST OF SCHEMES

Scheme 1.1 Chemical oxidation process of EDOT and the doping process of PEDOT polymer.⁴³

Scheme 3.1 Positive Doping/De-doping Process of PEDOT in [bmim][Tf₂N].

LIST OF FIGURES

Figure 1.1 Classification of Electrical Energy Storage Methods.

Figure 1.2 Simplified Ragone plot: the characteristics of various energy storage devices with the comparison of both energy density and power density.^{5, 9}

Figure 1.3 Classification and Comparison of Capacitors.

Figure 1.4 Scheme of electric double layer capacitor (EDLC).¹⁹

Figure 1.5 Classification of supercapacitors.

Figure 1.6 Schemes of n-doping and p-doping (reduction and oxidation) processes of conducting polymers in electrochemical reactions.²⁷

Figure 1.7 General set-up for electrochemical polymerization.

Figure 2.1 (a) Schematic representation of 3,4-ethylenedioxythiophene (EDOT), benzo[1,2-b:3,4-b':5,6-b'']trithiophene (BTT), tris-EDOT-benzo[1,2-b:3,4-b':5,6-b'']trithiophene (TEBTT), and their respective polymers (PEDOT, PBTT, and PTEBTT). **(b)** Schematic representation of the random copolymerization of BTT and TEBTT with EDOT.

Figure 2.2 (a) Linear scan voltammograms collected on gold button electrodes at a scan rate of 20 mV s⁻¹ from a solution of BTT (5 mM), TEBTT (1 mM), and EDOT (5 mM) in DCM. **(b, c)** Individual linear scan voltammograms detailing **(b)** BTT's and **(c)** TEBTT's

oxidation features; the values italicized point to oxidation features that are not well resolved but occur reproducibly between experiments.

Figure 2.3 SEM images of the morphologies of electrodeposited polymer films prepared from several monomer solutions of different BTT/EDOT monomer compositions: **(a)** 1:0, **(b)** 3:1, **(c)** 1:1, **(d)** 1:3, **(e)** 1:6, and **(f)** 0:1. Electrodeposition conditions: 50 mM monomer solutions in ACN; 20 deposition cycles in a voltage window of $-0.7 - +1.5$ V (vs. Ag/Ag⁺), on carbon cloth electrodes; deposition scan rate of 50 mV s⁻¹.

Figure 2.4 (a, b) Cyclic voltammograms of electrodeposited PBTT, PEDOT, and several P(BTT/EDOT) copolymers prepared from several solutions of different BTT/EDOT monomer compositions: 1:0 (black), 3:1 (red), 1:1 (blue), 1:3 (magenta), 1:6 (green), and 0:1 (dark blue) at a scan rate of 20 mV s⁻¹. Electrodeposition conditions: 50 mM monomer solutions in ACN; 20 deposition cycles in a voltage window of $-0.7 - +1.6$ V (vs. Ag/Ag⁺), on carbon cloth electrodes; deposition scan rate of 50 mV s⁻¹. Each voltammogram is normalized to the extent of functionalized surface area. **(c)** Galvanostatic charge-discharge curves collected for the polymers at a current density of 5 mA cm⁻²; the areal capacitance values inferred are indicated on the plot.

Figure 2.5 (a) Cyclic voltammograms of PTEBTT films electropolymerized on various working electrodes and voltage windows (collected in ACN). Electrodeposition conditions: 1 mM monomer solutions in DCM; 120 deposition cycles; deposition scan rate of 50 mV s⁻¹. **(b)** Cyclic voltammograms of PTEBTT films on glassy carbon button electrodes as a function of the number of electrodeposition cycles (collected in ACN). Electrodeposition conditions: 1 mM monomer solutions in DCM; 120 deposition cycles in a voltage window

of $-1.0 - +1.2$ V (vs. Ag/Ag⁺); deposition scan rate of 50 mV s^{-1} . (c) Cyclic voltammograms of PTEBTT films on glassy carbon button electrodes as a function of scan rate (collected in ACN). Electrodeposition conditions: 1 mM monomer solutions in DCM; 20 deposition cycles in a voltage window of $-1.0 - +1.2$ V (vs. Ag/Ag⁺); deposition scan rate of 50 mV s^{-1} . Inset: anodic (I_{pa}) and cathodic (I_{pc}) current intensity variations of the first redox couple of PTEBTT as a function of the square root of the scan rate.

Figure 2.6 Cyclic voltammograms of electrodeposited PBTT and PTEBTT. Electrodeposition conditions of PBTT: scan rate of 50 mV s^{-1} , 20 cycles, voltage window $-0.7 - +1.6$ V (vs. Ag/Ag⁺), 50 mM monomer in ACN. Electrodeposition conditions of PTEBTT: scan rate of 50 mV s^{-1} , 120 cycles, voltage window $-1.0 - +1.2$ V (vs. Ag/Ag⁺), 1 mM monomer in DCM. Each voltammogram is normalized to the extent of functionalized surface area.

Figure 2.7 SEM images of the morphologies of electrodeposited polymer films prepared from several monomer solutions of different TEBTT/EDOT monomer compositions: (a) 1:0, (b, e) 1:1, (c, f) 1:9, and (d) 0:1. Electrodeposition conditions: 1 mM monomer solutions in DCM; 120 deposition cycles in a voltage window of $-1.0 - +1.2$ V (vs. Ag/Ag⁺), on glassy carbon button electrodes; deposition scan rate of 50 mV s^{-1} .

Figure 2.8 (a) Cyclic voltammograms of electrodeposited PTEBTT, PEDOT, and several P(TEBTT/EDOT) copolymers prepared from several solutions of different TEBTT/EDOT monomer compositions: 1:0 (black), 3:1 (red), 1:1 (blue), 1:3 (magenta), 1:9 (green), and 0:1 (dark blue); curves collected at a scan rate of 20 mV s^{-1} . Electrodeposition conditions: 1 mM monomer solutions in DCM; 120 deposition cycles in

a voltage window of $-1.0 - +1.2$ V (vs. Ag/Ag⁺), on glassy carbon button electrodes; deposition scan rate of 50 mV s⁻¹. **(b)** areal capacitance vs. current density increments for several P(TEBTT/EDOT) copolymers. **(c)** areal capacitance vs. cycle number for several P(TEBTT/EDOT) copolymers (at 2 mA cm⁻²).

Figure 3.1 Cyclic voltammograms during electropolymerization of EDOT with increased cycles prepared from **(a)** TBAPF₆/ACN, **(b)** [bmim][Tf₂N], **(c)** [bmim][TfO], and **(d)** [bmim][PF₆] Electrodeposition conditions: 25 mM monomer solutions in supporting medium; 20-180 deposition cycles in a voltage window of $-1.0 - +1.2$ V (vs. Ag/Ag⁺), on carbon paper electrodes; deposition scan rate of 50 mV s⁻¹. Each voltammogram is normalized to the extent of functionalized surface area.

Figure 3.2 Cyclic voltammograms of PEDOT electrodeposited and post-electropolymerization CV in different combinations of ILs and organic solvents. **(a)** [bmim][Tf₂N] as electrodeposition medium and TBAPF₆/ACN as post-electropolymerization electrolyte; **(b)** TBAPF₆/ACN as both electrodeposition medium and post-electropolymerization electrolyte; **(c)** TBAPF₆/ACN as electrodeposition medium and [bmim][Tf₂N] as post-electropolymerization electrolyte; **(d)** TBAPF₆/ACN as both electrodeposition medium and post-electropolymerization electrolyte, with a voltage window of $-1.0 - +1.2$ V (vs. Ag/Ag⁺) and scan rate of 20 mV s⁻¹. Each voltammogram is normalized to the extent of functionalized surface area.

Figure 3.3 Galvanostatic charge-discharge curves collected for the PEDOT electrodeposited in ILs or organic solvents. **(a)** [bmim][Tf₂N] as electrodeposition medium and TBAPF₆/ACN as post-electropolymerization electrolyte; **(b)** TBAPF₆/ACN as both

electrodeposition medium and post-electropolymerization electrolyte; (c) TBAPF6/ACN as electrodeposition medium and [bmim][Tf2N] as post-electropolymerization electrolyte; (d) TBAPF6/ACN as both electrodeposition medium and post-electropolymerization electrolyte, at a current density of 2 mA cm⁻²; the areal capacitance values inferred are indicated on the plot.

Figure 3.4 Summary of galvanostatic charge-discharge values collected for the PEDOT electrodeposited in ILs or organic solvents. (a) [bmim][Tf2N] as electrodeposition medium and TBAPF6/ACN as post-electropolymerization electrolyte; (b) TBAPF6/ACN as both electrodeposition medium and post-electropolymerization electrolyte; (c) TBAPF6/ACN as electrodeposition medium and [bmim][Tf2N] as post-electropolymerization electrolyte; (d) TBAPF6/ACN as both electrodeposition medium and post-electropolymerization electrolyte, at a current density of 2, 5, and 10 mA cm⁻²; the percentage numbers indicated on the plot are the attenuation degree of capacitance values with the increased current density.

Figure 3.5 Summary of galvanostatic charge-discharge values collected for the PEDOT electrodeposited in [bmim][TfO] or TBAPF6/ACN, at a current density of (a) 2, (b) 5, and (c) 10 mA cm⁻².

Figure 3.6 SEM images of the morphologies of electrodeposited PEDOT films grown in (a) (c) TBAPF6/ACN, (b) (d) [bmim][Tf2N]. Electrodeposition conditions: 25 mM monomer solutions in electrolyte; 100 deposition cycles in a voltage window of -1.0 – +1.2 V (vs. Ag/Ag⁺), on carbon paper electrodes; deposition scan rate of 50 mV s⁻¹. The scale bar in (a) and (b) is 2 μm; (c) and (d) is 50 μm.

Figure 3.7 Linear scan voltammograms collected on glassy carbon electrodes at a scan rate of 20 mV s⁻¹ from a solution of BEDOT (5 mM) detailing oxidation features, in (a) [bmim][Tf2N], [bmim][TfO], TBAPF6/ACN and (b) [bmim][PF6].

Figure 3.8 Cyclic voltammograms during electropolymerization of BEDOT with increased cycles prepared from (a) TBAPF6/ACN, (b) [bmim][Tf2N], (c) [bmim][TfO], and (d) [bmim][PF6]. Electrodeposition conditions: 25 mM monomer solutions in supporting medium; 20-100 deposition cycles in a voltage window of -1.0 – +1.2 V (vs. Ag/Ag⁺), on carbon paper electrodes; deposition scan rate of 50 mV s⁻¹. Each voltammogram is normalized to the extent of functionalized surface area.

Figure 3.9 Summary of galvanostatic charge-discharge values collected for the PBEDOT electrodeposited in ILs or organic solvents. (a) [bmim][Tf2N] as electrodeposition medium and TBAPF6/ACN as post-electropolymerization electrolyte; (b) TBAPF6/ACN as both electrodeposition medium and post-electropolymerization electrolyte; (c) TBAPF6/ACN as electrodeposition medium and [bmim][Tf2N] as post-electropolymerization electrolyte; (d) TBAPF6/ACN as both electrodeposition medium and post-electropolymerization electrolyte, at a current density of 2, 5, and 10 mA cm⁻²; the percentage numbers indicated on the plot are the attenuation degree of capacitance values with the increased current density.

Figure 4.1 a) Size distribution pattern of the ball-milled DDNPs measured by DLS in MilliQ water (tuned to pH~3.8 by HCl solution). **b)** TEM image (bright field, 150keV) of the corresponding DDNPs (scale bar: 50 nm). Figure adapted with permission.¹⁵⁸

Figure 4.2 a) FTIR spectra and **b)** Raman spectra (1 scan, $t = 20\text{s}/\text{scan}$, $\lambda = 325\text{ nm}$) of thermally annealed DDNPs. [1] DDNPs prior to ball-milling (black curve), [2] ball-milled DDNPs (blue curve), [3] DDNPs thermally annealed at 500°C for 1h (purple curve), [4] DDNPs thermally annealed at 600°C for 1h (green curve), [5] DDNPs thermally annealed at 700°C for 1h (orange curve), [6] DDNPs thermally annealed at 800°C for 1h (red curve), and [7] DDNPs thermally annealed at 900°C for 1h (pink curve). Spectra given on an arbitrary scale. Note: Significant degradation of the sample was observed with increasing power and number of scans by Raman under the UV laser beam (i.e., upon longer times of exposure) – the peak maximum shifting towards higher frequencies (from ca. 1590 cm^{-1} , G-band contribution from the *graphite-like* outer-shell \rightarrow to 1640 cm^{-1} , –OH). Oxidative degradation mechanisms may be the source of degradation.

Figure 4.3 FTIR spectra of [1] ball-milled DDNPs (control), [2] thermally annealed GDNPs(800), [3] GDNPs(800) treated with the functional maleimide EHM (EHM-GDNP), and [4] the free EHM substituent. The molecular structure and main characteristic vibrations of EHM are indicated on the plot.

Figure 4.4 XRD patterns of the DDNP and GDNP(800) precursors. (arbitrary scale) The characteristic peaks of the crystal planes of diamond at $2\Theta = 44.3^\circ$ (111), 75.5° (220), and 91.7° (311) indicate that the diamond-like carbon structure (sp^3) of the DDNPs is preserved upon annealing at 800°C for 1h.

Figure 4.5 Dilute solutions of DDNPs (left), GDNPs(800) (center) and EHM-treated GDNPs(800) (right) in chlorobenzene (same initial concentration). After 3 days, the colloidal solution of EHM-GDNPs remains stable, while the unfunctionalized DDNP and

GDNP precursors precipitated and settled at the bottom of the quartz cuvettes (white circled).

Figure 4.6 XPS survey spectra of **a)** GDNP(800) and **b)** EHM-GDNP(800). High-resolution XPS analyses and deconvolutions of the C1s peaks of **c)** GDNP(800) and **d)** EHM-GDNP(800).

Figure 4.7 Thermogravimetric analysis (TGA) of **a)** thermally annealed GDNP(800) (control system, red curve) and GDNP(800) treated with the functional maleimide EHM (EHM-GDNP, blue curve), and **b)** the free EHM substituent. Note: the onset of evaporation of the free EHM substituents is observed at ca. 125 °C, while the onset of weight loss of EHM-GDNPs(800) shows beyond 300 °C (not seen in unfunctionalized GDNP(800)).

Figure 4.8 a) 1D ^{13}C CP/MAS solid-state NMR spectrum of thermally annealed GDNP(800); b) 2D $^{13}\text{C}\{^1\text{H}\}$ HETCOR spectra of the GDNP(800); c) 1D ^{13}C CP/MAS solid-state NMR spectrum of GDNP(800) treated with the control unsubstituted maleimide M (M-GDNP); d) 2D $^{13}\text{C}\{^1\text{H}\}$ HETCOR spectra of the M-GDNPs; e) 1D ^{13}C CP/static solid-state NMR spectrum of the M-GDNPs; f) 1D ^{13}C CP/MAS solid-state NMR spectrum of GDNP(800) treated with the functional maleimide EHM (EHM-GDNP). The molecular structures and peak assignments are indicated on the spectra.

Figure 4.9 a) 1D ^{13}C MAS solid-state NMR spectrum of thermally annealed GDNP(800). In the absence of ^1H decoupling, the resonance observed in Fig. 2a (at ca. 47.3 ppm) and pertaining to hydrogen-substituted carbons (CH, CH₂) cannot be observed. Here, a 1D ^{13}C CP/MAS analysis is required to account for the low content of hydrogen-substituted carbons located at the nanodiamond surface (also see Fig. 4.9b). b) 1D ^1H MAS

solid-state NMR spectrum of thermally annealed GDNPs(800). c) ^1H - ^1H double-quantum (DQ) analysis of M-treated GDNPs(800) treated with the control unsubstituted maleimide M (M-GDNP). DQ signals in the w1 dimension are observed at frequencies corresponding to the sum of single quantum (SQ) frequencies of protons that are close to one another in space and will correlate in the w2 dimension with the corresponding ordinary proton resonances. DQ correlation analyses can serve to identify equivalent protons, and is useful here to **differentiate between** CH and CH₂ moieties. d) 2D $^{13}\text{C}\{^1\text{H}\}$ HETCOR spectra of GDNPs(800) treated with the functional maleimide EHM (EHM-GDNP). The molecular structure (EHM) and peak assignments are indicated on the 2D spectrum.

Figure 4.10 Solution ^{13}C NMR spectrum of maleimide M (free substituent).

Figure 4.11 a) Fluorescein-5-maleimide (F5M); b) bright-field and c) fluorescence microscopy images of the GDNPs(800) treated with the fluorescent F5M dye (F5M-GDNP), and spun-coated on glass.

Figure 4.12 FTIR spectra of thermally annealed GDNPs(800) (red curve), the unfunctionalized fluorescein-5-maleimide (F5M) dye (green curve), and GDNPs(800) treated with F5M (F5M-GDNP) (blue curve).

Figure 4.13 a) UV-Vis and b) Fluorescence spectra (in solution) of thermally annealed GDNPs(800) (red curve), the unfunctionalized fluorescein-5-maleimide (F5M) dye (green curve), and GDNPs(800) treated with F5M (F5M-GDNP) (blue curve).

Figure 4.14 Fluorescence microscopy images of a) thermally annealed GDNPs(800) and b) the GDNPs(800) treated with the fluorescent F5M dye (F5M-GDNP); spun-coated

on glass. **c)** and **d)** Bright-field microscopy images of the GDNPs(800) and F5M-GDNP, respectively.

LIST OF TABLES

Table 2.1 Summary of electrodeposition conditions for **PTEBTT**, PEDOT, and several P(**TEBTT**/EDOT) copolymers prepared from several solutions of different **TEBTT**/EDOT monomer compositions (in DCM) and the associated areal capacitance (*Ca*) values on various working electrodes (WE). Experimental details: deposition scan rate of 50 mV s⁻¹; all measurements performed in ACN.

Table 3.1 A selection of cations and anions used to make ionic liquids.

Table 4.1 XPS analyses of the GDNPs(800) and of the EHM-treated GDNPs(800).

Chapter 1

Introduction and Background

1.1 Energy Reality and Energy Storage Demanding

Traditional industry society has been largely relying on the substantial energy consuming derived from the combustion of fossil fuels, which is non-renewable energy. Due to the limitation of the fossil fuel reserves as well as the environmental and ecology impact of the combustion for energy production, there has been intense activities and significant advancement in electricity harvested from renewable energy in recent decades, including solar energy, wind energy, water power, and so on. However, these energy resources are not constant and reliable power supply because of their variable nature and inherent intermittency, which causes significant challenges for the practical usage of electrical equipment and appliance.¹⁻³ The whole energy supply procedure can be simply described as “generation – transmission - distribution”. At this point, electrical energy storage techniques is emerging as the bridge to provide continuous and steady energy supply from energy generation systems to various distributions, which could be modern technologies, e.g. hybrid electric vehicles, portable electronic devices, and telecommunication.⁴

1.2 Electrochemical energy storage: batteries and supercapacitors

1.2.1 Classification of Energy Storage Techniques

Electrical energy generated through the conversion of solar, wind, and other sources can be transformed and stored in various ways, including in mechanical, thermal and chemical forms as shown in **Figure 1.1**.

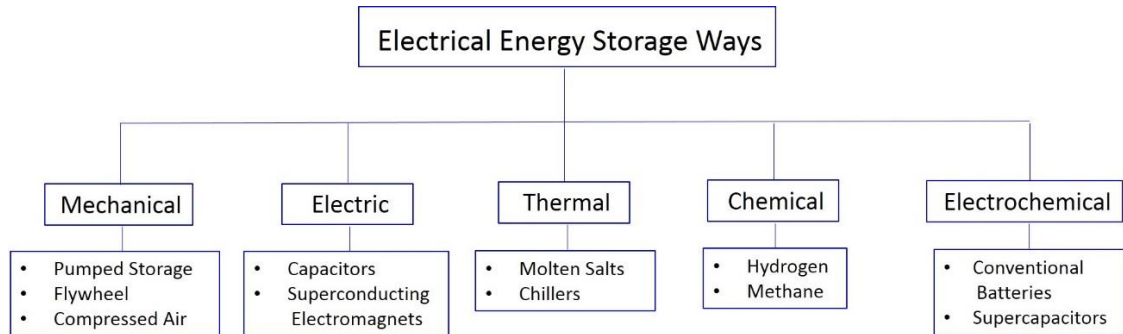


Figure 1.1 Classification of Electrical Energy Storage Methods.

Electrochemical energy storage (EES) is the most traditional energy storage system, which can be classified into three categories: primary batteries (zinc-carbon battery) – un-rechargeable dry voltaic cell which is composed of a zinc shell as the anode and a graphite rod as the cathode, secondary batteries (lead-acid battery) – voltaic cell which can be recharged, and fuel cells – a device requires continuous feeding of fuel and oxygen for the conversion of fuel’s chemical energy into electricity.^{5, 6} The primary common feature for batteries and fuel cells is to obtain electrical energy through the chemical energy stored.

Batteries are the most widely investigated and applied devices in EES systems for their large energy density and economical affordability. However, batteries and fuel cells suffer from inherent disadvantages which is low power density and short cycling life.^{7, 8} A capacitor is a device consisting of two or more conductive plates segmented by dielectric separator. When electric current flows through the capacitor, the potential energy is stored electrostatically between these conducting plates. When the capacitor connects to an external circuit, electric current will be discharged quickly. As illustrated in **Figure 1.2**, typically the relative higher energy density could only be achieved at the sacrifice of power density, and vice versa. So, high power-density devices should be complemented by dielectric capacitors or EDLCs to enhance the interfacial storage of charge on its working electrode surface.^{5,9} Batteries and supercapacitors both rely on electrochemical processes, although separate electrochemical mechanisms determines their relative energy and power density. Due to supercapacitor's physical/chemical charge storage mechanism and slow reaction kinetics for batteries and fuel cells, supercapacitors are expected to provide greater power density and sustainable life cycle compared with batteries and fuel cells but lower energy densities. On the other hand, supercapacitors can offer higher energy density compared with conventional energy storage devices. Thus, electrochemical supercapacitors (ESCs) are featured as critical components to complement and fill between the gap between batteries and conventional capacitors. They provide the prospects of maintaining the relatively high energy density comparable to batteries meanwhile can be charged and discharged rapidly to afford robust power densities.^{3, 8} Due to these characteristic, ESCs can be utilized conveniently and portably as the high-power electrical supplier for various stationary and mobile apparatus.

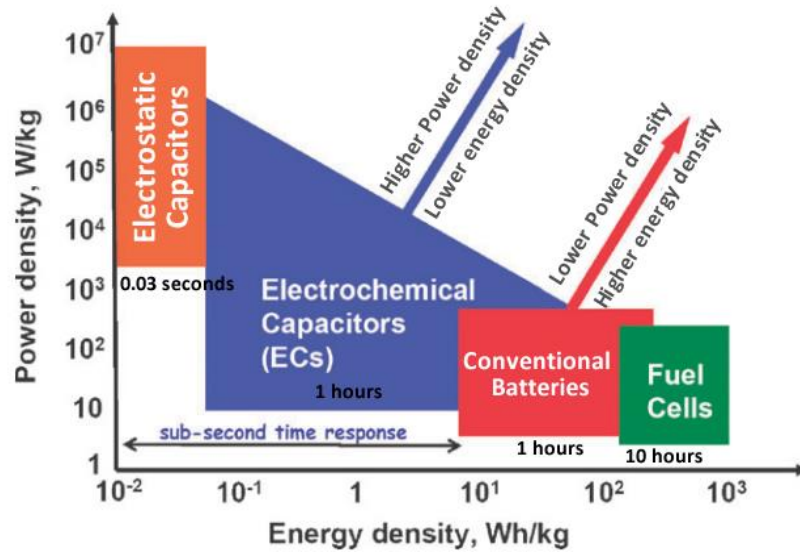


Figure 1.2 Simplified Ragone plot: the characteristics of various energy storage devices with the comparison of both energy density and power density.^{5, 9}

1.2.2 Classification of Capacitors

Depending on the choice of electrode and electrolyte, three major categories can be classified for the capacitors, which are electrostatic capacitors, electrolytic capacitors and supercapacitors. They can be further divided into subgroups according to the specific materials used as electrode and electrolyte.

As shown in **Figure 1.3**, Electrostatic capacitors are firstly developed way for electrical energy storage. Consisting of two conductive electrodes (films, foils, sintered beads of metal or conductive electrolyte, etc.) separated by an dielectric or insulating material (ceramic, glass, plastic film, vacuum/air, paper, oxide layer mica, etc.). In this type of capacitors, electric charges can be accumulated and stored inside the concentrated electric field between two parallel electrodes. The equivalent series resistance (ESR) and equivalent

series inductance (ESL) has low values for this arrangement. Discharge time could be within tens of microseconds and power delivering is on the order of 1.5 mWh/kg and 2 mWh/L.¹⁰

Different from the bulk insulators of conventional electrostatic capacitors, current electrolytic capacitors are normally polarized capacitors, the anode electrode of which are composed of a special metal with an insulating oxide layer performs as the dielectric. The surface of the oxide layer is covered by a solid or liquid electrolyte, serving as cathode electrode. Due to this the dielectric oxide layer is very thin with enlarged anode surface, electrolytic capacitors generally provide energy density on the order of 30 mWh/kg and 120 mWh/L, respectively, which are much higher than that of the electrostatic capacitors, however, much smaller value than electrochemical supercapacitors.¹⁰

For supercapacitors, electrical energy is stored and released electrochemically by charge separation in the nanoscale at the interface between working electrode material and the surrounding electrolyte. Generally, a supercapacitor device is constructed of two working electrodes separated by a porous separator made of dielectric porous film, all of which is saturated with electrolyte. The electrolyte is usually an aqueous or organic solvents containing a large amount of homogenously dispersed ions. So, the ionic can flow between the electrodes carrying the currents and keep the currents from discharging the cell. The core structure of a supercapacitor is the electroactive materials on the working electrode.

¹¹ The Structures, components, properties, pros and cons of capacitor catalog is summarized in **Figure 1.3**. Since the focus of this dissertation, more details on supercapacitor will be further discussed in the following section.

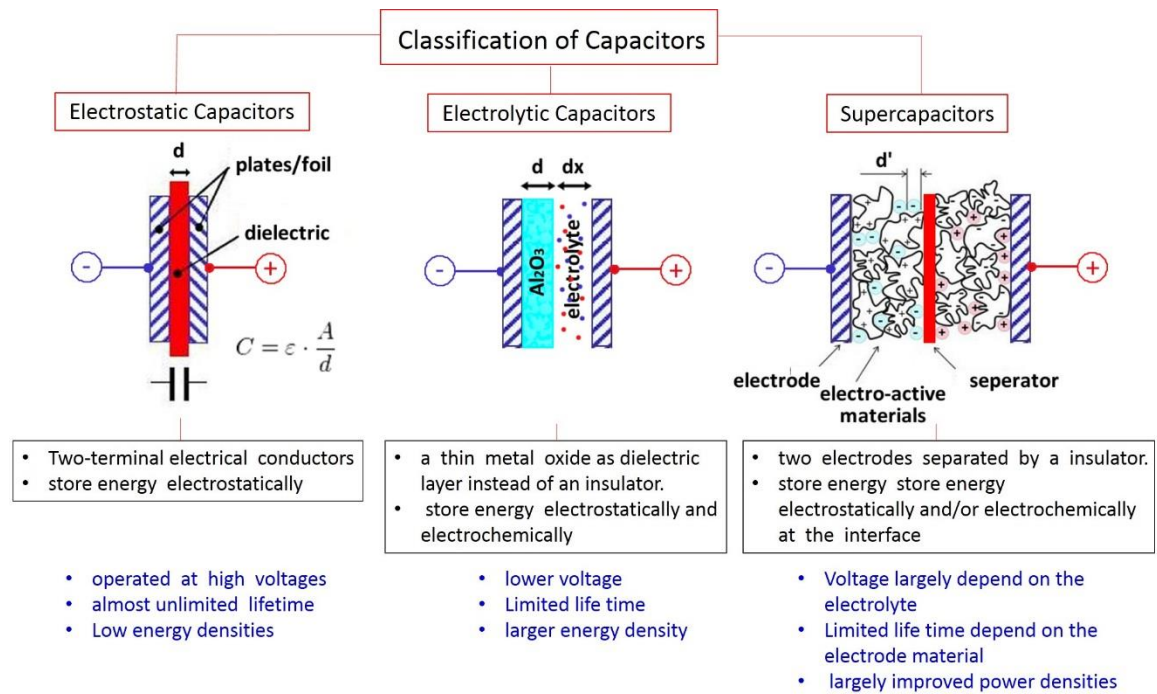


Figure 1.3 Classification and Comparison of Capacitors.

1.2.3 Classification and General Properties of Supercapacitors

While traditionally batteries offer high energy densities, and conventional electrostatic capacitors offer high power densities, supercapacitors, also named as electrochemical supercapacitors or ultracapacitors, fill the gap of the two types of energy storage devices and improve the charge-and-discharge rates and cycle life.^{5-8, 12} Electrochemical capacitors can be distinguished according to the two main mechanisms of energy storage ways: (i) electrochemical double-layer capacitors (EDLCs) by accumulating surface ions electrostatically at the interface between electrode composed of high-surface carbonaceous materials and its surrounding electrolyte, and (ii) pseudocapacitors based on surface redox (faradic) reactions of electro-active materials typically transition metal oxide/hydroxide and conducting polymers.^{8, 13-15}

1.2.3.1 Electrochemical Double-Layer Capacitors (EDLCs)

Surface area of carbonaceous materials (activated carbons (ACs), carbon nanotubes (CNTs), graphene, etc.) can be tuned by designing different morphology and have been utilized as working electrodes for electrochemical double layer capacitors (EDLCs).^{16, 17} The mechanism of charge generation for EDLCs includes surface dissociation and ion adsorption from crystal lattice defects or electrolyte.⁸ Electrical charges take place only on the surface by electrostatic accumulation. From **Figure 1.3**, the capacitance of EDLCs generated from electroactive materials of the working electrode, which includes interfacial contacting area of the carbon materials and electrolyte. Electrical charges is just accumulated on these interfaces. In the charging process, the accumulated electrons can be transferred from the negative side to the positive side of electrode via an external voltage. Within the supporting medium, cations transfer towards negative side and anions travel towards positive side. In the case of discharge, the whole processes continue in a reverse mode. By this mechanism, accumulated electrons and energy is accumulated and stored in the double-layer interface. In this type of ECSs, there is no charge transfer through the bulk electrode materials and electrolyte interface. Also, there is no net ion exchanges occur between the bulk electrode and the electrolyte. It can give an indication that the concentration of the electrolyte does not fluctuate in the charge-and-discharge processes.¹⁸

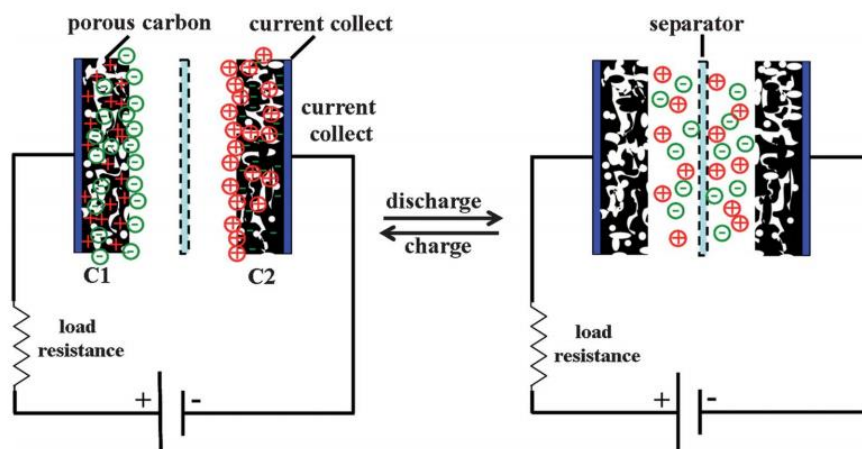


Figure 1.4 Scheme of electric double layer capacitor (EDLC).¹⁹

The energy density of EDLCs is much higher than conventional dielectric capacitors because the thicker thickness of the double layer is able to store more energy. EDLCs can store a substantial amount of electrical charges which is able to be delivered at higher power density compared with rechargeable batteries.¹¹ There are lots of other advantages for EDLCs, e.g. fast charge-and-discharge rates, high cycle life, lightweight, high stability and affordability. However the charge accumulated is purely electrostatic so it will limit the energy density for the restriction of surface area of the carbon materials.^{16, 20} Due to this shortcoming, the application of pseudocapacitive materials has been investigated with higher energy density and capacitance.

1.2.3.2 Pseudocapacitors

The working mechanism of pseudocapacitors or faradaic supercapacitors (FS) is different from electrostatic EDLC. With the apply of an additional potential, redox reactions together with faradaic reactions would take place in the pseudo-materials, resulting in charge transfer reactions through the electrodes. This process resembles the charge-discharge processes in batteries. Pseudo-materials undergoing such kind of redox

reactions include a few transition metal oxides/hydroxides/chalcogenide,^{6, 15} including ruthenium oxide (RuO₂), manganese dioxide (MnO₂),^{21, 22} cobalt oxide (Co₃O₄)²³ and NiCo₂S₄,^{24, 25} as well as conducting polymers, which could be polyaniline (PAni) and polypyrrole (PPy) and polythiophene (PTp).^{20, 26, 27}

Faradaic processes can be divided into three major types, which are reversible adsorption, e.g hydrogen adsorption on platinum/gold surfaces, redox reactions of transition metal oxides/hydroxides, and reversible electrochemical doping and dedoping processes of conjugated conducting polymers.⁶ For the third type, redox processes occur both on the surface and in the bulk near the surface of these pseudo-materials. It has been demonstrated that the energy storage mechanism based on Faradic mechanism can not only provide an enlarged working voltage window, but also enhance capacitance and energy densities compared with EDLCs.²⁸ As reported, the capacitance of a supercapacitor based on Faradaic mechanism can be 10 to 100 times higher compared with EDLC based on electrostatic accumulation mechanism.²⁹ Even though, also because of the energy storage mechanism, an FS is typically disadvantage in power density compared with EDLC because it takes relatively longer time for faradaic processes than nonfaradaic processes.³⁰ Moreover, similar to batteries, also due to the redox reactions occurring near the electrode, the phase of pseudocapacitance materials often changes within the electrode, which limits their stability during cycling and power densities.

1.2.3.3 Hybrid Supercapacitors

In recent decades, the hybrid design of EDLCs carbon materials and pseudocapacitance materials has inspired new types of so-called hybrid electrochemical capacitors (HECs).¹⁵

The advantages of the kind of hybrid structure is contributed by both non-Faradic and Faradic materials, where the synergistic effects of both EDLCs and faradaic capacitance mechanisms can make a contribution. For pseudocapacitance materials, charges are accumulated via faradic electrochemical process with capacitance increasement and working voltage window enlargement. Meanwhile, the incorporation of carbon material insure the stability and life time of the whole device. For both of the two mechanisms, to achieve high capacitance values, large surface area, suitable pore-size distribution, and high conducting properties is necessarily required, which will be further discussed in **Chapter 2**.

1.2.3.3.1 Metal Oxide- Carbon Composite Nanomaterials

In the metal oxide-carbon composite nanostructures, carbon nanotubes, graphene, active carbon and other electrical conducting carbon materials can be chosen as the hybrid with metal oxides in view of their superior mechanical and electrochemical stability.^{16, 31} There are two major ways to form the hybrids for carbon materials.

One way is to coat carbon layers onto the oxide surface, e.g. soaking oxides into carbohydrate solution or under hydrothermal/solvothermal methods.³²⁻³⁵ Despite the convinience and affordability of this method, the synthesized carbon materials are usually too amorphous and less conducting.³⁶ Besides, carbon layers can easily react with multivalent metal oxides in the process of carbonization, therefore their components and feeding ration should be precisely determined. Graphene and metal oxide encapsulation by electrostatic interaction as well as in-situ grown of metal/metal oxide and carbon nanotubes shows improved electrical conductivity and mechanical integrity.³⁷⁻³⁹ Coaxial carbon core-

oxide shell nanostructures is the other route. This hybrid configuration has several important merits, which are excellent conductivity for the structure of carbon core; homogeneous electrochemical accessibility without the usage of binders and other non-conducting materials; a dual energy-storage mechanism.⁴⁰

1.2.3.3.2 Metal Oxide- Conducting Polymer Hybrids

Electroactive conjugated polymers also known as conducting polymers are also promising candidates to supplement metal oxides in the application of energy storage.⁴¹ It can provide a buffering layer with flexibility and increase the hybrid's conducting ability when mixed with metal oxides. However, the disadvantage of conducting polymers is that the mechanical and electrochemical stability is poor in aqueous electrolytes. As a result, conducting polymers has shorter cycle life compared with carbon materials, which is one of the major obstacles for real applications.⁴² There are various ways and combinations for conducting polymers and metal oxides hybrids to harvest their synergetic effects, e.g. the sandwich structure of PANI between layers of MnO_2 , polymers decorated by metal oxide.

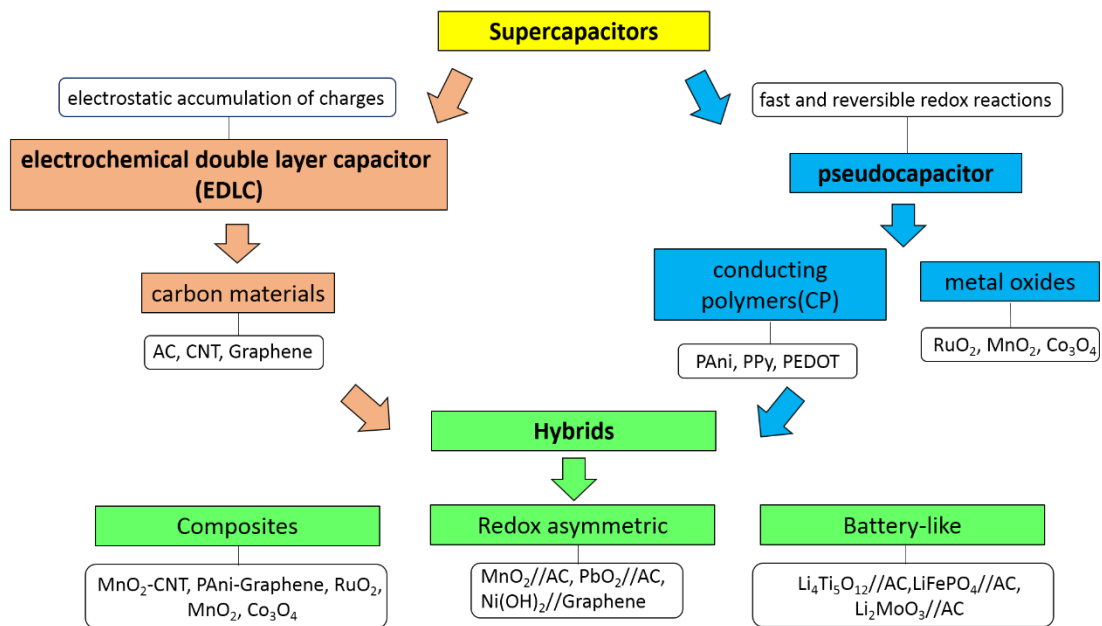


Figure 1.5 Classification of supercapacitors.

1.3 Techniques to Synthesis Electronically Conducting Polymer

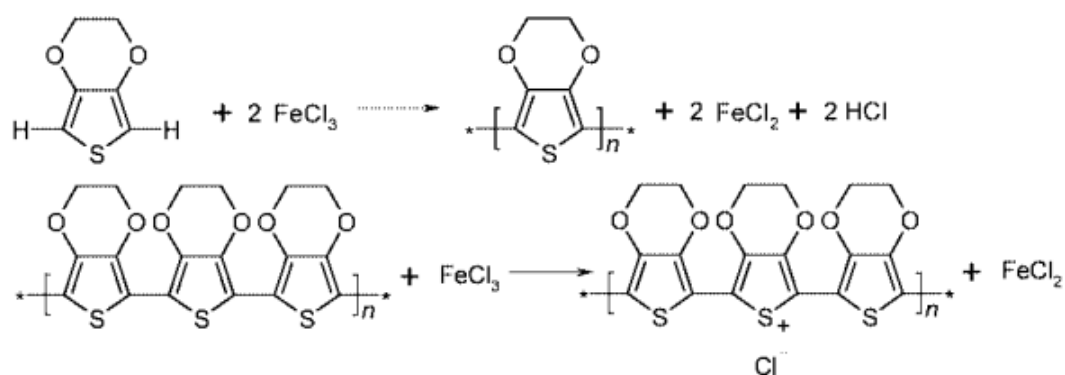
Electrodes for Supercapacitors

1.3.1 Chemically oxidation

There are several routes to produce conducting polymers, e.g. electrochemical oxidation, photopolymerization, and chemical oxidation. Electrochemical polymerization is ideal to synthesize nice polymer films in a controlled manner on the conducting substrate, while chemical polymerization can be applied to synthesize colloidal dispersions of polymers, which is much more amendable for production in large scale.

Because of conjugated bonding structures, conjugated polymers such as polypyrrole, polyaniline, polydioxothiophene, show high electronic conductivity. These polymers can be produced by electrochemically oxidize the corresponding monomers. In-situ deposition

of PEDOT can occur in an acetonitrile solution with EDOT monomer and iron (III) chloride oxidant as shown in **Scheme 1.1**. Doping is a subsequently process after EDOT is polymerized.



Scheme 1.1 Chemical oxidation process of EDOT and the doping process of PEDOT polymer.⁴³

1.3.2 Electrochemical polymerization

Electrochemical polymerization can also bring high oxidation state to the polymer in its growth process, and the doping/dedoping of ions from the electrolyte can be realized through trapping/escaping from the polymer chains. When cycling in the appropriate voltage potential windows, these polymers are able to go through a doping and dedoping reversible switching process, which makes the polymers as well as this polymerization techniques can be utilized in electrochemical capacitors, electrochromic, batteries, and so on.

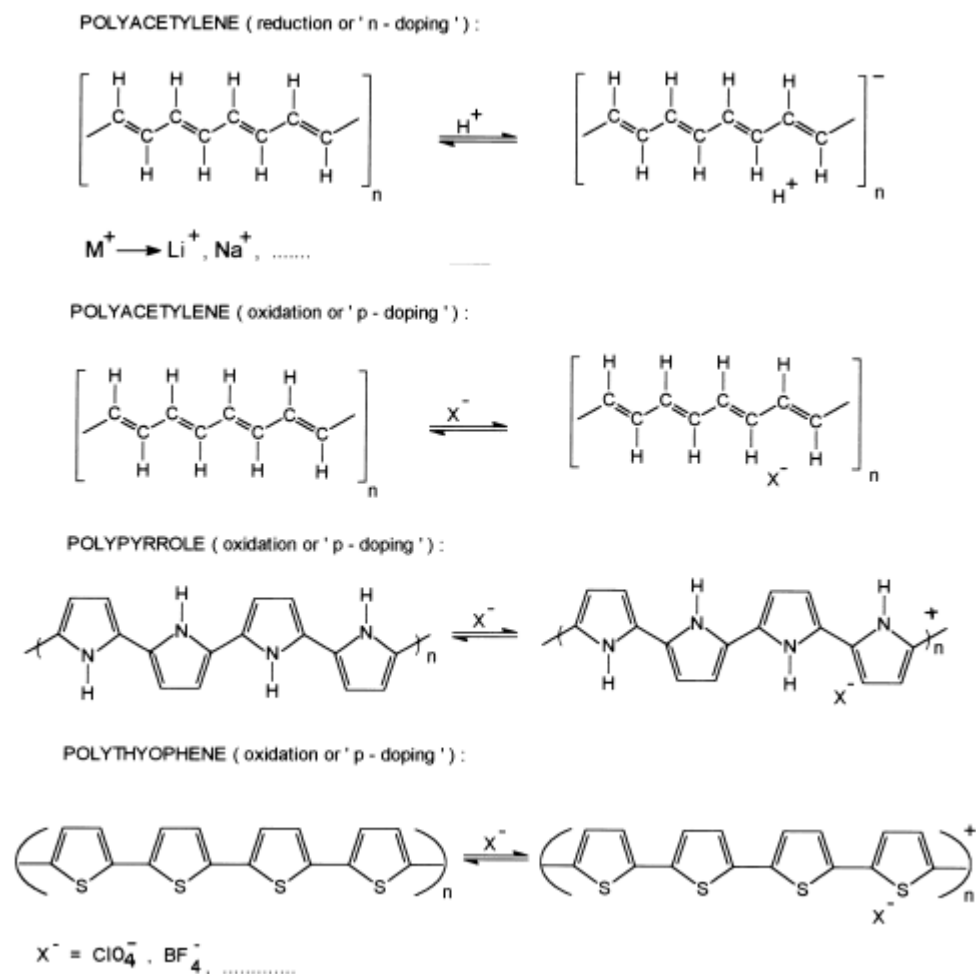


Figure 1.6 Schemes of n-doping and p-doping (reduction and oxidation) processes of conducting polymers in electrochemical reactions.²⁷

1.3.2.1 Choice of monomers

To synthesize conducting polymers through electrochemical techniques, the monomers should have π -conjugated structures and relatively low anodic oxidation potential for efficient polymerization, the structure of which is prone for electrophilic substitution reaction. Especially, aromatic-structure monomers can undergo electrophilic substitution reactions while still maintaining the aromatic framework. Such monomers which are

difficult to polymerize by chemical routes can be oxidized by electrochemical polymerization process. Relative low potential of oxidation can avoid of the oxidative decomposition of the supporting electrolyte and other side reactions of the solvent during electropolymerization process.²⁷

1.3.2.2 Choice of the growth medium and supporting electrolyte

Redox reactions can take place for monomers during the electropolymerization process, and these reactions is carried out via radical cation intermediates. It is reasonable to consider that the properties of growth medium and supporting electrolyte, especially their nucleophilic charaters plays an important role in the polymerization redox reactions. Poor nucleophilic solvents, e.g. aprotic specise, which could be benzonitrile and acetonitrile, is usually prefered. Meanwhile, solvents with strong nucleophilic anions, e.g. cyanide, acetate, alkoxide, and hydroxide could not be the ideal medium to produce polymer films in good quality. Soluble oligmers and polymers will be produced and dispersed throughout the whole solution. However, by adding suitable protic acid, some of the highly nucleophilic aprotic solvents, e.g. hydroxylic solvents, Dimethylformamide, Dimethyl sulfoxide, can still be applied in these kind of reactions. For some family nucleophilic solvents, e.g. halides species, it is not easy to deposit nice films onto the substrate because halides species are more prone to be oxidized than the targeted monomers. Besides the nucleophilic properties of solvents, the choice of the growth medium and supporting electrolyte should also be considered based on the solubility of electrolytic salts and monomers for polymerization. For the electrolytic salts, quarternary ammonium salts (R_4NX , $R = \text{Alkyl, Aryl radical}$; $X = \text{BF}_4^-, \text{PF}_6^-, \text{Cl}^-, \text{ClO}_4^-, \text{Br}^-, \text{I}^-, \text{CF}_3\text{SO}_3^-, \text{CH}_3\text{C}_6\text{H}_4\text{SO}_3^-$)

show high solubility in these nucleophilic aprotic solvents, and have usually been chosen as supporting electrolytes. In contrast, sodium and potassium compound commonly has low solubility in these solvents.²⁷

1.3.2.3 Electrodes

For a standard three-electrode electrochemical system, it contains three main parts, a working electrode, a counter electrode, and a reference electrode. A working electrode is typically a conducting substrate/steel providing a site for polymer electrodeposition, Since redox reactions take place for the formation of polymeric film on the working electrode, inert electrodes, e.g. Pt, Au, or glassy carbon is generally used as substrates would obtain a layer of conducting polymers on the surface, in the same time, concurrent oxidation of electrode materials can be avoided. However, inexpensive and more available substrate materials are usually choosed for practical applications such as supercapacitors, which can be ITO, carbon paper, carbon cloth and stainless substrates. A counter electrode is usually a metallic steel/foil made of inert and conducting metals, e.g. platinum, gold, and nickel. A reference electrode can be Ag/AgCl or saturated calomel electrode (SCE).

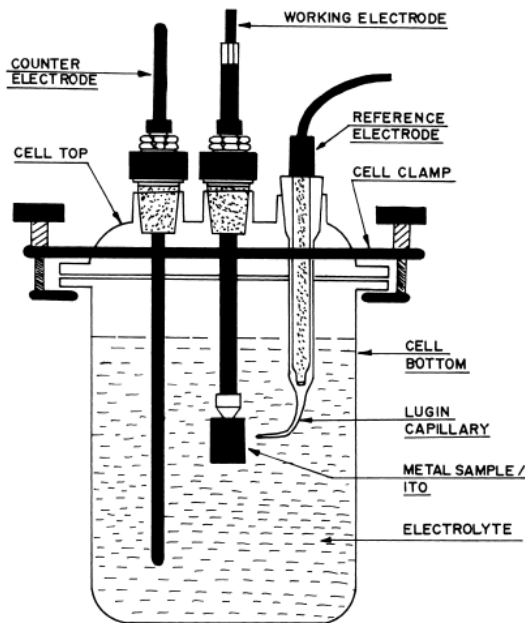


Figure 1.7 General set-up for electrochemical polymerization.²⁷

1.3.2.4 Attractive features of Electrochemical Polymerization

One of the most attractive features for electrochemical polymerization technique is it requires the choice of supporting electrolyte. The two main functions of supporting electrolyte in ECP is, firstly, the supporting electrolyte is usually conducting salts, which can be dissolved in the electrolytic solution and make the whole solution conducting. Secondly, the supporting electrolyte can be a source of counterions, and the synthesized polymer unite can be doped by anion/cation intercalation. “Dopant ions” can be adjusted accordingly by the wide choice of cations and anions from the suitable electrolyte. The doping process takes place simultaneously with the formation of polymers. However in conventional routes, polymer synthesis and doping process are subsequent and independent process.

Chapter 2

Multiple-Branch-Chain 3, 4-Ethylenedioxythiophene Derivatives Designed as Crosslinkers in the co- Electropolymerization of EDOT Yields High Capacitance

2.1 Introduction of Conducting Polymers and EDOT in Supercapacitor Applications

Of all electrochemical energy storage (EES) systems, Electrochemical supercapacitors (ECSs) is well suited for renewable energy-storage applications owing to the high charge and discharge rate, good energy-storage efficiency, steady cycle life and can be intergrated with renewable energy sources.^{7, 8} These properties allows them to supply stable power under fluctuating energy sources, e.g. wind and solar power generation.^{5-8, 12} As discussed in **Chapter 1, Section1.2.3**, Three different families of supercapacitors can be differentiated depending on the electro-active material employed.^{13, 20, 44} Pseudo-materials provide much higher energy density than carbonaceous materials due to their energy-storage mechanism is based on Faradic reaction. One type of electro-active materials for pseudocapacitors are transition metal oxides/hydroxides/chalcogenides.^{6, 15} Huge

gravimetric capacitive performance can be achieved by RuO₂, MnO₂,^{21, 22} V₂O₅,⁴⁵ Co₃O₄²³ and NiCo₂S₄,^{24, 25}. However, there would also be some difficulties when metal oxides are used as capacitance materials. Firstly, these metal oxides are wide bandgap semiconductors or insulators which show less conducting ability.⁴⁶ Less conductivity will not only put an detrimental effect for capacitance performance, but also generate joule heat of substantial amount in the repeated charging and discharging actions. Then, metal oxides are usually suffering from poor ion transportation.⁴⁷ To provide sufficient and larger contact area between the electrode matrix and electrolyte solution, metal oxides are typically synthesized with porous morphologies and hierarchical structures in nanoscale, which could offer sufficient ion transport pathways inside. However, in this case, due to the increased amount of grain boundaries, the rise of electrical resistivity will inevitably happen.^{48, 49} Typically, metal oxides suffer from severe volume swelling and shrinking during charge and discharge processes, which can damage and even pulverize the polymer film.⁵⁰ Most of these extensively studied oxides belong to transition metals which is rare and prohibitive in price, e.g. RuO₂ pseudocapacitor has the highest specific capacitance (~1000 F/g) in this class, but is a vehicle-sized ESC of RuO₂ would cost more than \$1 million.⁵¹ As a result, efforts is driving to develop more sustainable electroactive conjugated polymers (ECPs) for improvement of energy-storage capacity per unit cost.^{20, 26, 52}

There is a significant promise for ECPs in applications of electrochemical devices including energy harvesting,⁵³ electrochromic displays,⁵⁴ etc. Among these, ECPs has also been developed as electroactive materials in electrochemical supercapacitors (ESCs).^{6, 55} Compared with metal oxides, ECPs are attractive because they have good intrinsic

conductivity, namely, from a few S cm^{-1} to 500 S cm^{-1} in the doped state,^{56,57} much lower band gaps compared with conventional polymers,⁵⁴ relatively fast doping and undoping process, the ease of synthesis, and tunable electronic and structural properties through structural modifications.^{26, 58, 59}

Besides the usage of electroactive polymers reported initially for redox-reaction based supercapacitors,^{58, 60, 61} There has been increasing effort devoted to develop new conjugated monomers/polymers with different structures, especially for polythiophene, polyaniline, and polypyrrole.^{20, 26, 27, 62} The advantage of polyaniline is that it has the ability to store charges and energy in both aqueous and nonaqueous electrolyte solutions. In contrast, polythiophene has shown electrochemical instability which limited their application in energy storage devices, electron-rich derivatives of polythiophene, especially poly (3,4-ethylenedioxythiophene) (PEDOT) has attracted tremendous attention contributed to their superior features including fast redox switching speeds, relative higher electrochemical stability and capacitance.⁶³ Motivation for the use of polythiophene instead of polyaniline or polypyrrole in such devices stems from the fact that a higher cell voltage can be achieved with the polythiophene as most of these can be n- and p-doped because of a smaller band gap. Consequently, derivatives and analogues of poly (3, 4-alkylenedioxythiophene)s of similar structures with PEDOT have been studied for electrochemical devices.

In addition to the intrinsic pseudocapacitive properties of ECPs, their nano- and meso-scale morphologies and the interplay between material surface and electrolytes is also critical to optimizing the capacitance of electrode material and thus, overall supercapacitor performance. Considering both morphology and material/electrolyte interactions,

conjugated polymers that can be electropolymerized into highly porous networks are promising pseudocapacitive materials for use in the construction of supercapacitors for specific applications.⁶⁴⁻⁶⁶ Electropolymerization approaches using monomer solutions can be performed reproducibly, while incorporating ions and counterions in the process of forming open, porous nanostructured films.^{67, 68} Thus, several studies have emphasized the range of achievable morphologies using conjugated polymers derived from the electropolymerization of commercially available monomers such as polyaniline (PANI),^{69, 70} polypyrrole,^{70, 71} polythiophene,⁷² and poly(3,4-ethylenedioxythiophene) (PEDOT).^{73, 74} For example, varying the electrodeposition conditions of PANI induces considerable morphological changes that impact film capacitance (i.e., nanospheres to nanorods to nanofibers).⁷⁵

Another approach to tuning polymer film morphology relies on the development of functional monomers that can adopt other specific electrodeposition patterns upon electrochemical polymerization including multivalent monomers or comonomers that form 2D or 3D covalent networks.^{76, 77} For example, phenylenevinylene-,⁷⁶ phenylethynylene-,⁷⁷ and triazine-based⁷⁷ motifs have been shown to yield highly porous morphologies with specific surface values $>1,000 \text{ m}^2 \text{ g}^{-1}$ in specific experimental electrodeposition conditions, while trivalent motifs such as 1,3,5-tris(oligothienyl)benzene^{78, 79} and triarylamine⁸⁰⁻⁸³ are amenable to synthesizing efficient capacitive conjugated networks. In parallel, the copolymerization of monomers with comparable oxidation potentials, such as bithiophene and triphenylamine (10 mol%) motifs,⁸² is another promising strategy for the preparation of tunable capacitive polymeric frameworks.

2.2 9,9'-Spirobi[9H-fluorene] 3, 4-Ethylenedioxythiophene Derivative as Crosslinker in the co-Electropolymerization of EDOT

In this report, we compare the electropolymerization patterns of two 2D (trivalent) building blocks—benzo[1,2-*b*:3,4-*b'*:5,6-*b''*]trithiophene (BTT) and tris-EDOT-benzo[1,2-*b*:3,4-*b'*:5,6-*b''*]trithiophene (TEBTT) (**Figure 2.1**)—and their copolymerization with 3,4-ethylenedioxythiophene (EDOT). We also describe the experimental conditions required to form hierarchical π -conjugated frameworks with particularly high areal capacitance. Based on the basic characterization of BTT-based well-defined oligomers^{84, 85} and TEBTT homopolymers from previous reports,⁸⁶ we clarify the fundamental differences between electropolymerized homopolymer and copolymer networks made from these two building motifs, and emphasize their use for the synthesis of high-capacitance, nanostructured 3D polymeric networks that are resilient to repeated electrochemical cycling. In particular, comparing BTT- and TEBTT-based networks, we find that TEBTT-based homopolymers and copolymers with EDOT are substantially more capacitive (reaching up to 271.1 mF cm⁻² and 443.8 mF cm⁻² (1 mA cm⁻²), respectively) and stable upon cycling (up to 73% and 89% capacitance retention after 1,000 cycles, respectively) than their BTT counterparts.

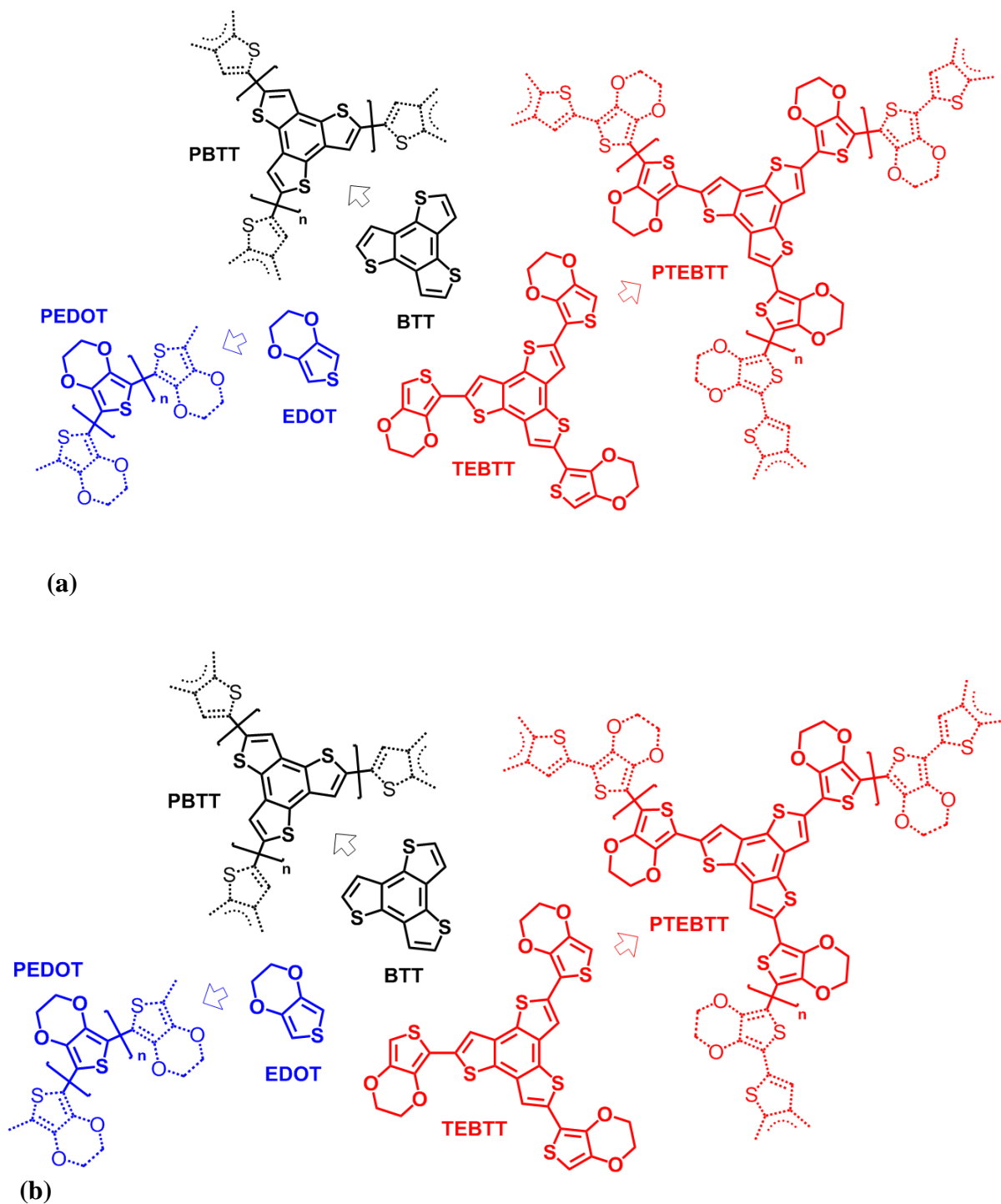


Figure 2.1 (a) Schematic representation of 3,4-ethylenedioxythiophene (EDOT), benzo[1,2-*b*:3,4-*b'*:5,6-*b''*]trithiophene (BTT), tris-EDOT-benzo[1,2-*b*:3,4-*b'*:5,6-*b''*]trithiophene (TEBTT), and their respective polymers (PEDOT, PBTT, and PTEBTT).

(b) Schematic representation of the random copolymerization of BTT and TEBTT with EDOT.

2.2.1 Experimental Section

2.2.1.1 Synthetic Procedures

Benzo[1,2-*b*:3,4-*b'*:5,6-*b''*]trithiophene⁸³ (BTT) and tris-EDOT-benzo[1,2-*b*:3,4-*b'*:5,6-*b''*]trithiophene⁸⁶ (TEBTT) were synthesized in the lab. All monomers were characterized by ¹H NMR (400 MHz) and ¹³C NMR (100 MHz) on a Bruker Advance III Ultrashielded 400 Plus instrument at room temperature. The ¹H, ¹³C spectra were referenced according to the tetramethylsilane (TMS) internal standards. High-resolution mass spectrometry (HRMS) data was recorded using an LTQ Orbitrap Velos MS (Thermo Fisher Scientific) in the positive atmospheric pressure photoionization (+APPI) mode. Elemental analyses were performed on a Flash 2000 - Thermo Scientific CHNO Analyzer.

2.2.1.2 Electrochemical Measurements

The electrochemical characterizations were performed in a standard three-electrode cell placed in a nitrogen-filled glovebox to which a Versastat 4 potentiostat/galvanostat (Princeton Instrument) was connected. In all three-electrode cell experiments, a nonaqueous Ag/Ag⁺ electrode [consisting of a Ag wire immersed in a 10 mM AgNO₃ and 100 mM tetrabutylammonium perchlorate (TBAP) solution in acetonitrile (ACN)] was used as the reference electrode, and a platinum wire was used as the counter electrode. All electrolyte solutions were prepared using anhydrous solvents [ACN, dichloromethane

(DCM)] and with 100 mM tetrabutylammonium hexafluorophosphate (TBAPF₆) as the supporting electrolyte.

The specific areal capacitance (Ca) of electrodeposited polymeric materials was calculated from the charge-discharge curves through the following general equation:⁸⁷

$$Ca = I^* \Delta t / \Delta V$$

where Ca is expressed in mF cm⁻² and the constant current (I) is applied in mA cm⁻²; Δt is the discharging time (in seconds) and ΔV is the potential change (in V).⁸⁷ In this report, we discuss and emphasize Ca values (as opposed to the specific gravimetric capacitance Cs) by using a measurement of the functionalized surface area that is more accurate than measuring the exact mass of the electrodeposited polymeric material.

2.2.1.3 Imaging Characterization

Electrodeposited polymer film morphologies were characterized with a Quanta 600 scanning electron microscope (SEM) (FEI). Prior to imaging the samples, the supporting electrolyte was washed from the electropolymerized thin film by successive rinsing steps in neat ACN, and a 5 nm layer of gold was sputtered onto the polymer films (to minimize charging effects). The SEM was operated at a working distance of 5 mm and an accelerating potential of 10 kV.

2.2.2 Results and Discuss

2.2.2.1 Electrochemical Characterizations of BTT and TEBTT

Figure 2.2a shows the linear scans in potential and actual onsets of oxidation for BTT, TEBTT, and EDOT (control scan); the various oxidation features observed for BTT and TEBTT on scanning linearly in the -2.0 – +2.5 V potential window (vs. Ag/Ag⁺) are detailed directly on the plots in **Figure 2.2b** and **Figure 2.2c**, respectively (oxidation potentials taken at the maximum peak height). In all three experiments, a dark electrodeposited film forms on the gold button electrode, indicating that electropolymerization is occurring during linear scans. BTT exhibits three well-pronounced oxidation peaks at +1.28 V (E_{ox1}), +1.59 V (E_{ox2}), and +2.04 V (E_{ox3}). Interestingly, prior studies of BTT-based systems via cyclic voltammetry (CV) have only described one oxidation peak, albeit at different potentials of +1.39 V (vs. Ag/Ag⁺)⁸⁶ and +1.55 V (vs. Ag/Ag⁺).⁸⁵ we note that the oxidation feature observed in the prior study⁸⁶ was somewhat broad and likely encompassed oxidation peaks E_{ox1} and E_{ox2} similar to those shown in **Figure 2.2b** (no cyclic voltammogram was provided in the later study). The first oxidation peak seen for BTT ($E_{\text{ox1}} = +1.28$ V) is sharp and has an onset at +1.11 V, on the same order of that observed for EDOT (+1.02 V; **Figure 2.2a**) and similar to that reported for terthiophene (*ca.* +1.0 V; vs. Ag/Ag⁺).^{88, 89} This oxidation onset is, however, significantly lower than that of single-ring thiophene motifs (*ca.* +1.75 V; vs. Ag/Ag⁺),⁸⁹ illustrating how redox potential depends on conjugation length and HOMO-LUMO gap reduction in more extended BTT π -systems.⁸⁹ The second and third oxidation features in the linear scan of BTT ($E_{\text{ox2}} = +1.59$ V and $E_{\text{ox3}} = +2.04$ V) suggest a sequential oxidation

of the three thiophene rings of BTT to radical cations, whereby each subsequent oxidation becomes less favored in response to the presence of previously formed positive charges.

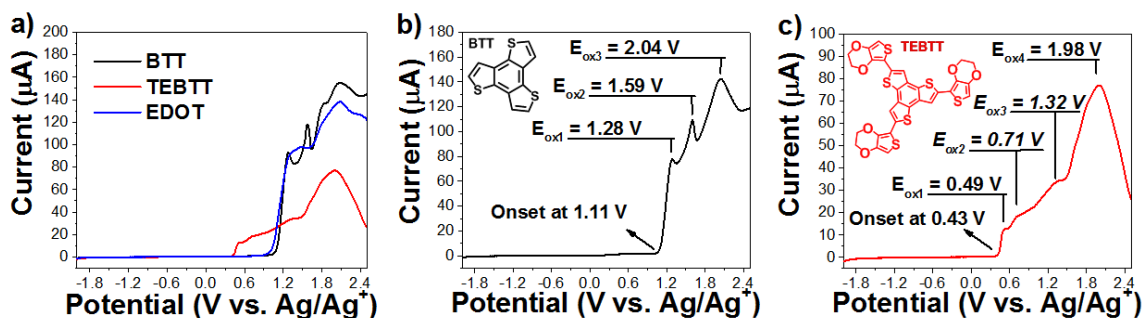


Figure 2.2 (a) Linear scan voltammograms collected on gold button electrodes at a scan rate of 20 mV s^{-1} from a solution of BTT (5 mM), TEBTT (1 mM), and EDOT (5 mM) in DCM. (b, c) Individual linear scan voltammograms detailing (b) BTT's and (c) TEBTT's oxidation features; the values italicized point to oxidation features that are not well resolved but occur reproducibly between experiments.

The early oxidation onset of TEBTT (**Figure 2.2c**) at +0.43 V is comparably much lower than that of BTT, which is expected because of the EDOT unit substitution on the BTT core, further extending the π -conjugated motif. Here, the oxidation potential of TEBTT measured by linear scan is lower than that reported in earlier work by CV (+0.78 V; vs. Ag/Ag⁺),⁸⁶ and we note that experimental uncertainties are not uncommon when measuring redox potentials via conventional CV methods. **Figure 2.2c** provides further insight on the consecutive oxidation features in TEBTT, although it should be noted that the second and third oxidation features ($E_{ox2} = +0.71$ V and $E_{ox3} = +1.32$ V) are somewhat convoluted in the broad redox response of TEBTT in this voltage window. While the first two oxidation peaks ($E_{ox1} = +0.49$ V and $E_{ox2} = +0.71$ V) can be assigned to the oxidation of the EDOT motifs in TEBTT, the third oxidation feature ($E_{ox3} = +1.32$ V) occurs at a

potential close to that of the first oxidation of the BTT motif ($E_{\text{ox}1} = +1.28$ V; **Figure 2.2b**) and can, therefore, reasonably be assigned to the oxidation of a thiophene ring at the core. Consistent with the oxidation peak attribution in BTT at higher potentials ($E_{\text{ox}3} = +2.04$ V; **Figure 2.2b**), the fourth oxidation feature seen for TEBTT ($E_{\text{ox}4} = +1.98$ V) suggests a sequential oxidation of the other thiophene rings at the core.

2.2.2.2 Copolymerization of BTT and EDOT

Considering the close oxidation potentials of BTT ($E_{\text{ox}1} = +1.28$ V; **Figure 2.2b**) and EDOT (+1.02 V; **Figure 2.2a**), the concurrent electropolymerization of the two motifs can be expected to yield copolymers with random compositions. Because PEDOT is one of the most conductive and capacitive polymers reported to date,^{73, 90, 91} copolymers of BTT and EDOT may combine high-capacitance, nanostructured networks that are inherently distinct from those of their respective homopolymers (PBTT and PEDOT). Thus, we examined the electrodeposition of P(BTT/EDOT) copolymers prepared from several monomer solutions of different BTT/EDOT monomer compositions; experiments were performed in ACN on highly porous conducting carbon cloth with a potential window of -0.7–+1.5 V and a scan rate of 50 mV s⁻¹ for 20 cycles. The SEM images shown in **Figure 2.3** illustrate the morphologies of the electrodeposited PBTT (**Figure 2.3a**; 1:0 ratio in BTT/EDOT), P(BTT/EDOT) copolymers (**Figure 2.3b-e**; 3:1, 1:1, 1:3, and 1:6 ratios, respectively), and PEDOT (**Figure 2.3f**; 0:1 ratio). Comparing the film depositions achieved in **Figure 2.3a** (PBTT) and **Figure 2.3f** (PEDOT), the contrasts in electrodeposition yields and morphologies formed on the carbon cloth electrodes are rather obvious, and it is interesting to note that BTT may not electropolymerize as efficiently as EDOT in spite of their

comparable onsets of oxidation. This might be explained by the lower conductivity of PBTT compared to PEDOT (although challenging to measure in non-continuous electropolymerized films), which may affect the propensity of the BTT monomer to electropolymerize further once a critical amount of PBTT is deposited on the carbon cloth. In contrast to the dense nodular morphology and large aggregates (700–2,500 nm) obtained on electropolymerizing EDOT (**Figure 2.3f**), sparser aggregates with high aspect ratios are observable for PBTT (width dispersion: 80–160 nm; length: 400–700 nm). Looking at the intermediate morphologies that develop on copolymerizing BTT and EDOT (depicted in **Figure 2.3b-e**), it is worth noting however that electrodeposited films of P(BTT/EDOT) are more densely nanostructured than those of their PBTT counterpart, showing significant differences in aggregate size distributions. In general, blending BTT and EDOT leads to the electrodeposition of aggregate patterns that are somewhat smaller in size (i.e., more nanostructured) compared to PEDOT films and dependent on the initial BTT/EDOT monomer ratios (**Figure 2.3b**, 3:1 ratio in BTT/EDOT, aggregates: 30-300 nm; clusters: 500-1,000 nm; **Figure 2.3c**, 1:1 ratio in BTT/EDOT, clusters: 400-2,000 nm; **Figure 2.3d**, 1:3 ratio in BTT/EDOT, aggregates: ca. 40 nm; clusters: 1,000-2,000 nm; **Figure 2.3e**, 1:6 ratio in BTT/EDOT, clusters: 200-1,400 nm).

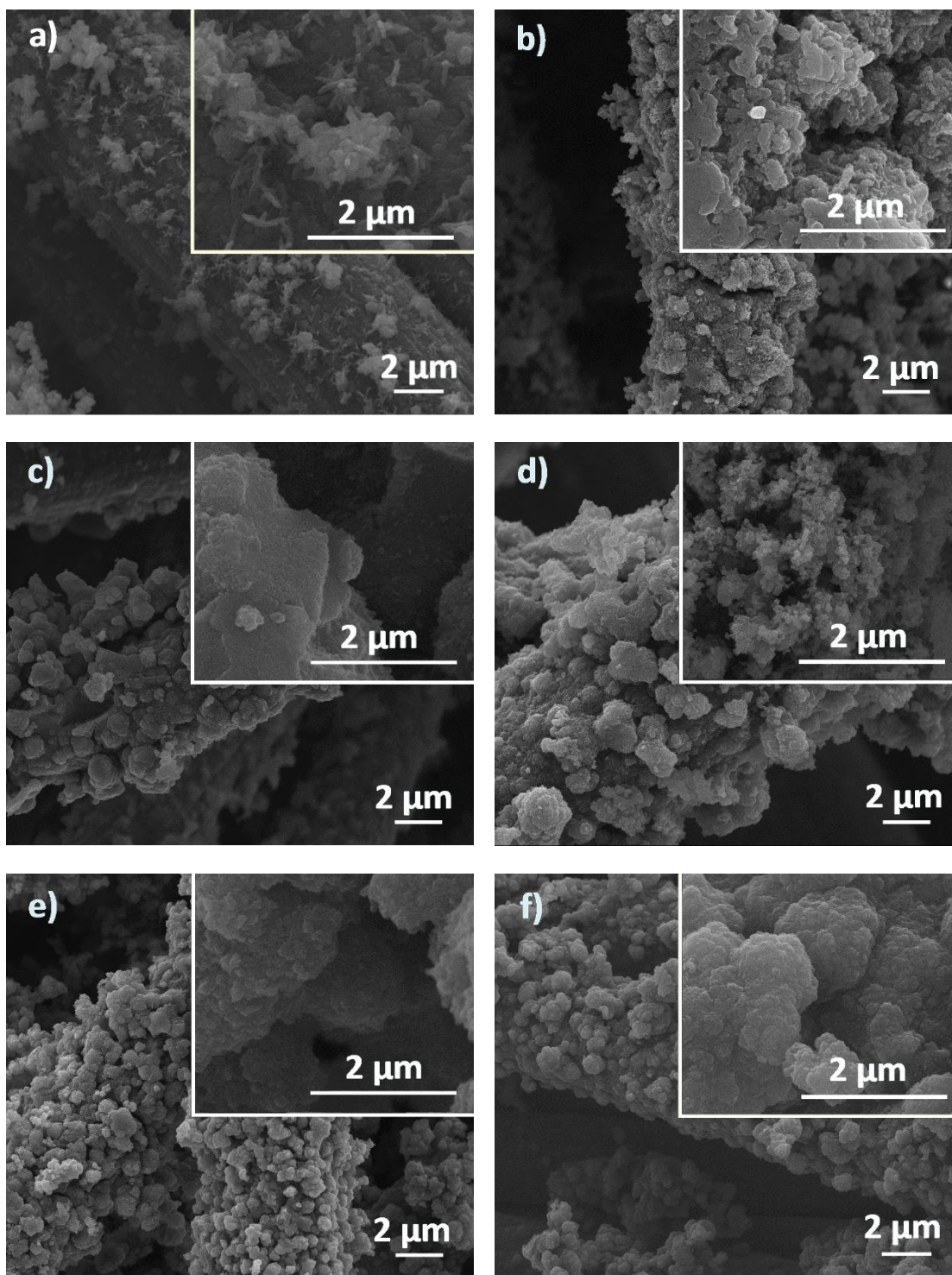


Figure 2.3 SEM images of the morphologies of electrodeposited polymer films prepared from several monomer solutions of different BTT/EDOT monomer compositions: (a) 1:0, (b) 3:1, (c) 1:1, (d) 1:3, (e) 1:6, and (f) 0:1. Electrodeposition conditions: 50 mM monomer

solutions in ACN; 20 deposition cycles in a voltage window of $-0.7 - +1.5$ V (vs. Ag/Ag⁺), on carbon cloth electrodes; deposition scan rate of 50 mV s^{-1} .

2.2.2.3 Electroactivity and Capacitive Properties of PBTT, PEDOT and P(BTT/EDOT)

The electroactivity and capacitive properties of PBTT, PEDOT, and the P(BTT/EDOT) copolymers were measured by CV; the corresponding voltammograms are shown in **Figure 2.4a-b**. For ease of comparison, each voltammogram is normalized to the extent of functionalized surface area, and in **Figure 2.4c** the areal capacitance (Ca) of the electrodeposited polymers is extracted from galvanostatic charge-discharge measurements (the values are shown directly on the plot). By comparing all electrodeposited systems in **Figure 2.4**, we note that PBTT homopolymers exhibit only a modest capacitance value of 73 mF cm^{-2} (at 5 mA cm^{-2}), which is consistent with the lack of reversibility of the broad redox process in the 0.0 to $+0.8$ V voltage window and with the smaller amount of material deposited on the carbon cloth electrode (**Figure 2.3a**). It is interesting to note, however, that considering recently published studies on electropolymerized material systems for supercapacitor applications,^{59, 90, 92, 93} Ca values $>50 \text{ mF cm}^{-2}$ inferred for PBTT remain significant. For comparison, polypyrrole/graphene oxide nanocomposites have been shown to yield 22.8 mF cm^{-2} (at 0.1 mA cm^{-2}),⁹³ while poly(3,4-propylenedioxyppyrrrole)/SWCNT composites attain 16.4 mF cm^{-2} (at 0.9 mA cm^{-2}),⁹² capacitance values that are expected to drop significantly at higher current densities, such as those at which we estimate the capacitance of PBTT (i.e., 5 mA cm^{-2}).

Following the same experimental conditions as those used for the electrodeposition of PBTT, PEDOT-functionalized carbon cloth electrodes yield Ca values of 733 mF cm^{-2} (at 5 mA cm^{-2}), confirming that PBTT homopolymers perform more modestly than PEDOT. Here again, these differences may arise from the lower electronic conductivity of PBTT compared to PEDOT, noting that the thiophene rings in BTT motifs are not in direct conjugation because the central phenyl interferes with the conjugation path between thiophenes. The significant voltage drops (IR-drop) visible in **Figure 2.4c** (2x that seen for PEDOT electropolymerized in the same conditions) reflect energy losses due to internal resistance in films of electrodeposited PBTT, further supporting the argument consistent with the idea that PBTT films may be less conductive than those of PEDOT. It should also be noted that the occurrence of α - β and β - β side-couplings in unsubstituted thiophene-based motifs subjected to electrochemical and oxidative polymerization conditions are known to affect conjugation, and subsequently lower the conductivity, electrochemical cycling stability, and capacitive performance of thiophene-based polymers.^{89, 94, 95} In parallel, and as shown in **Figure 2.4**, the capacitive cycles of the several P(BTT/EDOT) copolymers (see **Figure 2.1b**) electrodeposited and characterized by CV reflect redox behaviors that are somewhat intermediate between those of PBTT and PEDOT. A similar pattern is observed for areal capacitance values, suggesting that long segments of the two homopolymers formed on the carbon cloth electrode.

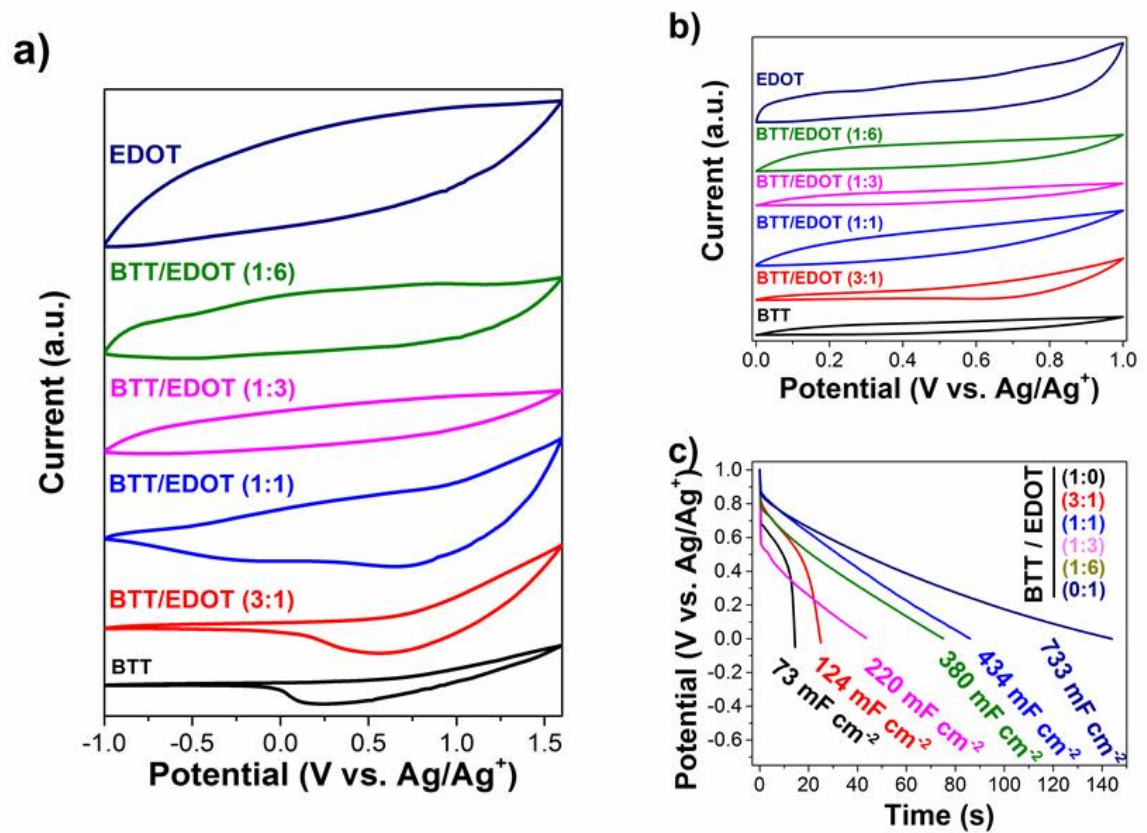


Figure 2.4 (a, b) Cyclic voltammograms of electrodeposited PBTT, PEDOT, and several P(BTT/EDOT) copolymers prepared from several solutions of different BTT/EDOT monomer compositions: 1:0 (black), 3:1 (red), 1:1 (blue), 1:3 (magenta), 1:6 (green), and 0:1 (dark blue) at a scan rate of 20 mV s^{-1} . Electrodeposition conditions: 50 mM monomer solutions in ACN; 20 deposition cycles in a voltage window of $-0.7 - +1.6 \text{ V}$ (vs. Ag/Ag^+), on carbon cloth electrodes; deposition scan rate of 50 mV s^{-1} . Each voltammogram is normalized to the extent of functionalized surface area. (c) Galvanostatic charge-discharge curves collected for the polymers at a current density of 5 mA cm^{-2} ; the areal capacitance values inferred are indicated on the plot.

As an alternative to BTT, and to mitigate the probability of α - β and β - β side-couplings between the thiophene moieties, we turn to the TEBTT motifs, where EDOT units were appended to the BTT core, extending the conjugation of the π -system and further reducing its HOMO/LUMO gap. As a result, and as previously discussed from **Figure 2.2c**, TEBTT exhibits a lower oxidation potential ($E_{\text{ox1}} = +0.49$ V). Because TEBTT is a more extended π -conjugated system, it is only moderately soluble in ACN, but its solubility was found sufficient in DCM (solubility up to 1.25 mM), and the later was used for the electrochemical polymerization of all TEBTT-based polymers. Next, the electrodeposited films were carefully rinsed with DCM and characterized in ACN for consistency with the characterization protocol used for all BTT-based polymers.

First, we studied the optimal conditions for the electrochemical deposition of PTEBTT as a function of voltage window, cycle number, and working electrode with the goal of achieving the best possible Ca values. The corresponding experimental conditions and obtainable Ca values are summarized in **Table 2.1**. **Figure 2.5a** shows the CV curves of PTEBTT films electrodeposited on various working electrodes and voltage windows. In contrast to the lack of reversibility of the broad redox process previously discussed for PBTT, the redox processes for PTEBTT were found to be inherently more reversible (see **Figure 2.6**). As emphasized in **Table 2.1** and **Figure 2.5a**, a voltage window of -0.2+0.8 V was found optimal for PTEBTT with respect to the Ca performance values. The choice of the working electrode (WE) was also found to be an important parameter, with glassy carbon (GC) button electrodes producing polymer films that are electroactive and reversibly cycled over a broader voltage range, suggesting a more adhered, more densely electropolymerized polymeric network (found to yield higher Ca values). In contrast,

attempts to electrodeposit TEBTT on carbon cloth and indium tin oxide (ITO) electrodes did not yield comparably promising results and thus, were not pursued further. Furthermore, because films electrodeposited via alternative deposition techniques such as potentiostatic and pulsed potentiostatic techniques showed only modest capacitive characteristics, we concentrated on CV protocols (**Table 2.1**). PTEBTT films electrodeposited on the GC electrode exhibit an oxidation onset at +0.20 V (**Figure 2.5a**) and a broad quasi-reversible redox couple ($E_{\text{ox}1} = +0.62 \text{ V} - E_{\text{red}1} = +0.27 \text{ V}$) followed by an irreversible oxidation (and related reduction $E_{\text{red}2} = +0.69 \text{ V}$ on the reverse cycle). The SEM image in **Figure 2.6a** shows a distinctly structured morphology on micron-sized fibers densely distributed across the GC surface (width dispersion: 150-200 nm; length: 1,200-1,600 nm) accompanied by some nodular aggregates (800-1,600 nm). From the optimized conditions (WE: glassy carbon button electrode, voltage window: -1.0—+1.2 V, scan rate: 50 mV s⁻¹), we studied the dependence of the capacitive response of PTEBTT as a function of the number of electrodeposition cycles and the scan rate; the corresponding CV curves are shown in **Figure 2.5b-c**. Overall, with PTEBTT, *Ca* values are found to increase with the number of electrodeposition cycles as more electroactive material is deposited on the GC electrode, reaching areal capacitance values as high as 271.1 mF cm⁻² (1 mA cm⁻²) after 120 cycles, which represents a 10-fold improvement compared to PBTT. In addition to the high *Ca* values achieved, **Figure 2.5b-c** emphasize the reversibility of the first redox couple in PTEBTT, which is maintained for films obtained over large numbers of deposition cycles (up to 120 shown in **Figure 2.5b**) and for films cycled over a wide range of scan rates (**Figure 2.5c**). These results indicate that films of electropolymerized PTEBTT are not limited by electronic conductivity or electrolyte

diffusion aspects. As illustrated in **Figure 2.5c**, the redox peak intensities (anodic, I_{pa} , and cathodic, I_{pc}) for electrodeposited films of PTEBTT were found to vary linearly with the square root of the scan rate (correlation factors given in inset), consistent with a reversible system.⁹⁶ The interpolations calculated give $I_{pa} = -0.13(3) v^{1/2} + 2.26(4)$ and $I_{pc} = -0.21(2) v^{1/2} - 1.63(3)$ with v representing the scan rate investigated.

2.2.2.4 Copolymerization of TEBTT and EDOT

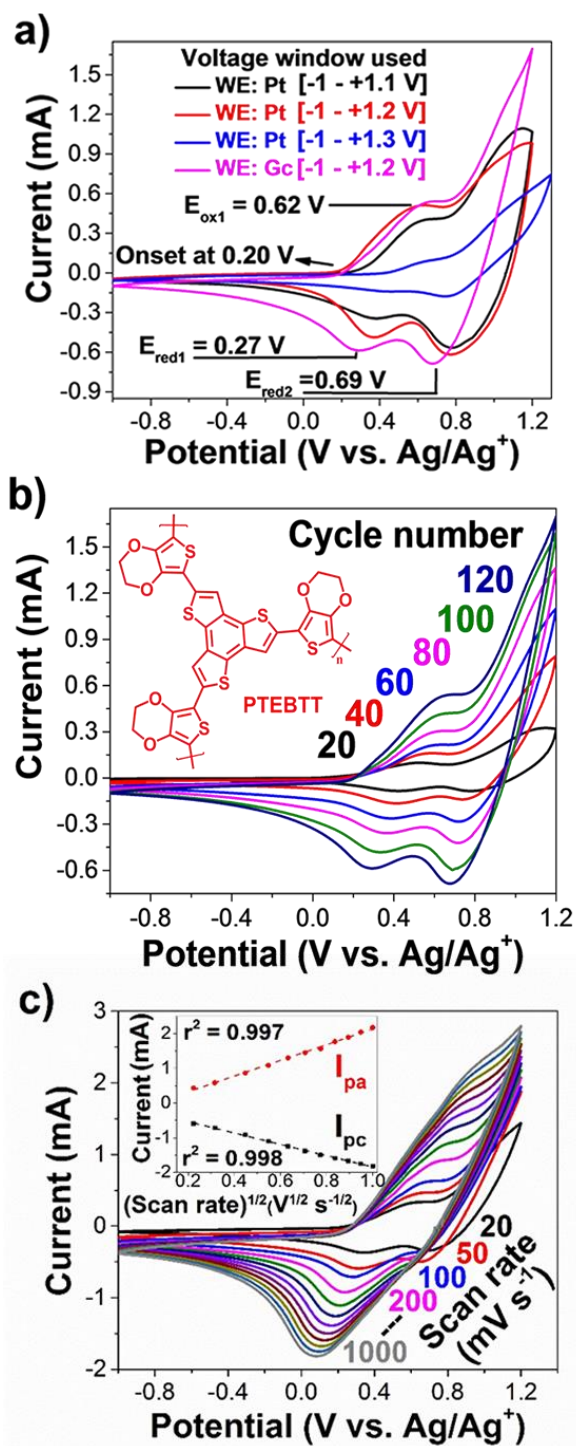


Figure 2.5 (a) Cyclic voltammograms of PTEBTT films electropolymerized on various working electrodes and voltage windows (collected in ACN). Electrodeposition conditions:

1 mM monomer solutions in DCM; 120 deposition cycles; deposition scan rate of 50 mV s^{-1} . **(b)** Cyclic voltammograms of PTEBTT films on glassy carbon button electrodes as a function of the number of electrodeposition cycles (collected in ACN). Electrodeposition conditions: 1 mM monomer solutions in DCM; 120 deposition cycles in a voltage window of $-1.0 - +1.2 \text{ V}$ (vs. Ag/Ag^+); deposition scan rate of 50 mV s^{-1} . **(c)** Cyclic voltammograms of PTEBTT films on glassy carbon button electrodes as a function of scan rate (collected in ACN). Electrodeposition conditions: 1 mM monomer solutions in DCM; 20 deposition cycles in a voltage window of $-1.0 - +1.2 \text{ V}$ (vs. Ag/Ag^+); deposition scan rate of 50 mV s^{-1} . Inset: anodic (I_{pa}) and cathodic (I_{pc}) current intensity variations of the first redox couple of PTEBTT as a function of the square root of the scan rate.

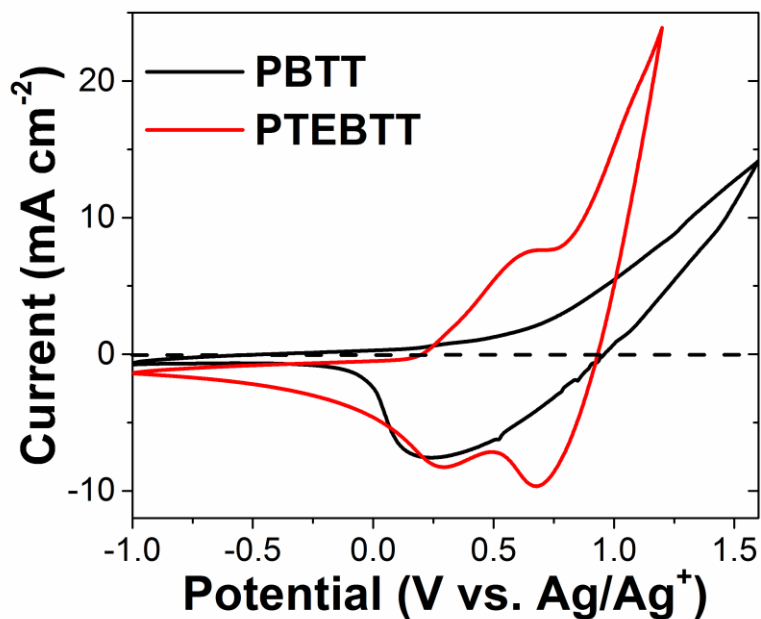


Figure 2.6 Cyclic voltammograms of electrodeposited PBTT and PTEBTT. Electrodeposition conditions of PBTT: scan rate of 50 mV s^{-1} , 20 cycles, voltage window $-0.7 - +1.6 \text{ V}$ (vs. Ag/Ag^+), 50 mM monomer in ACN. Electrodeposition conditions of

PTEBTT: scan rate of 50 mV s^{-1} , 120 cycles, voltage window -1.0 – $+1.2 \text{ V}$ (vs. Ag/Ag^+), 1 mM monomer in DCM. Each voltammogram is normalized to the extent of functionalized surface area.

Table 2.1 Summary of electrodeposition conditions for PTEBTT, PEDOT, and several P(TEBTT/EDOT) copolymers prepared from several solutions of different TEBTT/EDOT monomer compositions (in DCM) and the associated areal capacitance (C_a) values on various working electrodes (WE). Experimental details: deposition scan rate of 50 mV s^{-1} ; all measurements performed in ACN.

Monomer Solution Composition / Concentration	WE	Condition of Electrodeposition	Time/Number of Deposition Cycles	C_a (mF cm^{-2})	Conditions of Measurement
TEBTT/EDOT 1:0 1 mM	Pt	Potentiostatic $I = 1.2 \text{ V}$	20 min	15.6 mF cm^{-2}	1 mA cm^{-2} between $[0 - 0.8 \text{ V}]$
			40 min	44.6 mF cm^{-2}	
			50 min	21.3 mF cm^{-2}	
TEBTT/EDOT 1:0 1 mM	Pt	Pulsed potentiostatic $I_1 = 1.2 \text{ V}$ (1s) $I_2 = -1.0 \text{ V}$ (2s)	600 ($I_1 - I_2$)	40.6 mF cm^{-2}	1 mA cm^{-2} between $[0 - 0.8 \text{ V}]$
			1200 ($I_1 - I_2$)	45.3 mF cm^{-2}	
			1800 ($I_1 - I_2$)	44.1 mF cm^{-2}	
TEBTT/EDOT 1:0 1 mM	Pt	Cycling $[-1 - 1.1 \text{ V}]$	40 cycles	41.6 mF cm^{-2}	1 mA cm^{-2} between $[0 - 0.8 \text{ V}]$
			80 cycles	124.0 mF cm^{-2}	
			120 cycles	184.5 mF cm^{-2}	
TEBTT/EDOT 1:0 1 mM	Pt	Cycling $[-1 - 1.2 \text{ V}]$	40 cycles	61.0 mF cm^{-2}	1 mA cm^{-2} between $[0 - 0.7 \text{ V}]$
			80 cycles	141.0 mF cm^{-2}	
			120 cycles	186.0 mF cm^{-2}	
TEBTT/EDOT 1:0 1 mM	Pt	Cycling $[-1 - 1.3 \text{ V}]$	40 cycles	20.6 mF cm^{-2}	1 mA cm^{-2} between $[0 - 0.8 \text{ V}]$
			80 cycles	55.0 mF cm^{-2}	
			120 cycles	17.9 mF cm^{-2}	
TEBTT/EDOT 1:0 1 mM	GC	Cycling $[-1 - 1.2 \text{ V}]$	40 cycles	29.5 mF cm^{-2}	1 mA cm^{-2} between $[0 - 0.8 \text{ V}]$
			80 cycles	99.0 mF cm^{-2}	
			120 cycles	271.1 mF cm^{-2}	
TEBTT/EDOT 3:1 1 mM	GC	Cycling $[-1 - 1.2 \text{ V}]$	40 cycles	53.7 mF cm^{-2}	1 mA cm^{-2} between $[-0.2 - 0.8 \text{ V}]$
			80 cycles	193.6 mF cm^{-2}	
			120 cycles	323.4 mF cm^{-2}	
TEBTT:EDOT 1:1 2.5 mM	GC	Cycling $[-1 - 1.2 \text{ V}]$	40 cycles	139.0 mF cm^{-2}	1 mA cm^{-2} between $[-0.2 - 0.8 \text{ V}]$
			80 cycles	383.8 mF cm^{-2}	
			120 cycles	443.8 mF cm^{-2}	
TEBTT:EDOT 1:3	GC	Cycling $[-1 - 1.2 \text{ V}]$	40 cycles	99.8 mF cm^{-2}	1 mA cm^{-2}
			80 cycles	127.1 mF cm^{-2}	

5 mM			120 cycles	356.7 mF cm ⁻²	between [-0.2 – 0.8 V]
TEBTT:EDOT 1:9 5 mM	GC	Cycling [-1 – 1.2 V]	40 cycles 80 cycles 120 cycles	59.0 mF cm ⁻² 127.1 mF cm ⁻² 218.0 mF cm ⁻²	1 mA cm ⁻² between [-0.2 – 0.8 V]
TEBTT:EDOT 5:95 5 mM	GC	Cycling [-1 – 1.2 V]	40 cycles 80 cycles 120 cycles	57.7 mF cm ⁻² 125.7 mF cm ⁻² 189.3 mF cm ⁻²	1 mA cm ⁻² between [-0.2 – 0.8 V]
TEBTT:EDOT 0:1 5 mM	GC	Cycling [-1 – 1.2 V]	40 cycles 80 cycles 120 cycles	24.0 mF cm ⁻² 40.3 mF cm ⁻² 55.9 mF cm ⁻²	1 mA cm ⁻² between [-0.2 – 0.8 V]
TEBTT:EDOT 0:1 1 mM	GC	Cycling [-1 – 1.2 V]	120 cycles	12.1 mF cm ⁻²	1 mA cm ⁻² between [0.1 – 0.8 V]

Pt: platinum button electrode; GC: glassy carbon electrode.

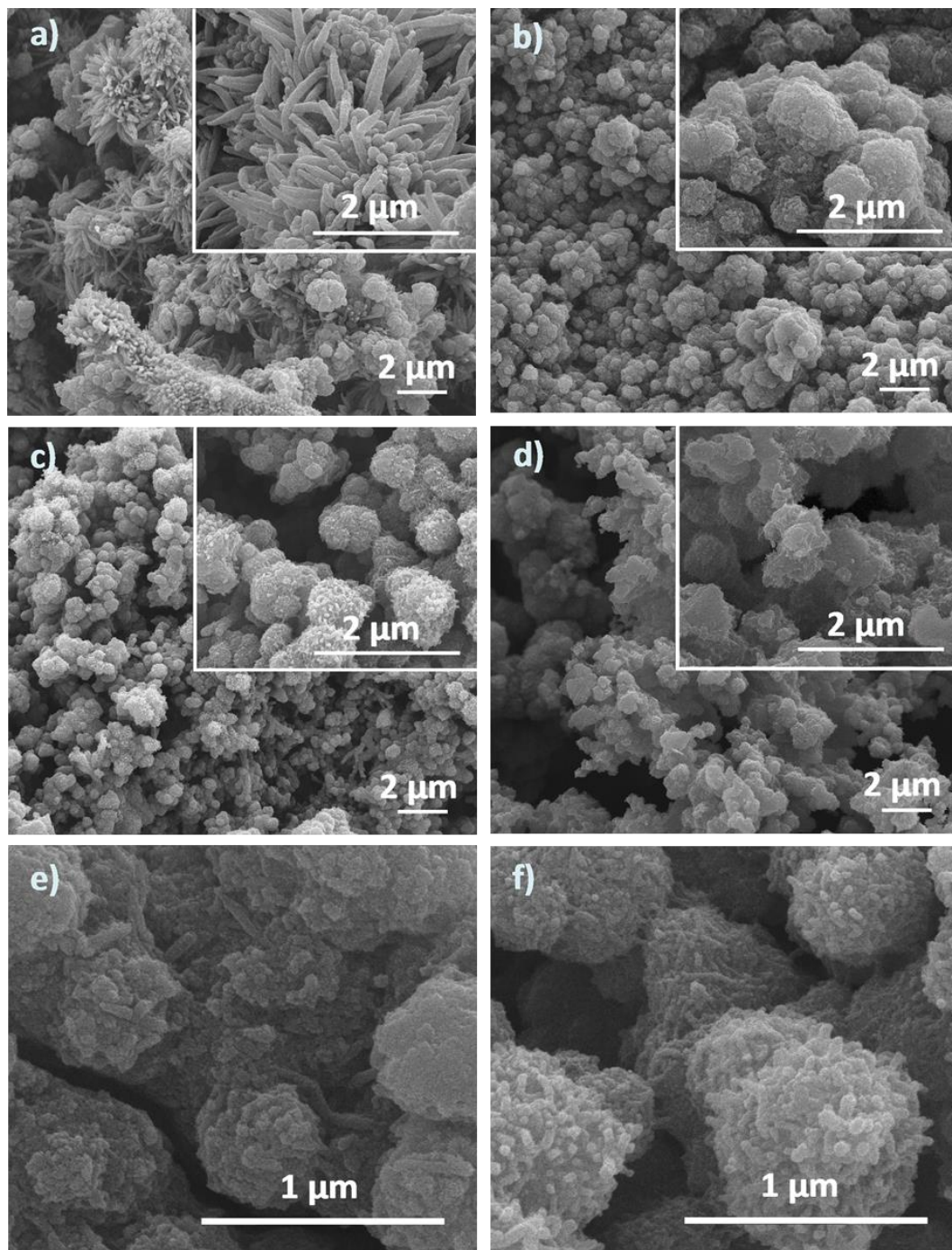


Figure 2.7 SEM images of the morphologies of electrodeposited polymer films prepared from several monomer solutions of different TEBTT/EDOT monomer compositions: (a) 1:0, (b, e) 1:1, (c, f) 1:9, and (d) 0:1. Electrodeposition conditions: 1 mM monomer

solutions in DCM; 120 deposition cycles in a voltage window of -1.0 – +1.2 V (vs. Ag/Ag⁺), on glassy carbon button electrodes; deposition scan rate of 50 mV s⁻¹.

Following the conditions of electropolymerization employed earlier in ACN, now applied in DCM, films of electrodeposited PEDOT yield lower *Ca* values (**Table 2.1**) than those obtained earlier from ACN: PEDOT electrodeposited on carbon cloth from 1 mM and 5 mM monomer solutions yield capacitance values of *ca.* 12 mF cm⁻² and *ca.* 55 mF cm⁻² (at 1 mA cm⁻²), respectively (**Table 2.1**). These lower *Ca* values may result from the lower propensity of the monomer to undergo electropolymerization in the lower dielectric constant solvent DCM ($\epsilon = 8.9$)⁹⁷ (ACN: $\epsilon = 36.6$)⁹⁷ combined with the effect of using a WE that is inherently less porous (on going from carbon cloth to the GC button electrode).^{98, 99} The SEM image in **Figure 2.7d** shows aggregate patterns in a relatively wide size distribution (650-1,000 nm) spread across films that are several micrometers thick.

Next, we prepared P(TEBTT/EDOT) copolymers by electrodeposition from several solutions of different TEBTT/EDOT monomer compositions; electrodeposition conditions: 1 mM monomer solutions in dichloromethane (DCM); 120 deposition cycles in a voltage window of -1.0 – +1.2 V (vs. Ag/Ag⁺), on glassy carbon (GC) button electrodes; deposition scan rate of 50 mV s⁻¹. As depicted by the SEM images shown in **Figure 2.7b** and **Figure 2.6c**, the P(TEBTT/EDOT) copolymers exhibit morphologies that are fairly distinct from those of their homopolymer counterparts, PTEBTT and PEDOT. In particular, the higher-magnification SEM images shown in **Figure 2.7e-f** indicate that the aggregate patterns formed are highly nanostructured (**Figure 2.7b&e**, 1:1 ratio in

TEBTT/EDOT, aggregates: <100 nm; clusters: 500-1,200 nm; **Figure 2.7c&f**, 1:9 ratio in TEBTT/EDOT, aggregates: <50 nm; clusters: 600-1,000 nm). Here, we note that the dense, highly textured hierarchical P(TEBTT/EDOT) networks formed are consistent with the values of high areal capacitance given in **Table 2.1**. The CV curves of the electrodeposited P(TEBTT/EDOT) polymers shown in **Figure 2.7a** reflect inherently more capacitive material systems compared to their homopolymer counterparts, PTEBTT or PEDOT; observations consistent with the higher Ca values obtained for the copolymers and summarized in **Table 2.1**, reaching up to 443.8 mF cm^{-2} (at 1 mA cm^{-2}) (1:1 ratio in TEBTT/EDOT). In particular, copolymers that result from the addition of only 5 mol.% of TEBTT in the initial TEBTT/EDOT monomer solution exhibit significantly higher Ca values compared to PEDOT: 189 mF cm^{-2} vs. 12 mF cm^{-2} (at 1 mA cm^{-2}), respectively, representing a ca. 15-fold capacitance increase. These results suggest that TEBTT motifs play a critical role in the development of open, hierarchical morphologies required to maximize areal capacitances and promote electrolyte diffusion in conventional electropolymerized π -conjugated systems such as PEDOT. **Figure 2.8** also shows how the capacitive cycles of the several P(TEBTT/EDOT) copolymers electrodeposited and characterized by CV reflect redox behaviors that are not intermediate between those of PTEBTT and PEDOT—an observation that points to a random integration of TEBTT and EDOT monomers during the electropolymerization step.

Figure 2.8b-c depict the areal capacitance of PTEBTT, PEDOT, and the P(TEBTT/EDOT) copolymers obtained from the electropolymerization of several TEBTT/EDOT monomer compositions (3:1, 1:1, 1:3, and 1:9 ratios) as a function of current density (**Figure 2.8b**) and cycle number (**Figure 2.8c**). It is interesting to note that

several P(TEBTT/EDOT) copolymers (1:1, 1:3, and 1:9 ratios) undergo only little capacitance variations with current density increments, suggesting excellent electrolyte diffusion within the highly porous P(TEBTT/EDOT)-based frameworks. **Figure 2.8c** shows that films of electrodeposited PTEBTT are relatively resilient to repeated electrochemical cycling with *ca.* 73% of capacitance retained (at 2 mA cm⁻²) over 1,000 cycles (vs. 96% for PEDOT over 1,000 cycles (at 2 mA cm⁻²). Here, we note that our estimate of the stability of the homopolymer PTEBTT is on the low end of the capacitance retention reported in prior work (*ca.* 95% over 1,400 cycles),⁸⁶ a difference that is likely to stem from the significantly thicker films examined in this study: PTEBTT is electrodeposited in 120 cycles between -1.0 and +1.2 V vs. only 8 cycles between 0.0 and +1.0 V in earlier work.⁸⁶ Likewise, all of the P(TEBTT/EDOT) copolymers show >70% of capacitance retention (at 2 mA cm⁻²) over 1,000 cycles (with up to *ca.* 89% achieved), demonstrating satisfying long-term stability upon repeated electrochemical cycling. These stability figures, ranging between those of PTEBTT and PEDOT, are greater than those reported for some of the more conventional conjugated polymers such as 50% capacitance retention over 1,000 cycles (at 2 mA cm⁻²) for polypyrrole,⁶⁵ 84% capacitance retention after 200 cycles for poly(3-methylthiophene) (longer cycling times not provided), and 70% capacitance retention after 1,000 cycles for PANI.^{26, 65} Last, we note that the mechanical stability and long-term cycling performances of the P(TEBTT/EDOT)-based frameworks may be further improved in hybrid carbon-based composite systems including carbon nanotubes or graphene oxide; however this falls beyond the scope of this report.⁶⁶

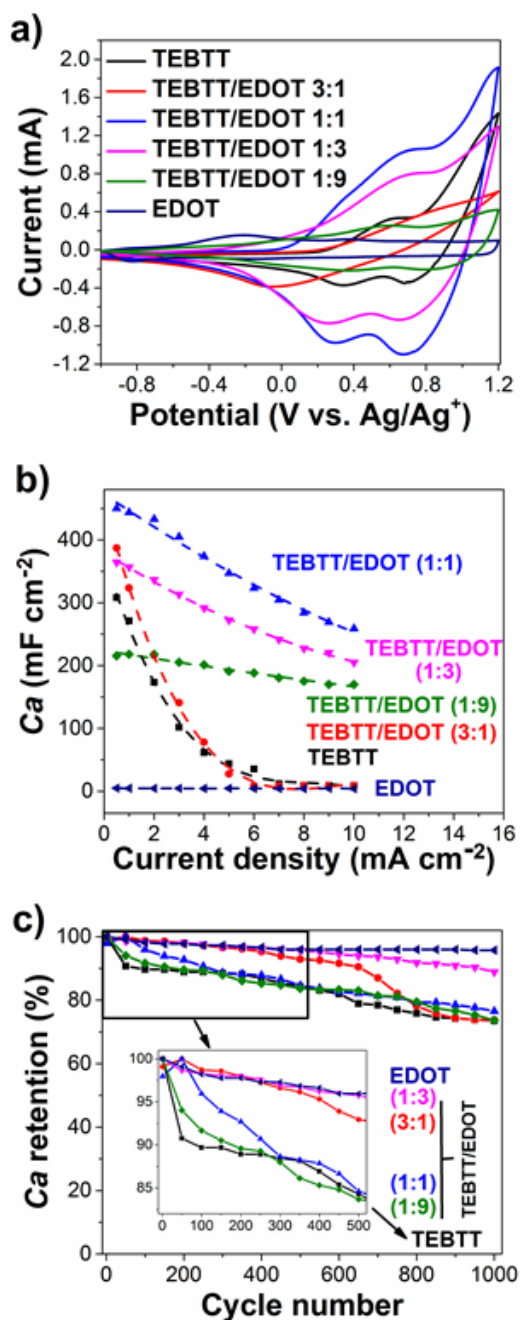


Figure 2.8 (a) Cyclic voltammograms of electrodeposited PTEBTT, PEDOT, and several P(TEBTT/EDOT) copolymers prepared from several solutions of different TEBTT/EDOT monomer compositions: 1:0 (black), 3:1 (red), 1:1 (blue), 1:3 (magenta), 1:9 (green), and 0:1 (dark blue); curves collected at a scan rate of 20 mV s⁻¹.

Electrodeposition conditions: 1 mM monomer solutions in DCM; 120 deposition cycles in a voltage window of $-1.0 - +1.2$ V (vs. Ag/Ag⁺), on glassy carbon button electrodes; deposition scan rate of 50 mV s^{-1} . (b) areal capacitance vs. current density increments for several P(TEBTT/EDOT) copolymers. (c) areal capacitance vs. cycle number for several P(TEBTT/EDOT) copolymers (at 2 mA cm^{-2}).

2.2.3 Conclusion

In summary, we have shown that high-surface-area π -conjugated polymeric networks can be synthesized via the electrochemical copolymerization of the 2D (trivalent) motifs benzo[1,2-*b*:3,4-*b'*:5,6-*b''*]trithiophene (BTT) and tris-EDOT-benzo[1,2-*b*:3,4-*b'*:5,6-*b''*]trithiophene (TEBTT) with EDOT. Of all the material systems studied, P(TEBTT/EDOT)-based frameworks achieved the highest areal capacitance with values as high as 443.8 mF cm^{-2} (at 1 mA cm^{-2}), higher than those achieved by the respective homopolymers (PTEBTT and PEDOT) in the same experimental conditions of electrodeposition (PTEBTT: 271.1 mF cm^{-2} (at 1 mA cm^{-2}); PEDOT: 12.1 mF cm^{-2} (at 1 mA cm^{-2}). The high areal capacitance achieved with P(TEBTT/EDOT) copolymers—with up to *ca.* 30-fold capacitance increases compared to PEDOT—can be related to the open, highly porous hierarchical π -conjugated frameworks formed during the electropolymerization step. We find that both PTEBTT- and P(TEBTT/EDOT)-based frameworks are resilient to repeated electrochemical cycling, maintaining $>70\%$ capacitance over 1,000 cycles (up to 89% achieved), making them promising systems for high life cycle capacitive electrode applications. Lastly, the use of 2D motifs such as TEBTT in the synthesis of electropolymerized hierarchical π -conjugated frameworks with

particularly high areal capacitance may be applicable to other established capacitive polymeric systems such as polythiophenes, polypyrrole, and PANI.

Chapter 3

How Doping Influences EDOT and its Derivative's Electrochemical Properties – the role of anions in the Electropolymerization process

3.1 Introduction and Background

Besides tremendous interests and potentials in investigations of organic devices from energy harvesting⁵³ to electrochromic displays,^{54, 100} electroactive conjugated polymers (ECPs) are emerging as attractive candidates for electrochemical energy storage applications.^{6, 55} This is contributed to their good intrinsic conductivity in the doped state,^{56, 57} much lower band gaps compared with conventional polymers (10 eV),⁵⁴ relatively fast doping and undoping process, the ease of synthesis, and tunable electronic and structural properties through structural modifications^{26, 58, 59} and high specific capacitances.⁶³

In electrochemical process, the suitable choice of appropriate electrolytes to enlarge the safe working potential window with electrolyte stability is well known to improve ECPs' performance in ESCs applications. Ionic liquids (ILs) are ion composed salts and usually fluid over a wide temperature range with low melting points. Protected with inert gas to



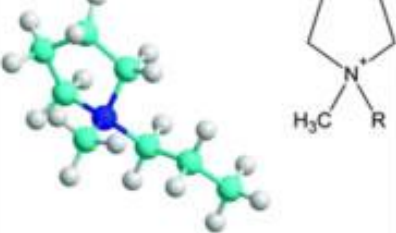
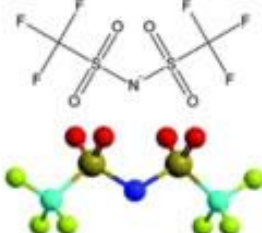
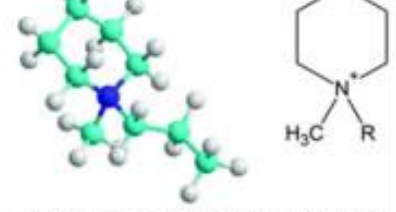
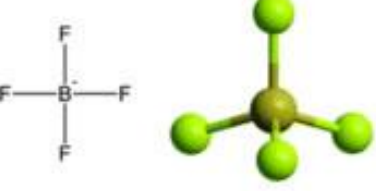

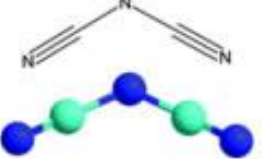
avoid the gaseous products generated at cathode and anode, the working potential window when ILs is used as supporting electrolyte can be improved by almost 1.5–2 times than that of aqueous electrolytes with acid-base.¹⁰¹ ILs have been applied as supporting medium for various devices and materials processing applications in both industry and academia, overcoming the limitation of volatile organic compounds (VOCs).¹⁰²⁻¹⁰⁴ Especially, ILs have been utilized as superior medium to electrodeposit metals, alloys, semiconductors and ECPs in the application of supercapacitors.¹⁰⁵⁻¹⁰⁸ This is mainly contributed to their unique characteristics including intrinsic ion and high ionic conductivity, broad electrochemical voltage windows in neutral conditions, instant ion mobility during redox reaction processes, extremely low vapor pressure, environmental stability;^{103, 106, 107, 109, 110} and numerous, however partly understood, cation/anion effects plays a role to influence the hierarchical morphology and particle size of deposits.

It is well known that for an IL, the size and symmetry of cation plays an important role for its physical properties (e.g. melting point) whereas the anion has more influence towards its stability and chemical reactivity.¹⁰⁷ Due to the combinations of various cations and anions, there is a plethora of different ILs already available and can still be a tremendous long list of potential ILs, the ionic structures and properties of which can be designed and adjusted artificially to accommodate different purposes and applications.^{104, 107} Considering the usage of ILs for the ECPs synthesis, there has been some investigations based on relative small varieties of ILs. The magnitude of the cation can be adjusted accordingly by tailoring the alkyl substituent's chain length. Usually, planar aromatic cations, represented by imidazolium is preferred rather than its analogues with non-planar configurations which can be pyrrolidinium, due to the enhanced cation intercalation,

superior fluidity and conductivity of the plane configuration.^{106, 111} **Table 3.1** shows the range of nitrogen-based cations which are commonly used. Also, during the polymer growth process and electrochemical cycling, it is interesting to note that the nature of these anions can act as dopants, which play a role in the extent of their intercalation into the polymers.¹⁰⁶ Together with doping effect of anions, it is possible that cation/anion is able to influence the polymer's crystal size and as a consequence the morphology of those deposits, which plays a crucial role for the overall electroactive performance of ECP. Motivation for the use of PTh instead of PAn or PPy in supercapacitor application stems from the fact that a relative broader potential window (~1.2 V) can be achieved with PTh, as most of these can be n- and p-doped because of a smaller band gap.^{112, 113} Amongst PTh-based organic conducting polymers, poly (3,4-ethylenedioxythiophene) (PEDOT) and its derivatives have been explored as a most popular and extensively studied electroactive material due to their high electrochemical stability and fast cycle switching speed.^{100, 114} Polythiophene, as well as substituted polythiophenes, have been synthesized by electrochemical polymerization and characterized in ILs, containing Trifluoromethanesulfonate [OTf]-, hexafluorophosphate [PF₆]-, sulfonated aromatics or bis(trifluoromethanesulfonyl)amide [NTf₂]- anions and so on, to yield significant increased currents and higher stability than carried out in common organic solvents dissolving conducting salts, making them of tremendous interest for electrochemical supercapacitor.^{106, 108, 111, 115-122} Electropolymerization of thiophenes have been studied in imidazolium or pyrrolidinium-based ionic liquids as the growth medium and the supporting electrolyte, to assess the influence of the anions on morphology formation and electrochemical activity of these conducting polymers.^{111, 119} However, there is no systematic study on how the

anions of ILs and common organic solution with salt could play a role as a medium both for polymerization and post-polymerization electrolyte for PEDOT and PEDOT-similarity. Here we put an effort to study the electrochemical behavior of PEDOT in ILs for fundamental investigation. There is tremendous potential to clarify the role of the separate anions and cations and how they would affect the electrochemical behavior of electroactive polymers. In this study, imidazolium-based ionic liquids with three different types of anions which are 1-Butyl-3-methylimidazolium bis(trifluoromethylsulfonyl)imide ([bmim][Tf₂N]), 1-Butyl-3-methylimidazolium trifluoromethanesulfonate ([bmim][TfO]), 1-butyl-3-methylimidazolium hexafluorophosphate ([bmim][PF₆]) were used as growth medium and supporting electrolyte to assess the influence of the nature of these anions on the morphology and electrochemical activity of PEDOT. It is found PEDOT produced in ILs shows much slower growth rate and orderly morphologies than grown in an organic electrolyte with TBPPF₆. Some CVs of the polymers show multiple redox peaks, the possible reasons and origins are discussed. The synthesized polymer can be affected greatly by both the ILs with different anion/cation, and its mutual interaction with targeted monomer. The same protocol has been carried out for a PEDOT-similarity, which is 4,4'-dimethoxy-3,3'-bithiophene (BEDOT). It can be pertinent to refer to this study when designing suitable ionic liquids for PEDOT and its analogues for investigation and optimization of electrochemical systems, such as batteries and supercapacitors.

Table 3.1 A selection of cations and anions used to make ionic liquids.

Cations	Anions
 <p><i>N,N</i>-diethyl-<i>N</i>-methyl-<i>N</i>-(2-methoxyethyl) ammonium, [DEME]⁺</p>	 <p>Bis(fluorosulfonyl)imide, [FSI]⁻</p>
 <p><i>N</i>-methyl-<i>N</i>-alkyl pyrrolidinium, [C_nmpyr]⁺</p>	 <p>Bis(trifluoromethanesulfonyl)amide, [NTf₂]⁻</p>
 <p><i>N</i>-methyl-<i>N</i>-alkyl piperidinium, [C_nmpip]⁺</p>	 <p>Tetrafluoroborate, [BF₄]⁻</p>
 <p>1-alkyl-3-methylimidazolium, [C_nmim]⁺ R=Et [emim]⁺ R=Bu [bmim]⁺ R=Hex [hmim]⁺</p>	 <p>Dicyanamide, [dca]⁻</p>

* R groups – typically ethyl, propyl, butyl.

3.2 The Study on Electropolymerization of EDOT and BEDOT and the Post-polymerization Electrochemical Properties

3.2.1 Experimental Section

3.2.1.1 Synthetic Procedures

4,4'-dimethoxy-3,3'-bithiophene (BEDOT) were synthesized in the lab. All monomers were characterized by ^1H NMR (400 MHz) and ^{13}C NMR (100 MHz) on a Bruker Advance III Ultrashielded 400 Plus instrument at room temperature. The ^1H , ^{13}C spectra were referenced according to the tetramethylsilane (TMS) internal standards. High-resolution mass spectrometry (HRMS) data was recorded using an LTQ Orbitrap Velos MS (Thermo Fisher Scientific) in the positive atmospheric pressure photoionization (+APPI) mode. Elemental analyses were performed on a Flash 2000 - Thermo Scientific CHNO Analyzer.

3.2.1.2 Electropolymerization Procedure and Electrochemical Measurements

All electrochemical measurements were performed in a standard three-electrode cell which is connected with a Versastat 4 potentiostat/galvanostat (Princeton Instrument). Carbon paper (CP) was cut into strips and sonicated in ethanol, afterwards dried overnight at 60 °C under vacuum. Each strip was wrapped partially by parafilm with a bare surface area $\sim 0.7 \times 0.7 \text{ cm}^2$ on the front edge. These parafilm covered CP strips were used as working electrode substrates for electrodeposition. A platinum wire was the counter electrode, and the reference electrode was a nonaqueous Ag/Ag⁺ electrode, consisting of a silver wire immersed in an acetonitrile solution of 10 Mm AgNO₃ and 0.1 M

tetrabutylammonium perchlorate (TBAP). Ionic liquids of HPLC grade and 3,4-ethylenedioxythiophene monomers (EDOT, 97%) was purchased from Sigma Aldrich and used as received. In this study, Ionic liquids of 1-Butyl-3-methylimidazolium bis(trifluoromethylsulfonyl)imide ([bmim][Tf₂N]), 1-Butyl-3-methylimidazolium trifluoromethanesulfonate ([bmim][TfO]), 1-butyl-3-methylimidazolium hexafluorophosphate ([bmim][PF₆]) was used. Anhydrous acetonitrile (ACN) from Sigma Aldrich with 100 mM tetrabutylammonium hexafluorophosphate (TBAPF₆) is applied as supporting electrolyte. To investigate the how ILs and organic electrolyte affect the growth and electroactivity of EDOT and its similarity, 25 mM EDOT dissolved in [bmim][Tf₂N] or TBAPF₆/ACN was applied as the growth medium in a standard three-electrode cell. PEDOT was electro-deposited onto CP electrode by cyclic voltammetry with scanning potential between -1.0 and +1.2 V vs. Ag/Ag⁺ and varied potential cycles (scan rate 50 mV/s). After electrochemical cycling, CP substrate's bare surface uncovered by parafilm was deposited with PEDOT. In order to remove the residues and unreacted monomers, CP substrate was rinsed with dropcasted fresh IL or acetonitrile which is consistent with the growth medium. Either [bmim][Tf₂N] or TBAPF₆/ACN is used as supporting electrolyte for electrochemical measurements. The same protocol has been carried out for EDOT in [bmim][TfO] and [bmim][PF₆]. The presence of oxygen can affect the electrochemical synthesis of a conducting polymer for the possibility to form hydroxide at the electrode and react with radical intermediates of polymers.¹⁰⁶ All of the experiment was carried out in an Ar-protected glovebox.

In the post-polymerization cyclic voltammetric experiments, each electrode was scanned with scan rate of 20 mV/s for three times. In the charge and discharge experiments

the polymer film was cycled three times within the potential range consisted with CV window.

The areal capacitance (Ca) of electrodeposited polymeric materials was calculated from the charge-discharge curves through the following general equation:⁸⁷

$$Ca = I^* \Delta t / \Delta V ,$$

where Ca is expressed in mF cm^{-2} and the constant current (I) is applied in mA cm^{-2} ; Δt is the discharging time (in seconds) and ΔV is the potential change (in V).⁸⁷ In this report, we discuss and emphasize Ca values (as opposed to the gravimetric capacitance Cs) by using a measurement of the functionalized surface area that is more accurate than measuring the exact mass of the electrodeposited polymeric material.

3.2.2 Results and Discussion

3.2.2.1 Electrochemical Polymerization and Characterizations of EDOT

It is widely accepted that the electrochemical performance of ECPs-based supercapacitor can be largely determined by the interaction of the electroactive conjugated polymers with the electron collector. Electron collectors are usually conducting substrate/steel, which can be carbon cloths, carbon fibers, porous carbon papers (CPs). In this experiment, in order to minimize the effect of other parameters, CPs have been chosen as electrode substrate. **Figure 3.1a-d** shows the cyclic voltammograms for increased polymerization cycles at a scan rate of 50 mV/s for CP electrodes in a solution of 25 mM EDOT monomer in ACN containing 100 mM TBAPF₆ or pure ILs, which are

[bmim][Tf₂N], [bmim][TfO] and [bmim][PF₆], respectively. As known, if there are more electroactive materials deposited onto the electrode, there will be higher current signals in correspond with the linearly swept voltage. It can be shown from the cyclic voltammograms of PEDOT electrochemical deposited in these different kinds of ILs or organic electrolyte, that the highest redox currents of polymer was obtained during the deposition in TBAPF₆/ACN in **Figure 3.1a**, and the lowest from [bmim][PF₆] in **Figure 3.1d**. However, it is also interesting to note that in TBAPF₆/ACN, the current density per surface area quickly saturated within the first 40 cycles, and decreased with additional cycles, which indicate PEDOT underwent faster polymerization process compared with ionic liquids until the grown film is too thick. Beside [bmim][PF₆], which shows very tiny current density and not significant increase over cycling, PEDOT electropolymerized in [bmim][Tf₂N] (**Figure 3.1b**) and [bmim][TfO] (**Figure 3.1c**) shows smooth and continuous increase of current over additional cycles, which may contribute to the slowly and gradually growth of PEDOT in these ILs. In electrochemical polymerization process, the radical coupling and oxidation of monomers took place at the interface of the CP electrode surface and electrolyte where PEDOT deposition were accumulated. Due to the strong electrostatic and other interaction forces, ILs' viscosity is 10 to 100 times higher compared with water and organic solvents, which affects on the diffusion rate within the ILs and results in the smaller diffusion coefficients and lower ionic conductivity.¹⁰⁴ Hence, it is reasonable to envision viscosity of ILs can also play a significant role in the electrochemical polymerization process. According to diffusion rates, it could be expected that in the low viscous organic solvent electrolyte, these accumulated polymers and oligomers near the electrode will be more easily to diffuse away than in ILs species.

Meanwhile, the unreacted monomers are also more flexible to diffuse onto the interfacial place and more materials can be polymerized and deposited. It is speculated ILs with higher viscosity is helpful for further oligomers oxidation and polymers deposition onto the electrode by accumulation, while lower viscosity facilitates fast polymerization to diffuse away into the bulk distributed in the whole medium. It can be observed after the first several cycles that EDOT monomer solution of TBAPF₆/ACN turned dark thoroughly while EDOT/IL solution was brown with transparency. ILs composed by larger ions or charge delocalized ions usually have lower viscosity, so ILs with anions such as (CF₃SO₂)N⁻ and CF₃SO₃⁻ tend to be more viscous than that of PF₆⁻.¹⁰⁶ The viscosities of these imidazolium type ILs is [bmim][Tf₂N] (69 η/cP) < [bmim][TfO] (93 η/cP) < and [bmim][PF₆] (450 η/Cp).^{123, 124} The preference of high viscosity is not always the case seen for [bmim][PF₆] and there are other factors.

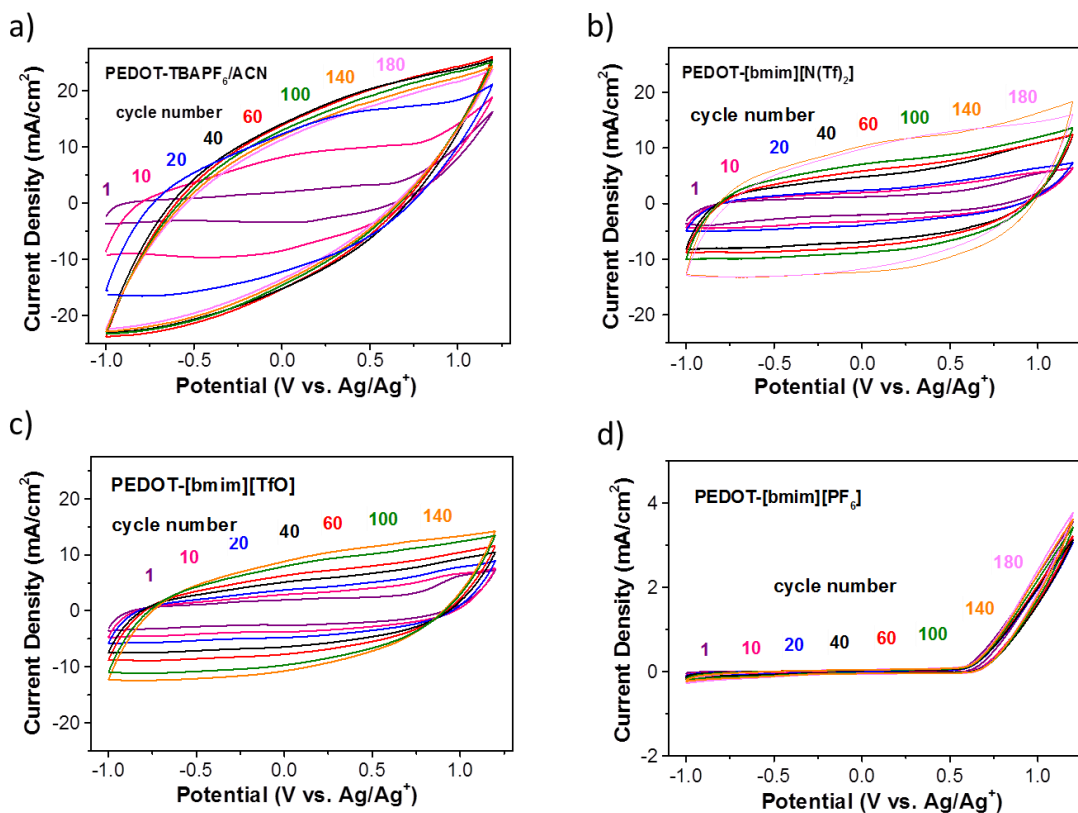


Figure 3.1 Cyclic voltammograms during electropolymerization of EDOT with increased cycles prepared from (a) TBAPF₆/ACN, (b) [bmim][Tf₂N], (c) [bmim][TfO], and (d) [bmim][PF₆] Electrodeposition conditions: 25 mM monomer solutions in supporting medium; 20-180 deposition cycles in a voltage window of -1.0 – +1.2 V (vs. Ag/Ag⁺), on carbon paper electrodes; deposition scan rate of 50 mV s⁻¹. Each voltammogram is normalized to the extent of functionalized surface area.

To assess the electrochemical activities of these conducting polymer films deposited on the substrate and its redox process, cyclic voltammetry (CV) process is carried out. The CVs collected during the electrochemical deposition and increased cycling of EDOT in four kinds of supporting electrolyte is shown in **Figure 3.1 (a)-(d)**. The electrolyte system used as cycling medium can strongly affect the electrochemical response of the polymers. It can

be seen that in **Figure 3.1(a)-(c)**, the growth CVs of PEDOT shows an increase in current density with successive cycles, indicating continuous PEDOT deposition and successful film growth on the substrate. Among these, EDOT electrodeposited in TBAPF₆/ACN shows the highest current density, whereas in **Figure 3.1 (d)**, PEDOT electrodeposited in [bmim][TfO], the current density is extremely low and there is almost no significant current increase. This can be explained by little PEDOT deposited in this kind of ionic liquid.

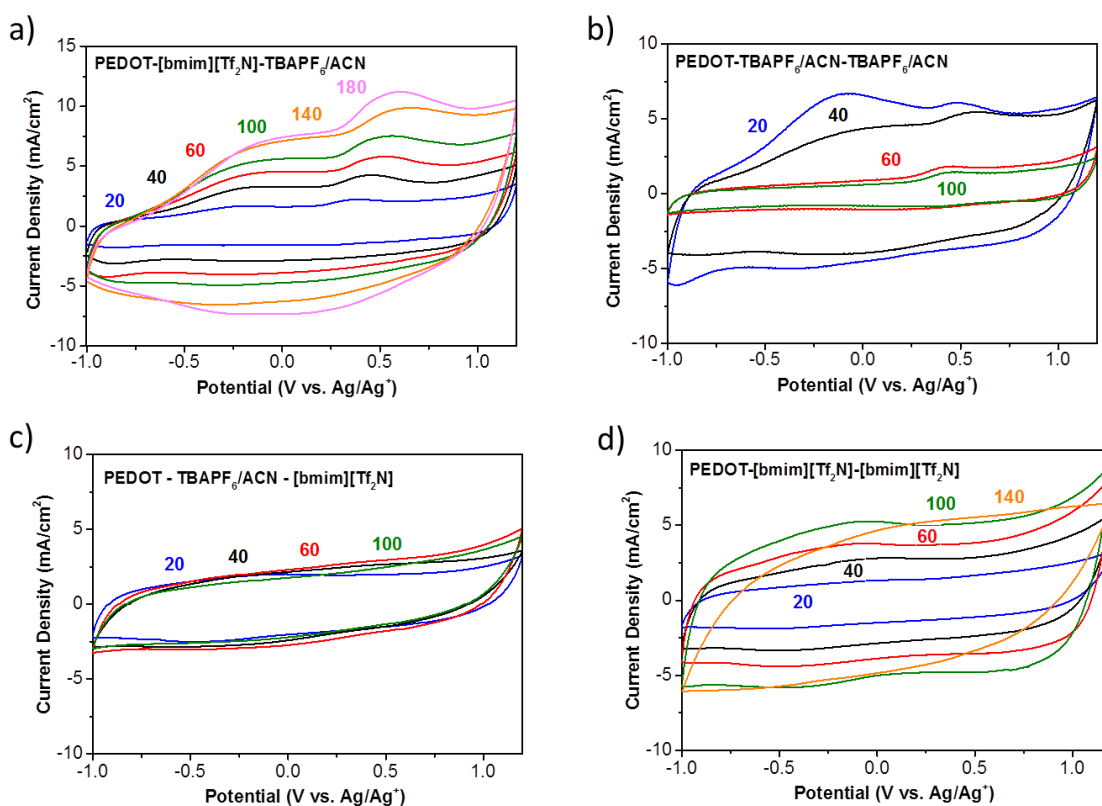


Figure 3.2 Cyclic voltammograms of PEDOT electrodeposited and post-electropolymerization CV in different combinations of ILs and organic solvents. (a) [bmim][Tf₂N] as electrodeposition medium and TBAPF₆/ACN as post-electropolymerization electrolyte; (b) TBAPF₆/ACN as both electrodeposition medium and post-electropolymerization electrolyte; (c) TBAPF₆/ACN as electrodeposition medium and [bmim][Tf₂N] as post-electropolymerization electrolyte; (d) [bmim][Tf₂N] as both electrodeposition medium and post-electropolymerization electrolyte.

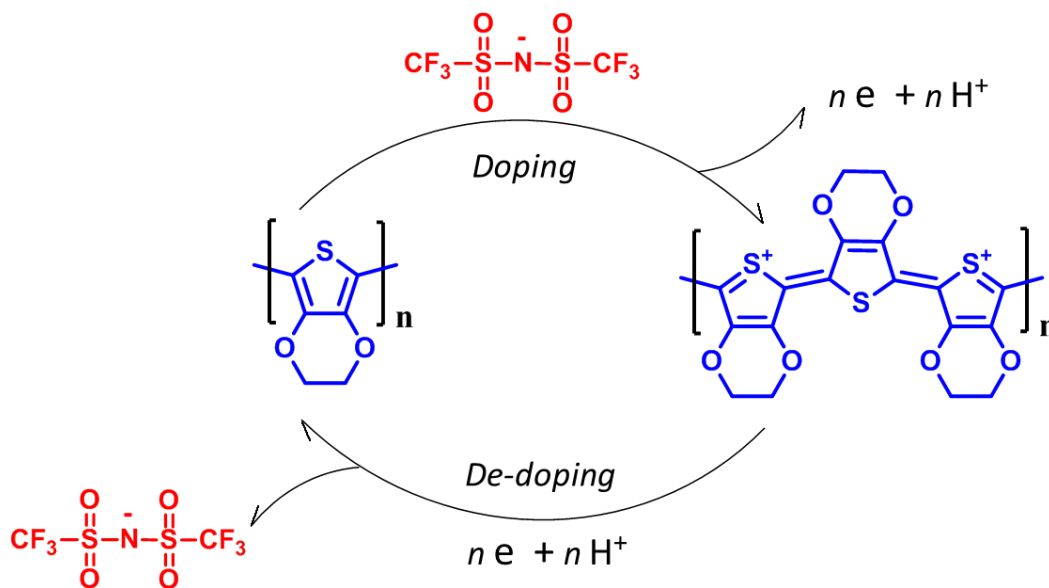
and [bmim][Tf₂N] as post-electropolymerization electrolyte; **(d)** TBAPF₆/ACN as both electrodeposition medium and post-electropolymerization electrolyte, with a voltage window of -1.0 – +1.2 V (vs. Ag/Ag⁺) and scan rate of 20 mV s⁻¹. Each voltammogram is normalized to the extent of functionalized surface area.

In **Figure 3.2a**, following the electropolymerization, the carbon paper composed of the deposited PEDOT polymer film in [bmim][Tf₂N] was removed from the growth electrolyte. PEDOT prepared in [bmim][Tf₂N], was rinsed with ACN and transferred into monomer-free ACN/TBAPF₆ in which the post-polymerization CVs were carried out. This batch of sample is named PEDOT-[bmim][Tf₂N]-ACN/TBAPF₆. When either ACN/TBAPF₆ or [bmim][Tf₂N] was used as the growth medium and ACN/TBAPF₆ is used as after-growth CV electrolyte (**Figure 3.2a-b**), polymer films grown in [bmim][Tf₂N] gives higher current response, this can be contributed to a slower, more ordered polymer structure growth, which is consistent with the electropolymerization results in **Figure 3.1a-b**. The same trend can be observed in **Figure 3.2c-d**. It can also be noted that the redox current charge during the post-polymerization CV is much higher in ACN/TBAPF₆ than [bmim][Tf₂N], when comparing PEDOT-ACN/TBAPF₆-ACN/TBAPF₆ (**Figure 3.2b**) and PEDOT-ACN/TBAPF₆-[bmim][Tf₂N] (**Figure 3.2c**), as well as PEDOT-[bmim][Tf₂N]-ACN/TBAPF₆ (**Figure 3.2a**) and PEDOT-[bmim][Tf₂N]-[bmim][Tf₂N] (**Figure 3.2d**), suggesting superior electrochemical activity in lower viscous organic solvent. It is known from the growth CVs in Figure 3.1a-d that the electrochemical response of PEDOT depends greatly on the nature of the ionic liquid applied. So, the post-polymerization CVs of PEDOT shows there is influence for both the growth medium in which PEDOT

deposited, and the nature of the supporting electrolyte used in the post-polymerization cycling.^{106, 117} CVs of these polymer films in the [bmim][Tf₂N] or ACN/TBAPF₆ indicate not only an influence of the nature of the counter ions on the polymer growth but also its effect as the supporting solvent for the post-polymerization cycling.

Cyclic voltammetry can provide valuable information to analysis the structure of the PEDOT formed. In **Figure 3.2b**, It can be noticed the voltamograms of PEDOT-[bmim][Tf₂N]-ACN/TBAPF₆ displays two anodic peak currents, although only one broad cathodic peak can be observed may because peaks merged into one. The shape and current intensity of the CV is very different comparing to PEDOT-[bmim][Tf₂N]-[bmim][Tf₂N] in **Figure 3.2d**, which used ILs as growth medium and supporting electrolyte. From **Figure 3.2a-d**, it has been noted that the redox peaks of the post-polymerization CVs for PEDOT grown in [bmim][Tf₂N] or ACN/TBAPF₆ varied significantly depending on whether monomers were cycled in molecular solvent system or in ionic liquid, in which the counter ions intercalated into polymer films need a transferring time for equilibration in the new solvent.. This phenomenon is mainly related to the different extent polymer can expand in various supporting electrolyte, which affect the size of response.¹¹⁷. What's more, the two distinct anodic peaks displayed in **Figure 3.2a** indicate that at least two redox reaction mechanisms have been involved in oxidation. During redox reaction of a conducting polymer, there is a principal limiting mechanism of the electronic charge compensation: expulsion of cation/anion originally presented in the polymer film together with incorporation of anion/cation from the surrounding electrolyte during oxidation/reduction process to maintain electroneutrality. In the first step of this experiment which is electropolymerization of EDOT in IL shown in **Figure 3.1a**, the ionic liquid of

[bmim][Tf₂N] as cycling electrolyte can actively involve in the redox response of deposited polymer, resulting in counter-ion intercalation/de-intercalation near the polymer backbones. For the positive doping process, electrons would be exchanged in oxidation process, meanwhile [Tf₂N]⁻ would be intercalated in the polymer film instead of electrons. As shown in **Scheme 3.1**. The viscosity and conductivity of the supporting solution, the nature and mobility of the counter ions, and ability of the supporting solution to swell the polymer film, is able to significantly influence the doping process and deposited polymer's electrochemical behavior in electropolymerization cycling and its afterwards post-polymerization CV process.¹²⁵



Scheme 3.1 Positive Doping/De-doping Process of PEDOT in [bmim][Tf₂N].

However, cases are more complex for the post-polymerization CV in a different medium. It has been observed in **Figure 3.2** that there are multiple redox peaks in the PEDOT polymer films synthesized in ionic liquids. The “two-peaks” phenomenon can only be observed in PEDOT-[bmim][Tf₂N]-ACN/TBAPF₆ and PEDOT-ACN/TBAPF₆-

ACN/TBAPF₆ when organic solvent was used as post-polymerization CV electrolyte. Considering what is the reason for the multiple redox peaks observed for poly(thiophene), there is extensive investigations in the literatures however these discussions have not reached to an agreement yet and still under debate. It has been proposed that in PEDOT polymers the polymer chains can be highly conjugated and well-grown, but also it can be shorter with a more open configuration. As a result, the polymer structure is composed of two zones, one is rigid and the other is loosely packed.^{117, 118, 126, 127-130} The presence of two zones in the polymer structure could explain the presence of two peaks in oxidation and reduction process for PEDOT. Also, these multiple redox peaks could be explained by the transitions between polaron, bipolaron neutral, and metallic states of the polymer,¹³¹ An additional possibility is speculated that the presence of doping and de-doping in polymer's redox processes because of the ionic liquid cation. This can be related to the interchain cavity and the solvation energy of the polymer in different mediums.

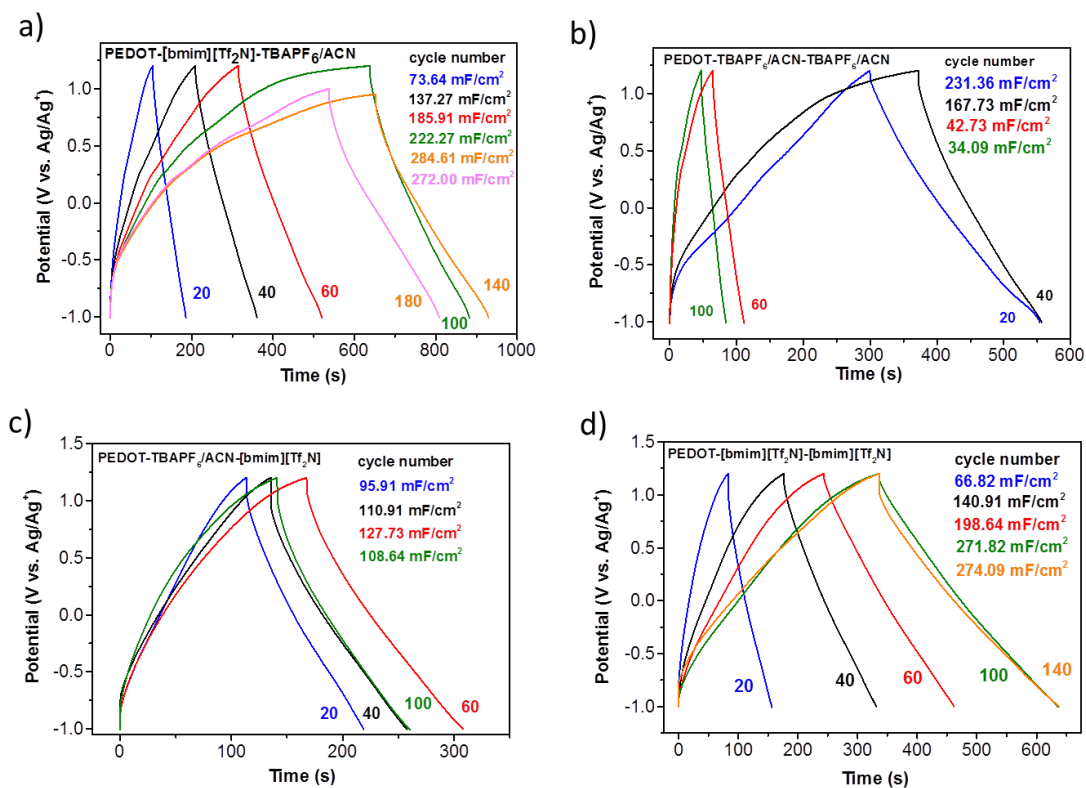


Figure 3.3 Galvanostatic charge-discharge curves collected for the PEDOT electrodeposited in ILs or organic solvents. **(a)** [bmim][Tf₂N] as electrodeposition medium and TBAPF₆/ACN as post-electropolymerization electrolyte; **(b)** TBAPF₆/ACN as both electrodeposition medium and post-electropolymerization electrolyte; **(c)** TBAPF₆/ACN as electrodeposition medium and [bmim][Tf₂N] as post-electropolymerization electrolyte; **(d)** TBAPF₆/ACN as both electrodeposition medium and post-electropolymerization electrolyte, at a current density of 2 mA cm⁻²; the areal capacitance values inferred are indicated on the plot.

PEDOT films electrochemically deposited in ILs have shown an increase of galvanostatic charge-discharge performance as shown in **Figure 3.3** As deposited PEDOT

cycling in TBAPF₆/ACN shows higher capacitance than cycling in ILs, suggests higher extent of polymer swelling and faster ion transfer into and out of the polymer chains.

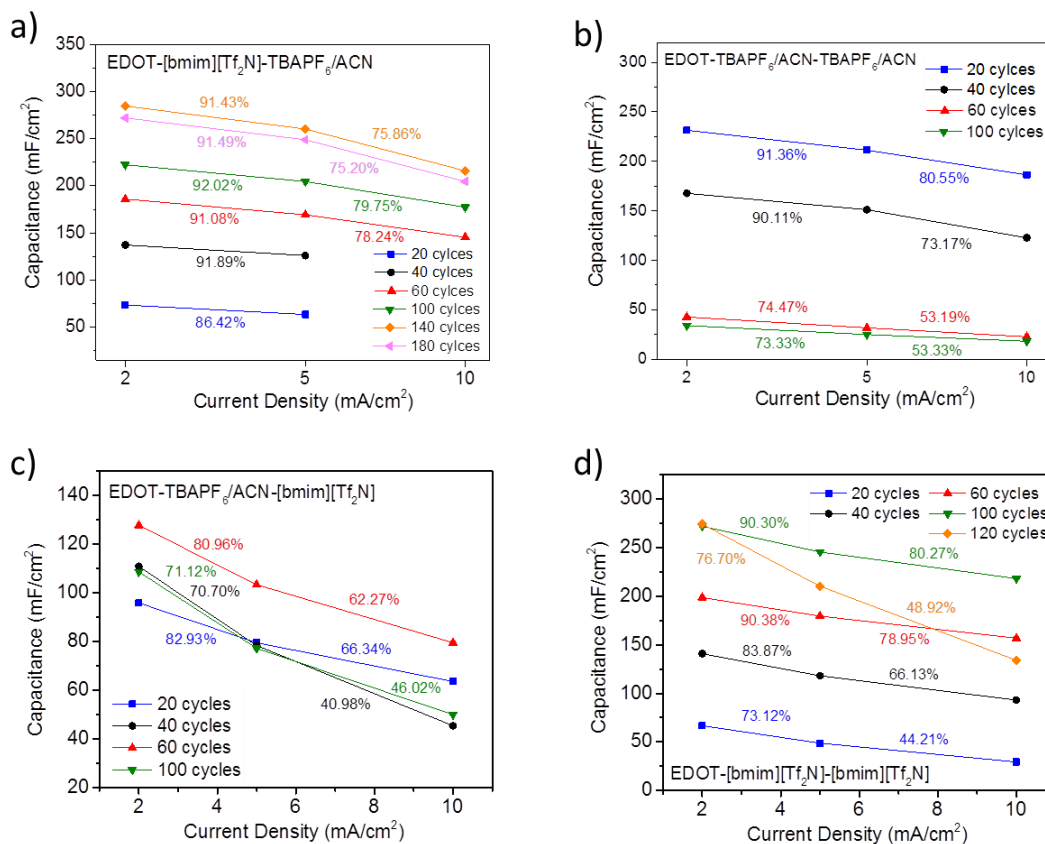


Figure 3.4 Summary of galvanostatic charge-discharge values collected for the PEDOT electrodeposited in ILs or organic solvents. **(a)** [bmim][Tf₂N] as electrodeposition medium and TBAPF₆/ACN as post-electropolymerization electrolyte; **(b)** TBAPF₆/ACN as both electrodeposition medium and post-electropolymerization electrolyte; **(c)** TBAPF₆/ACN as electrodeposition medium and [bmim][Tf₂N] as post-electropolymerization electrolyte; **(d)** TBAPF₆/ACN as both electrodeposition medium and post-electropolymerization electrolyte, at a current density of 2, 5, and 10 mA cm⁻²; the percentage numbers indicated

on the plot are the attenuation degree of capacitance values with the increased current density.

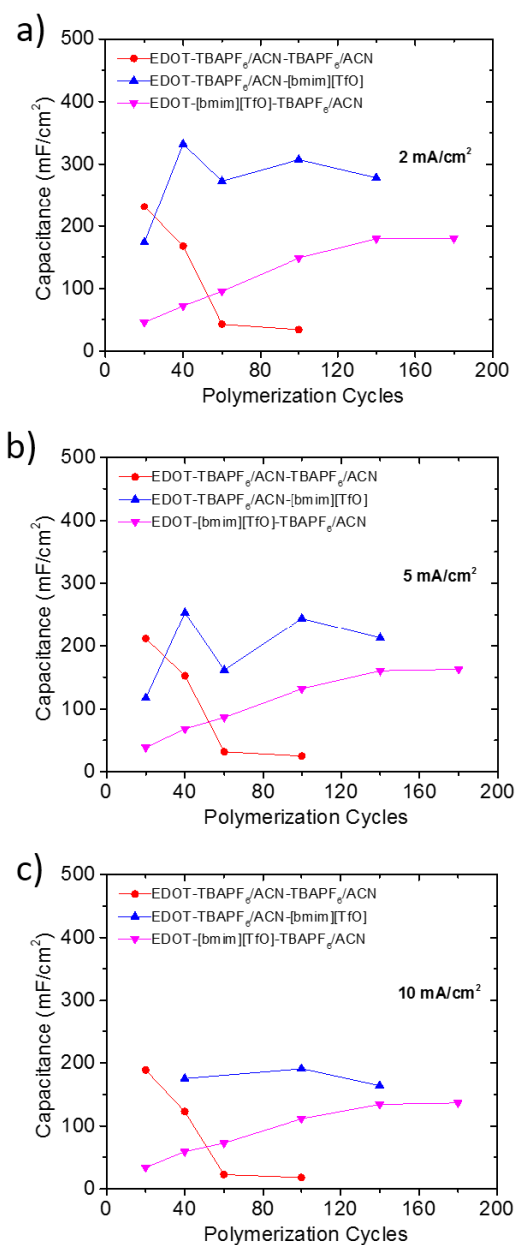


Figure 3.5 Summary of galvanostatic charge-discharge values collected for the PEDOT electrodeposited in [bmim][TfO] or TBAPF₆/ACN, at a current density of (a) 2, (b) 5, and (c) 10 mA cm⁻².

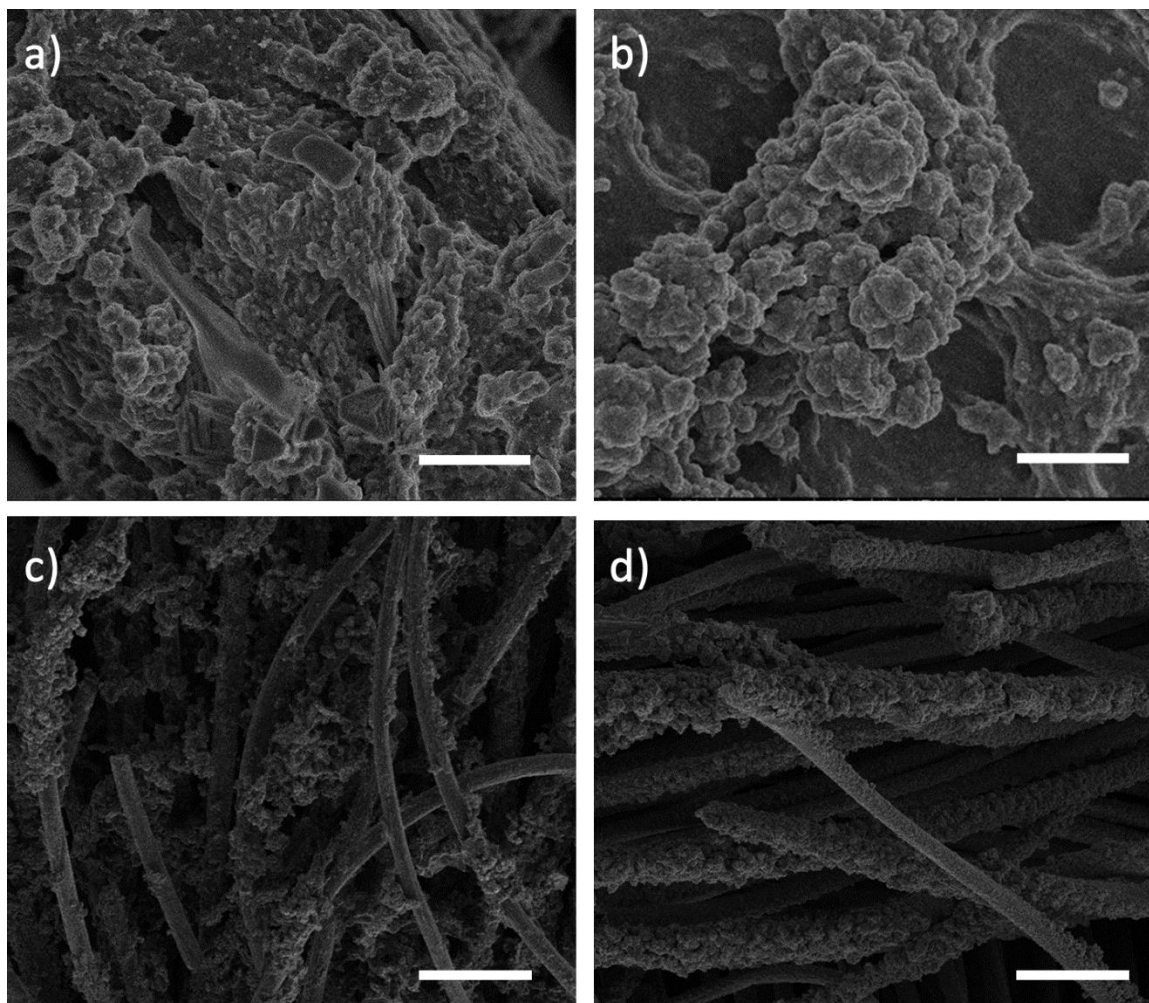


Figure 3.6 SEM images of the morphologies of electrodeposited PEDOT films grown in (a) (c) TBAPF₆/ACN, (b) (d) [bmim][Tf₂N]. Electrodeposition conditions: 25 mM monomer solutions in electrolyte; 100 deposition cycles in a voltage window of -1.0 – +1.2 V (vs. Ag/Ag⁺), on carbon paper electrodes; deposition scan rate of 50 mV s⁻¹. The scale bar in (a) and (b) is 2 μm; (c) and (d) is 50 μm.

Films grown in ILs could give different morphologies.^{119, 121} In addition to the intrinsic pseudocapacitive properties of ECPs, the interfacial electrochemistry between ECPs and the electrolyte also plays a significant role for its overall capacitance performance, which

can be enhanced by morphology adjustments. Synthesis of nano or meso-scale structures with hierarchical porosity can not only provide sufficient specific surface area (SSA) as electroactive sites for faradaic reactions, but also to ensure the effectively participation of electrolyte ions and electrons in the interface.⁴⁴ Therefore, the surface of PEDOT film electrochemically deposited on the carbon paper electrode was examined by scanning electron microscope (SEM), as shown in **Figure 3.6**. There is a distinct effect of the anion (and a less clear effect of the solvent) on the morphology of the PEDOT layers. The film produced in the neat ILs was more compact and homogeneous than that from the organic solution medium with higher electrochemically activity and heavier doped. The films electropolymerized in the TBAPF₆/ACN solutions shows a granular depositions whereas the film grown in ILs appeared to be very smooth and in order.

3.2.2.1 Electrochemical Characterizations of BEDOT

In order to clarify and confirm the effect of anions on PEDOT and its derivatives, 4,4'-dimethoxy-3,3'-bithiophene (BEDOT) were synthesized, and the same protocol has been carried out. **Figure 3.7** shows the linear scans in potential and actual onsets of oxidation for BEDOT, where the various oxidation features on scanning linearly in the -2.0 – +2.5 V potential window (vs. Ag/Ag⁺) are detailed directly on the plots. PBEDOT dark films can be deposited on the glassy carbon button electrode in [bmim][Tf₂N] and [bmim][TfO], indicating that electropolymerization is occurring during linear scans.)

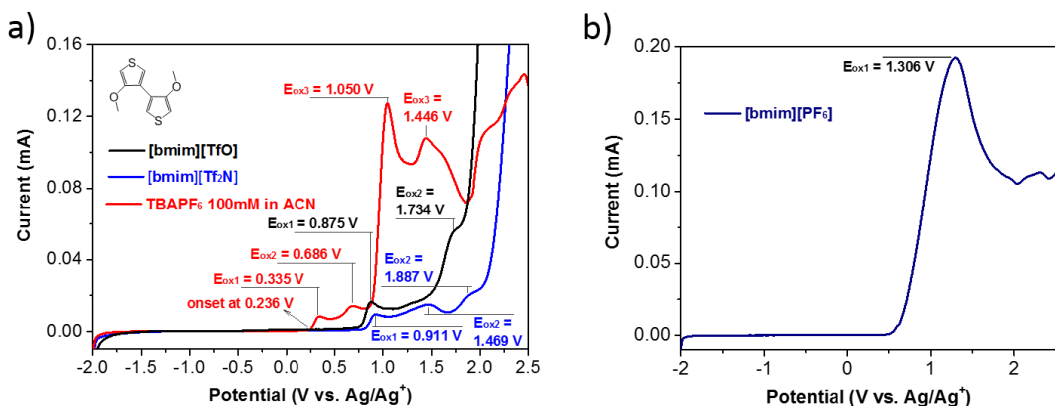


Figure 3.7 Linear scan voltammograms collected on glassy button electrodes at a scan rate of 20 mV s^{-1} from a solution of **BEDOT** (5 mM) detailing oxidation features, in (a) [bmim][Tf₂N], [bmim][TfO], TBAPF₆/ACN and (b) [bmim][PF₆].

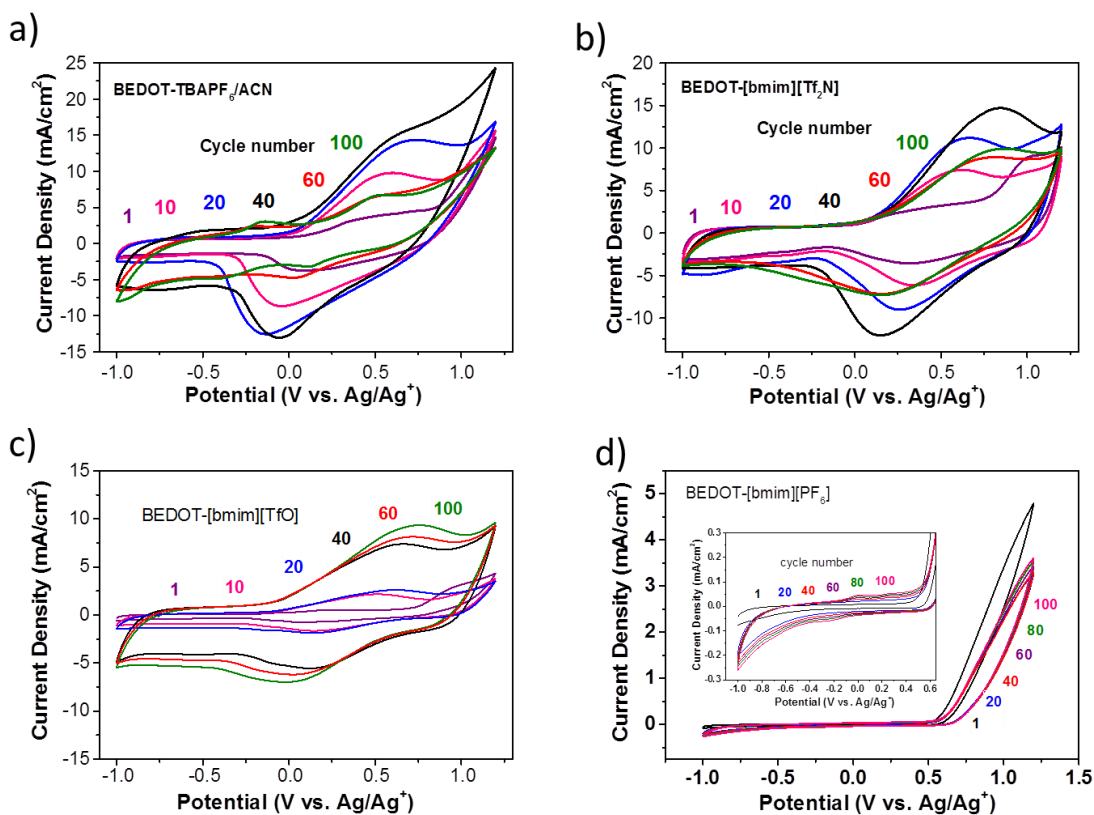


Figure 3.8 Cyclic voltammograms during electropolymerization of BEDOT with increased cycles prepared from (a) TBAPF₆/ACN, (b) [bmim][Tf₂N], (c) [bmim][TfO],

and **(d)** [bmim][PF₆] Electrodeposition conditions: 25 mM monomer solutions in supporting medium; 20-100 deposition cycles in a voltage window of -1.0 – +1.2 V (vs. Ag/Ag⁺), on carbon paper electrodes; deposition scan rate of 50 mV s⁻¹. Each voltammogram is normalized to the extent of functionalized surface area.

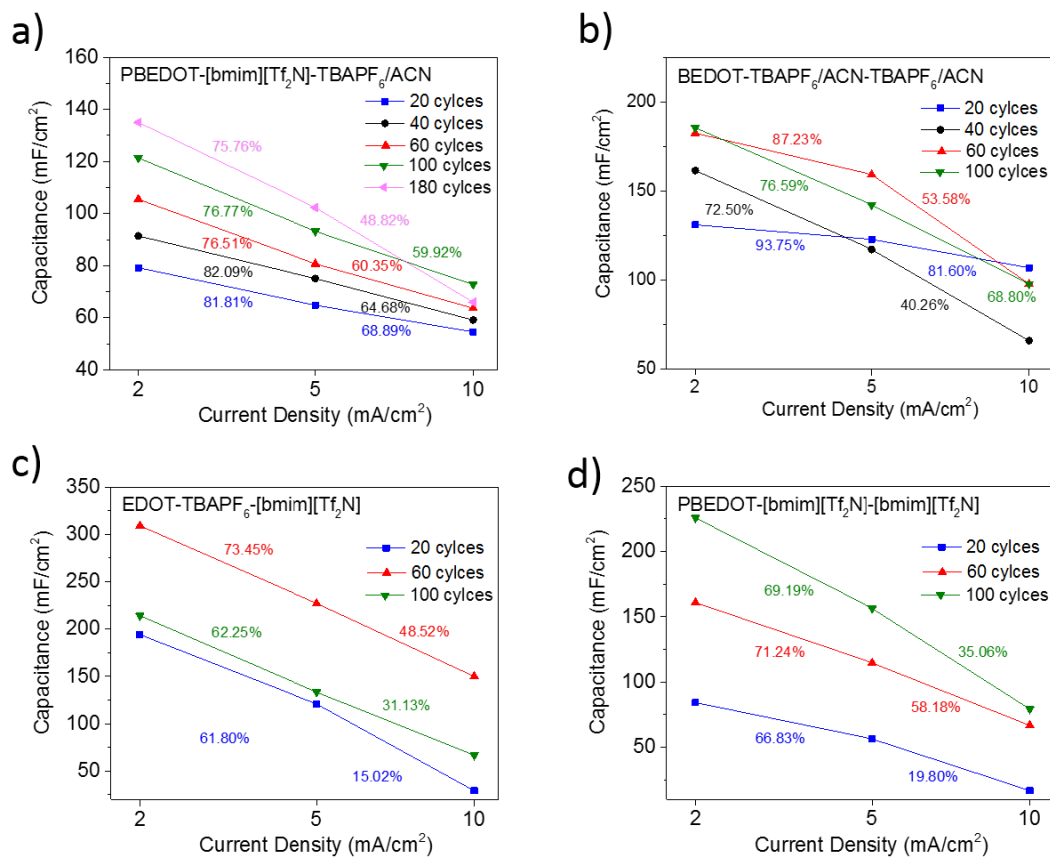


Figure 3.9 Summary of galvanostatic charge-discharge values collected for the PBEDOT electrodeposited in ILs or organic solvents. **(a)** [bmim][Tf₂N] as electrodeposition medium and TBAPF₆/ACN as post-electropolymerization electrolyte; **(b)** TBAPF₆/ACN as both electrodeposition medium and post-electropolymerization electrolyte; **(c)** TBAPF₆/ACN as electrodeposition medium and [bmim][Tf₂N] as post-electropolymerization electrolyte; **(d)** TBAPF₆/ACN as both electrodeposition medium

and post-electropolymerization electrolyte, at a current density of 2, 5, and 10 mA cm⁻²; the percentage numbers indicated on the plot are the attenuation degree of capacitance values with the increased current density.

3.2.3 Conclusion

Electropolymerization of EDOT and its derivative 4,4'-dimethoxy-3,3'-bithiophene (BEDOT) have been studied in three kinds of imidazolium-based ionic liquids and conducting salt in volatile organic compounds with different anions both as the growth medium and the supporting electrolyte, to assess the influence of these anions on their morphology and electrochemical activity. It is found these thiophene polymers grown in ILs with higher viscosity and lower diffusion shows much slower growth rate and orderly morphologies than in TBAPF₆ dissolved in ACN, and gives better electrochemical performance via cyclic voltammetry (CV) and galvanostatic charge-and-discharge (CD) studies. Polymers displayed multiple redox peaks in several cases, the possible reasons and origins are discussed. The synthesized polymer can be affected greatly by both the ILs with different anion/cation, and its mutual interaction with targeted monomer. As far as known, there is no systematic study on how the anions of ILs and common organic solution could play a role as a medium both for polymerization and post-polymerization electrolyte for PEDOT and its derivatives. This study can be used as an easy reference and provide experimental diagnostic data when selecting ionic liquids to investigate and optimize thiophene-based electrochemical systems, such as batteries and supercapacitors.

Chapter 4

Direct Functionalization of Nanodiamonds with Maleimide

4.1 Introduction

Diamond materials span a wide range of attractive physical properties, including large mechanical resistance, high thermal conductivity, and tunable optoelectronic behaviour when suitably doped.^{132, 133} Down to the nanoscale, embedded diamond nanoparticles find use in surface coatings, nanocomposites, and are promising building elements in nanophotonic device engineering.¹³⁴ In parallel, their excellent chemical stability and anticipated compatibility in biological systems make them particularly attractive for biomedical applications.¹³³ Thus, a number of recent studies have emphasized the perspectives of nanodiamonds as drug-delivery vehicles, templates for biological sensing, and probes in bioimaging.¹³² The nature of the solubilizing substituents and specific functional groups appended to the nanodiamond surface defines the function of the nanoparticle, and in turn its field of applicability.

Synthetic nanodiamonds prepared by detonation protocols, so-called detonation diamond nanoparticles (DDNPs), are composed of primary nanocrystals (2-10 nm) and their aggregates (10-100 nm).¹³² As synthesized, DDNPs show a relatively heterogeneous surface, composed of amorphous carbon forms (*a*-C), hydroxyls (–OH), alkoxy/ether

groups (C–O–C), carbonyls (C=O), sp^2 moieties (C=C), and a non-negligible content of dangling bonds ($-C^*$, unsatisfied valence).¹³⁵⁻¹⁴⁰ Thus, DDNPs are generally subjected to a chemical surface-treatment in order to selectively produce short functionalities (*e.g.*, $-OH$, $-CO_2H$, $-COCl$, $-NH_2$) to which larger substituents can be appended, most commonly by esterification or amidation.¹⁴¹ The reductive C-C coupling between aryl diazonium salts and hydrogenated diamond films,¹⁴² and *graphitized*/ hydrogenated DDNPs,¹⁴³⁻¹⁴⁵ are examples of direct functionalization. Further derivatization with functional substituents can be achieved by catalyzed cross-coupling at the aryl site. As an alternative, functional aryls can also be appended to diamond films (*e.g.* via cycloadditions, [4+2] or [2+2]),¹⁴⁶⁻¹⁵² and to the π -system of thermally annealed nanodiamonds,^{153, 154} albeit using specific reagents and elevated temperature conditions.¹⁵⁵ Here, we report on a protocol of direct functionalization by which maleimide-derivatized substituents can be appended to the outer shell of thermally annealed nanodiamonds under ambient conditions. Noting that a wide range of functional maleimides can readily be made from the commercial precursor maleic anhydride,¹⁵⁶ this direct approach to functionalizing nanodiamonds should be amenable to the preparation of nanomaterials with a manifold of functions.

4.2 Experimental Section

4.2.1 Preparation of the Nanoparticle Precursors

Materials: Synthetic nanodiamonds with nominal primary particle sizes of less than 10 nm were sourced from Sigma Aldrich (catalogue # 636428-5G). MilliQ water (18 M Ω)

was used as the dispersive medium in the ball-milling step. All other reagents were ACS reagent grade and sourced from Sigma Aldrich.

Methods: *Ball-milling procedure* – Concentrated solutions of diamond nanoparticles were prepared according to the salt-milling protocol described by Pentecost *et al.*¹⁵⁷ The nanodiamonds were mixed with NaCl in a 1:7 ratio and then transferred into a steel jar (50 mL volume; Retsch Co.), along with stainless steel grinding balls (50 g, 6 mm diameter). The milling was carried out at 400 rpm for 15h (by 1h intervals, and 30min pauses between milling intervals) in a Planetary Ball Mill PM 200 (Retsch Co.). Next, the mixture was charged in a glass beaker filled with hydrochloric acid (HCl) (37% in volume), diluted with deionized water, and sonicated in a sonication bath (Branson 5510, Branson) for 30 min in order to remove iron contaminants produced during the milling step (from the steel balls and jar). The resulting solution of nanoparticles was then centrifuged in an ultracentrifugation system (Superspin 610 rotor, WX Ultra 90, Thermo Scientific) to precipitate the nanodiamonds. The nanoparticles were collected, re-dispersed in deionized water and centrifuged again. This cleaning step was repeated several times until a negative silver nitrate test (0.1N) was obtained. The ball-milled and purified nanodiamonds were dispersed in aqueous HCl solutions (pH~3.8) and sonicated with an ultrasonic probe for 1.5h^[2] (Ultrasonic Processor Q500, Qsonica; ϕ 1.27 cm Standard probe; Maximum out-put power 400W, used at 60% amplitude). *Thermal annealing protocol* – The ball-milled nanodiamonds (DDNPs) were charged in a quartz vessel, placed in a furnace (V.S. Technologies), and subjected to distinct annealing temperatures for 1h under vacuum (10^{-2} Torr): T=500°C → GDNP(500), T=600°C → GDNP(600), T=700°C → GDNP(700), T=800°C → GDNP(800), T=900°C → GDNP(900).

4.2.2 Characterization of the Nanoparticle Precursors

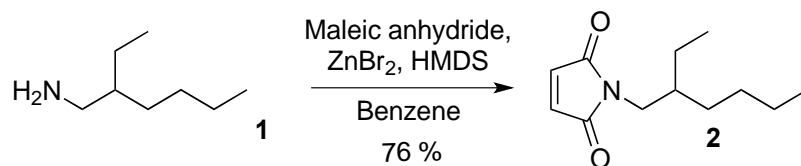
The size distribution of the ball-milled nanodiamond precursors was estimated by dynamic light scattering (DLS) (Zetasizer Nano ZS, Malvern). As DLS measurements were found to be sensitive to the concentration of nanoparticles in solutions,¹⁵⁸ the concentration of each sample solution was adjusted by tuning the absorbance of the sample to optical density (OD)~1.0 at the wavelength of 350 nm (Ocean Optics Inc., light source DH-2000-Bal, 1 cm path-length cuvette) through dilution with an aqueous HCl solution (pH~3.8) before each DLS measurement. A Lemis ViscoDens VDM-300 was used to measure the solvent viscosity and density of pH~3.8 HCl solutions, and the measured parameters were input in the DLS method. Over 90 DLS measurements (20 seconds per run) were averaged to avoid environmental perturbation and obtain stable data. The size and shape of the primary nanoparticles was further examined by high-resolution transmission electron microscopy (HR-TEM; Titan G2 80-200, FEI Co.). Aqueous solutions of nanodiamonds were deposited on 300 mesh Au grids (Ted Pella Inc., USA) and the nanodiamonds were analyzed under an acceleration voltage of 300 kV. Fourier transform infrared spectroscopy (FTIR) analyses were carried out on a Nicolet iS10 from Thermo Scientific equipped with a Smart iTR compartment for ATR analysis. The spectra were collected at 4 cm⁻¹ resolution with 64 cumulative scans in the 4000-600 cm⁻¹ spectral range. Raman analyses were carried out on a LabRAM Aramis (Horiba Jobin Yvon) micro-Raman system. The spectra were acquired in a backscattering configuration. A 40X objective was used to focus and collect scattered light from the substrate, and the excitation source consisted of a He-Cd laser (325 nm). Typical laser power at the sample position was 1D (~1 Mw) and the data acquisition time was 20 s per scan. Note: Significant degradation of the sample was observed with

increasing power and number of scans by Raman under the UV laser beam (i.e., upon longer times of exposure) – the peak maximum shifting towards higher frequencies (from ca. 1580 cm^{-1} , G-band \rightarrow to 1640 cm^{-1} , –OH). Oxidative degradation mechanisms may be the source of degradation. X-ray diffraction analyses (XRD) were performed on a BRUKER D8 Advance ($\text{Cu}\lambda\text{K}\alpha_1 = 1.5406\text{ \AA}$; increments: 0.01 degree/step; scan speed: 1 s/step). X-ray photoelectron spectroscopy (XPS) studies were performed on a Kratos Axis Ultra DLD spectrometer equipped with a monochromatic Al $\text{K}\alpha$ X-ray source ($h\nu = 1486.6\text{ eV}$) operating at 150 W, a multichannel plate and delay line detector under a vacuum of 1×10^{-9} mbar. The measurements were performed in hybrid mode using electrostatic and magnetic lenses. All spectra were recorded using an aperture slot of $300\text{ }\mu\text{m} \times 700\text{ }\mu\text{m}$. The survey and high-resolution spectra were collected at fixed analyzer pass energies of 160 eV and 20 eV, respectively and quantified using empirically derived relative sensitivity factors provided by Kratos analytical. The data were analyzed with the software CASAXPS. The individual peaks were fitted by a Gaussian (70%)–Lorentzian (30%) (GL30) function after applying Shirley-type background subtraction. Thermogravimetric analyses (TGA) were conducted in Al_2O_3 crucibles under argon flow (Netzsch, TG 209 F1 with ASC). A heating rate of $5\text{ }^\circ\text{C}/\text{min}$ and sample mass of ca. 12mg were set for all experiments.

4.2.3 Synthesis of the Maleimide EHM

Materials and Methods: All reagents from commercial sources were used without further purification. Reactions were carried out under a nitrogen atmosphere. Solvents were dried and purified using standard techniques. Flash chromatography was performed with analytical-grade solvents using Silicycle SiliaFlash P60 (particle size $40\text{--}63\text{ }\mu\text{m}$, 60 \AA , 230

– 400 mesh) silica gel. Flexible plates PE SilG/UV 250 μm from Whatman[®] were used for TLC. Compounds were detected by UV irradiation or staining with I_2 , unless otherwise stated. All compounds were characterized by ^1H NMR and ^{13}C NMR at room temperature on a Bruker Avance III Ultrashielded 600 Plus instrument (respectively at 600 MHz and 150 MHz) or on a Bruker Avance III 500 equipped with a 13C-1H *cryoprob* (at 500 MHz for proton and 125 MHz for carbon). High-resolution mass spectrometry (HRMS) accurate data were recorded using a Bruker LC-MS MicroTOF II in positive electro spray ionization mode (+ESI). Elemental analyses were carried out on a Flash 2000 - Thermo Scientific CHNO Analyzer.



Synthesis of 1-(2-ethylhexyl)-1*H*-pyrrole-2,5-dione¹⁵⁹ (2) – EHM: A solution of 2-ethylhexan-1-amine 1 (1.5 mL, 9.2 mmol) in dry benzene (5 mL) was added to a stirred solution of maleic anhydride (1 g, 10.12 mmol) in dry benzene (100 mL) at room temperature over a *ca.* 15 min period. After an additional 1 h stirring at 30°C, ZnBr_2 (2.28 g, 9.7 mmol) was added in one portion, and the mixture was stirred for another *ca.* 10 min. A solution of hexamethyldisilazane (HMDS) (2.75 mL, 13.415 mmol) in dry benzene (15 mL) was added slowly at 30°C over a period of 30 min (the reaction mixture changed from clear to turbid). Next, the reaction temperature was increased to 80°C, and the mixture was refluxed for an additional 2 h. After being cooled to room temperature, the reaction mixture was poured into 0.5 M HCl (70 mL). The aqueous phase was extracted with ethyl acetate (2x50 mL). The combined organic extracts were washed successively with 40 mL of

saturated NaHCO_3 and 40 mL of brine and then dried over anhydrous MgSO_4 and concentrated under vacuo. The oily residue was purified by column chromatography (hexane/EtOAc 5:1) to yield compound 2 (1.6 g, 76%) as a clear oil. ^1H NMR (500 MHz, CDCl_3), δ (ppm): 6.68 (s, 2H); 3.40 (d, 2H, $J = 7.5$ Hz); 1.72-1.69 (m, 1H); 1.27-1.21 (m, 8H); 0.87 (t, 6H, $J = 7.5$ Hz). ^{13}C NMR (125 MHz, CDCl_3), δ (ppm): 170.8; 133.6; 41.3; 37.7; 29.9; 28.0; 23.3; 22.6; 13.6; 9.9. HRMS/ESI: m/z calcd for $\text{C}_{12}\text{H}_{20}\text{NO}_2^+$: 210.1489 [M+H] $^+$, found: 210.1483.

4.2.4 Functionalization Procedure

Methods: Following the annealing step, 50 mg of GDNPs were dispersed and sonicated for 60 min (sonication bath, Branson 5510) in 5 mL of acetonitrile (ACN), under ambient conditions. Next, the functional imide (EHM or M, 1 g) was added to the colloidal solution of diamond nanoparticles, and the mixture was stirred briefly. Assuming functionalization had occurred, the mixture of GDNPs and (excess) imide substituents was subjected to 5 washing cycles by centrifugation (Eppendorf 5702, 4400 rpm) in acetone (15 mL/washing-cycle) in order to remove the free imide substituents (excess). Next, the nanoparticles were dried under vacuum overnight (10^{-2} mBar, 25°C). Note: Unfunctionalized EHM or M substituents can be recovered upon centrifugation in acetone. The DLS, FTIR, XPS and TGA measurements were performed as per the experimental described for the nanodiamond precursors.

4.2.5 SS-NMR Analyses

1D ^1H MAS and ^{13}C CP/MAS spectra were recorded on a Bruker AVANCE III spectrometer operating at resonance frequencies of 400 and 100 MHz for ^1H and ^{13}C , respectively, and using a conventional double resonance 4 mm CPMAS probe. The samples were introduced under argon into zirconia rotors, which were then tightly closed. The spinning frequency was set to 17 and 10 KHz for the ^1H and ^{13}C analyses, respectively. NMR chemical shifts are reported with respect to TMS as the external reference. For CP/MAS ^{13}C NMR experiments, the following sequence was used: i) 90° pulse on the proton (pulse length 2.4 s), then ii) cross-polarization step with a contact time of typically 2 ms, and iii) acquisition of the ^{13}C signal under high-power proton decoupling. The delay scans was set to 5 s to allow the complete relaxation of the ^1H nuclei, and 3,000-5,000 scans were performed for a carbon experiment and 32 for a proton experiment. An apodization function (exponential) corresponding to a line broadening of 80 Hz was applied prior to Fourier transformation.

2D $^{13}\text{C}\{^1\text{H}\}$ heteronuclear correlation (HETCOR) analyses were conducted on a Bruker AVANCE III spectrometer using a 3.2 mm MAS probe. The following protocol was employed: i) 90° proton pulse, ii) t_1 evolution period, iii) cross-polarization (CP) to carbon spins, and iv) detection of carbon magnetization under two pulse phase modulation (TPPM) decoupling.^{160, 161} For the cross-polarization step, a ramped radio frequency (RF) field centered at 75 KHz was applied to protons, while the carbon RF field was matched to obtain optimal signal. A total of 32 t_1 increments with 2000 scans each were collected. The sample spinning frequency was 8.5 kHz. A 2D Fourier transformation gives through space

between pairs of neighboring carbon (in F2) and proton (in F1) nuclei. Using a short contact time (0.2 ms) for the CP step, the polarization transfer in the dipolar correlation experiment is expected to be quite selective, that is to lead to correlation only between pairs of connected ^1H - ^{13}C spins (C-H directly bonded).

^1H - ^1H double-quantum (DQ) experiments were recorded on a Bruker AVANCE III-600 spectrometer with a conventional double resonance 3.2 mm CPMAS probe, according to the following general protocol:¹⁶² i) excitation of DQ coherences, ii) t_1 evolution, iii) Z-filter, and iv) detection. The spectra were recorded in a rotor-synchronized fashion in t_1 ; that is the t_1 increment was set equal to one rotor period (4.545 μs). One cycle of the standard back-to-back (BABA) recoupling sequence was used for the excitation and reconversion period. Quadrature detection in w_1 was achieved using the States-TPPI method. A spinning frequency of 22 KHz was used. The 90° proton pulse length was 2.5 μs , while a recycle delay of 5 s was used. A total of 128 t_1 increments with 32 scans each were recorded. DQ proton spectroscopies under fast MAS have recently been shown to be a powerful technique to probe the structural information and dynamics inherent to proton-proton dipolar couplings. The DQ frequency in the w_1 dimension corresponds to the sum of two single-quantum (SQ) frequencies of the two coupled protons and correlates in the w_2 dimension with the two corresponding proton resonances.

4.2.6 Preparation and Characterization of F5M-GDNPs

Materials: Fluorescein-5-maleimide (F5M) was purchased from Life Technology (CAS: 75350-46-8).

Methods: 10 mg of GDNPs(800) were dispersed and sonicated for 60 min (sonication bath, Branson 5510) in 1 mL of acetonitrile (ACN), under ambient conditions. Next, Fluorescein-5-maleimide (F5M, 5 mg) was added to the colloidal solution of diamond nanoparticles, and the mixture was stirred briefly. The mixture of GDNPs and (excess) F5M dye molecules was subjected to washing cycles by centrifugation (Eppendorf 5702, 4400 rpm) in acetonitrile until the supernatant solution showed no residual optical absorption by UV-Vis. Next, the nanoparticles were dried under vacuum overnight (10^{-2} mBar, 25°C) or dissolved in a mixture of acetonitrile/DMF for further characterizations.

Characterization of the DDNPs Functionalized with F5M: Fluorescence microscopy images were collected with an Olympus BX43 Upright Fluorescence Microscope (Software: QCapture). Samples of F5M, GDNPs(800) and F5M-GDNPs were spun-cast from acetonitrile on glass substrates. UV-Vis spectra were collected with a Cary 100 (DMF solutions). Fluorescence spectra (from DMF solutions) were acquired with a Cary Eclipse ($\lambda_{\text{Ex}} = 455$ nm; $\lambda_{\text{max}} = 550$ nm). FTIR analyses were carried out on a Nicolet iS10 from Thermo Scientific equipped with a Smart iTR compartment for ATR analysis. The spectra were collected at 4 cm $^{-1}$ resolution with 64 cumulative scans in the 4000-600 cm $^{-1}$ spectral range.

4.3 Results and Discussion on Direct Functionalization of Nanodiamond with Maleimide

4.3.1 Thermal Annealing and Characterization of detonation diamond nanoparticles (DDNPs)

Considering DDNPs, the extent of sp^2 moieties at the nanodiamond surface can be increased by high-temperature annealing treatment under vacuum, a procedure by which the sp^2 carbon content (*graphite-like*) develops from shell to core, at the expense of the sp^3 diamond carbon.¹⁶³⁻¹⁶⁵ The *graphite-like* surface of fullerenes, such as carbon nanotubes (CNTs) and buckminsterfullerene (C60), is known to be amenable to addition reactions with various molecular partners, including substituted furfuryl and maleimide derivatives.¹⁶⁶ Here, DDNPs were de-aggregated by ball-milling (see **Figure 4.1**) and subjected to distinct annealing temperatures under vacuum (10^{-2} Torr), yielding various samples of *graphitized* diamond nanoparticles (GDNPs); the evolution of the surface composition was monitored by FTIR and Raman spectroscopy. As shown in **Figure 4.2**, thermal annealing induces i) a reduction of the extent of surface carbonyls (1715 cm^{-1} ; **Figure 4.2a**), along with ii) a concomitant development and broadening of the main band ($1500\text{-}1650\text{ cm}^{-1}$; **Figure 4.2b**) as the peak maximum shifts towards lower frequencies (from *ca.* 1640 cm^{-1} ($-\text{OH}$) to 1590 cm^{-1} (G-band contribution)) – features characteristic of the formation of sp^2 bonding patterns.¹⁶⁷

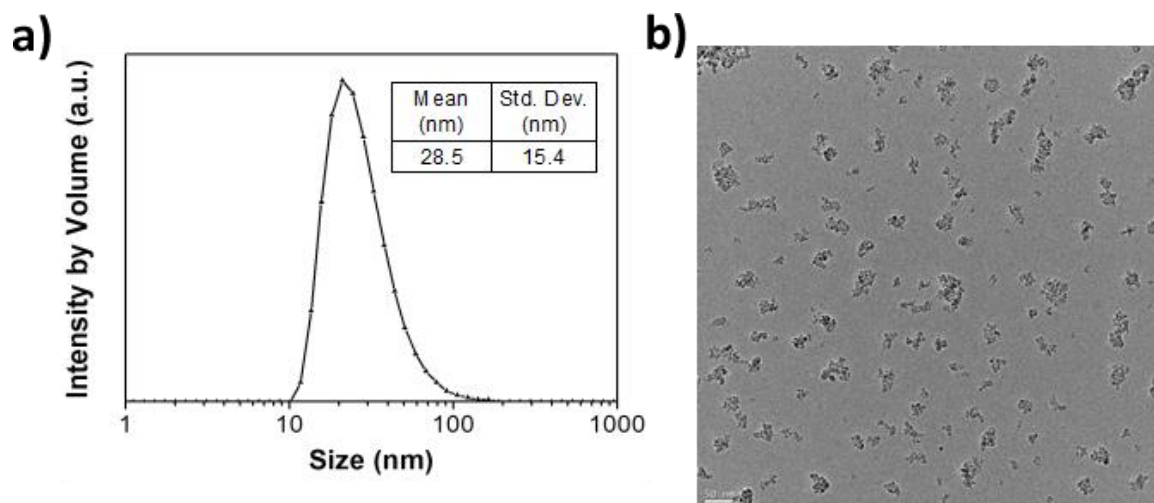


Figure 4.1 a) Size distribution pattern of the ball-milled DDNPs measured by DLS in MilliQ water (tuned to pH~3.8 by HCl solution). b) TEM image (bright field, 150keV) of the corresponding DDNPs (scale bar: 50 nm). Figure adapted with permission.¹⁵⁸

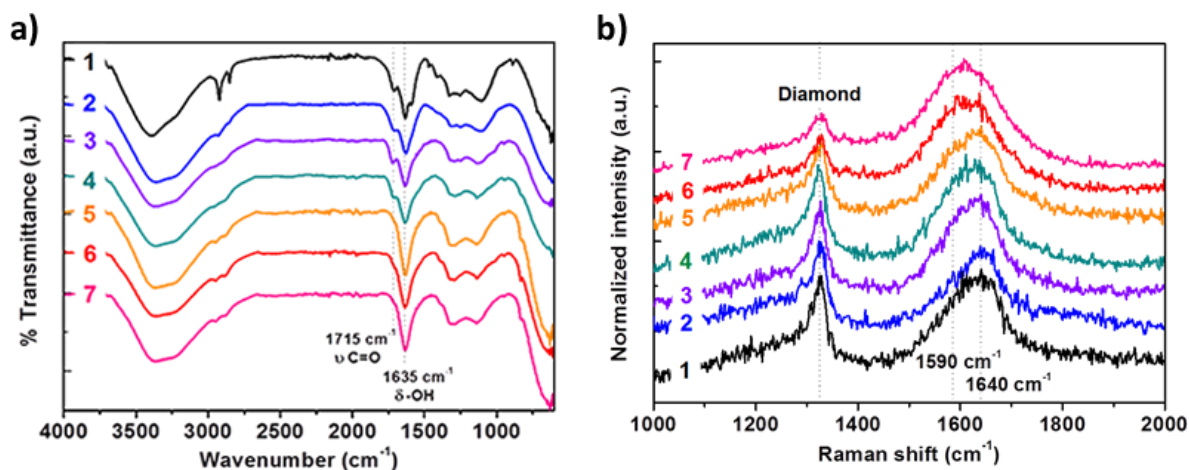


Figure 4.2 a) FTIR spectra and b) Raman spectra (1 scan, $t = 20$ s/scan, $\lambda = 325$ nm) of thermally annealed DDNPs. [1] DDNPs prior to ball-milling (black curve), [2] ball-milled DDNPs (blue curve), [3] DDNPs thermally annealed at 500°C for 1h (purple curve), [4] DDNPs thermally annealed at 600°C for 1h (green curve), [5] DDNPs thermally annealed at 700°C for 1h (orange curve), [6] DDNPs thermally annealed at 800°C for 1h (red curve), and [7] DDNPs thermally annealed at 900°C for 1h (pink curve). Spectra given on an

arbitrary scale. Note: Significant degradation of the sample was observed with increasing power and number of scans by Raman under the UV laser beam (i.e., upon longer times of exposure) – the peak maximum shifting towards higher frequencies (from ca. 1590 cm^{-1} , G-band contribution from the *graphite-like* outer-shell \rightarrow to 1640 cm^{-1} , –OH). Oxidative degradation mechanisms may be the source of degradation.

4.3.2 Functionalization of Annealed DDNPs with Maleimide

In a control experiment, a batch of DDNPs annealed at higher temperature (800°C) – GDNP(800) – was treated with a simple alkyl-substituted maleimide derivative (EHM; **Figure 4.3**) for a few minutes under ambient conditions. A detailed experimental can be found in **Section 4.2.4**; the XRD analysis of the GDNP(800) precursor (**Figure 4.4**) confirmed the integrity of the diamond core upon thermal annealing. With the observation of a net change in nanoparticle dispersion in solution (see **Figure 4.5**), the treated GDNPs were further inspected by FTIR. **Figure 4.3** shows a number of characteristic features pointing to an effective association between EHM and the nanodiamond surface. The FTIR spectra of the ball-milled DDNPs [1] and thermally annealed GDNPs(800) [2], prior to EHM-treatment, are shown along with those of the EHM-treated GDNPs(800) [3] and the free EHM substituent [4]. At a first level of observation, the association between EHM and the nanodiamond surface is supported by the presence of the characteristic stretching modes of maleimide¹⁶⁸ in EHM-treated GDNPs [3]: $\nu(\text{C}=\text{O})$: ca. 1700 cm^{-1} , $\nu_{\text{s}}(\text{C},\text{C}>\text{N}-)$: ca. 1405 cm^{-1} , and $\nu_{\text{as}}(\text{C},\text{C}>\text{N}-)$: ca. 1165 cm^{-1} (Imide I, II and III). Further, a notable shift of the $\nu_{\text{as}}(\text{C},\text{C}>\text{N})$ asymmetric stretch from ca. 1165 cm^{-1} [4] to ca. 1180 cm^{-1} [3] suggests a structural change at the alkene site (C=C) of maleimide. Assuming that an addition

reaction occurred across the alkene, maleimide would be converted to its saturated analog, succinimide – an assumption supported by the apparent loss of the bending modes characteristic of maleimide at 693 cm^{-1} (ring-bend) and 827 cm^{-1} (δ (=CH), out-of-plane) in EHM-treated GDNPs [3] (marked with red box).¹⁶⁹ X-ray photoelectron spectroscopy (XPS) analyses (see **Figure 4.6** and **Table 4.1**) indicate a non-negligible increase in relative oxygen (O: 3.7 at%) and nitrogen (N: 2.3 at%) contents in EHM-treated GDNPs(800) compared to the untreated GDNP(800) precursor (O: 3.0 at%; N: 1.5 at%), thus providing additional support for the change in surface composition inferred from the FTIR data. The thermogravimetric analyses (TGA) of EHM-treated GDNPs(800), the untreated GDNP(800) precursor and the free EHM substituent are provided in the **Figure 4.7**.

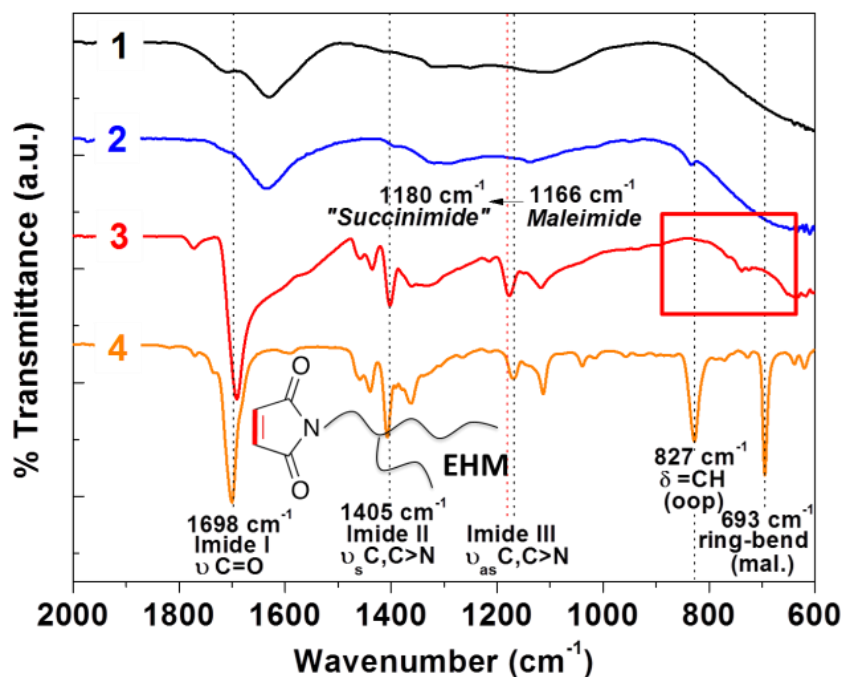


Figure 4.3 FTIR spectra of [1] ball-milled DDNPs (control), [2] thermally annealed GDNPs(800), [3] GDNPs(800) treated with the functional maleimide EHM (EHM-

GDNP), and [4] the free EHM substituent. The molecular structure and main characteristic vibrations of EHM are indicated on the plot.

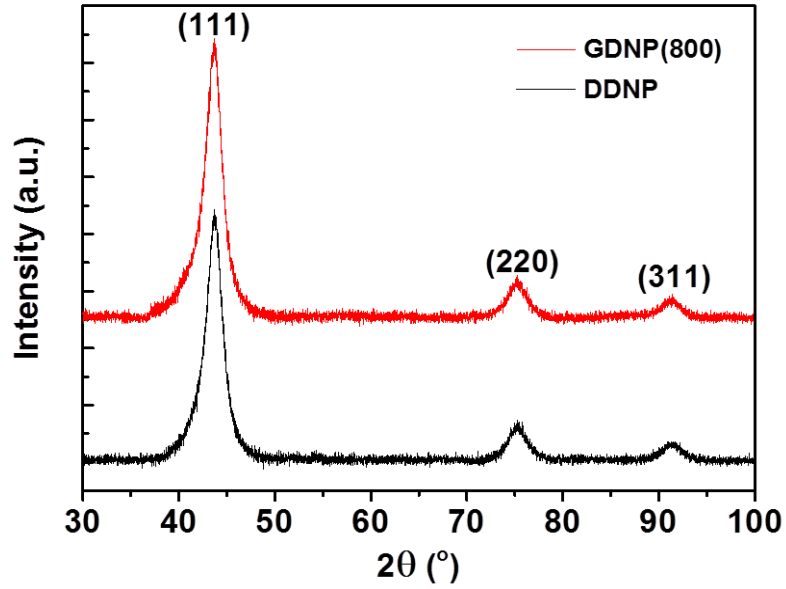


Figure 4.4 XRD patterns of the DDNP and GDNP(800) precursors. (arbitrary scale) The characteristic peaks of the crystal planes of diamond at $2\theta = 44.3^\circ$ (111), 75.5° (220), and 91.7° (311) indicate that the diamond-like carbon structure (sp^3) of the DDNPs is preserved upon annealing at 800°C for 1h.



Figure 4.5 Dilute solutions of DDNPs (left), GDNPs(800) (center) and EHM-treated GDNPs(800) (right) in chlorobenzene (same initial concentration). After 3 days, the colloidal solution of EHM-GDNPs remains stable, while the unfunctionalized DDNP and GDNP precursors precipitated and settled at the bottom of the quartz cuvettes (white circled).

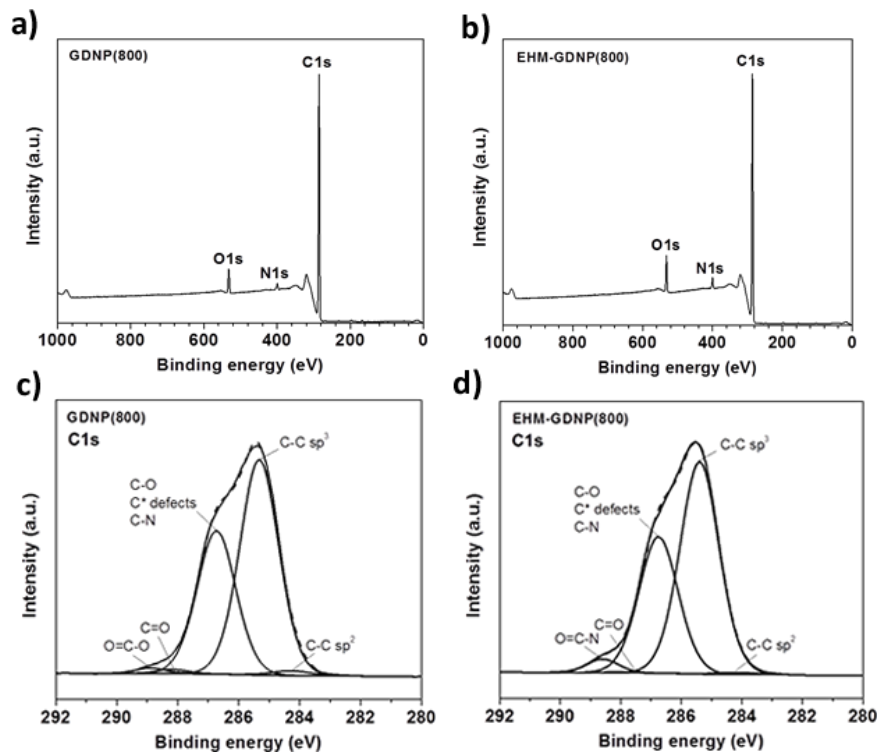


Figure 4.6 XPS survey spectra of **a)** GDNP(800) and **b)** EHM-GDNP(800). High-resolution XPS analyses and deconvolutions of the C1s peaks of **c)** GDNP(800) and **d)** EHM-GDNP(800).

Table 4.1 XPS analyses of the GDNPs(800) and of the EHM-treated GDNPs(800).

	Atomic content (at%)		
	C	O	N
GDNP(800)	95.5	3.0	1.5
EHM-GDNP(800)	94.0	3.7	2.3

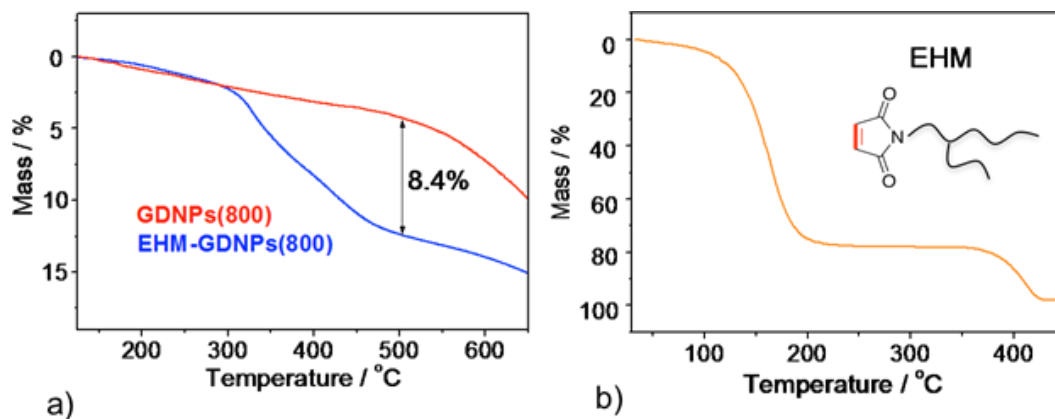


Figure 4.7 Thermogravimetric analysis (TGA) of **a)** thermally annealed GDNPs(800) (control system, red curve) and GDNPs(800) treated with the functional maleimide EHM (EHM-GDNP, blue curve), and **b)** the free EHM substituent. Note: the onset of evaporation of the free EHM substituents is observed at ca. 125 °C, while the onset of weight loss of EHM-GDNPs(800) shows beyond 300 °C (not seen in unfunctionalized GDNPs(800)).

4.3.3 Binding Strategy Investigation through Solid-state NMR (SS-NMR)

A number of solid-state NMR (SS-NMR) analyses were performed to validate the apparent bond-forming reaction taking place between EHM and the nanodiamond surface (**Figure 4.8** and **Figure 4.9**). In **Figure 4.9**, the 1D ^{13}C magic-angle spinning (MAS) NMR spectrum of the thermally annealed GDNPs(800) (**Figure 4.9a**) shows only one resonance at 33.4 ppm, characteristic of the sp^3 -hybridized carbon content of the nanodiamond precursor.¹³⁵⁻¹³⁹ Meanwhile, the 1D ^1H MAS spectrum of the GDNPs (**Figure 4.9b**) shows a broad resonance in the range 1-4 ppm, consisting of an overlap of several peaks, including resonances associated to CH_X groups.^{135-139, 170} The presence of CH_X surface groups (such as CH and CH_2) can be confirmed by 1D ^{13}C cross-polarization (CP)/MAS^{135-139, 170, 171} (**Figure 4.8a**, peak at 47.3 ppm), and by 2D $^{13}\text{C}\{^1\text{H}\}$ heteronuclear correlation (HETCOR)

spectroscopy (**Figure 4.8b**) analyses (here, the use of a short contact time for the CP step in this through-space dipolar correlation experiment is expected to lead to correlations between pairs of connected ^1H - ^{13}C spins only¹⁷²⁻¹⁷⁴). In **Figure 4.8b**, the clear ^1H - ^{13}C correlations at 0.8(^1H) and 45.2(^{13}C) ppm, and at 2.1(^1H) and 48.2(^{13}C) ppm, can be ascribed to the CH_2 and CH groups, respectively.

Figure 4.8c shows the 1D ^{13}C CP/MAS spectrum of the thermally annealed GDNPs(800) treated by an unsubstituted maleimide (M). In comparison with the 1D ^{13}C CP/MAS spectrum of the GDNP precursors prior to M-treatment (**Fig. 4.8a**), the spectrum of M-treated GDNPs shows an additional peak of pronounced intensity at 173 ppm (C2/blue dot), characteristic of the $\text{C}=\text{O}$ group pertaining to the control maleimide substituent M; the solution ^{13}C NMR spectrum of M (**Figure 4.10**) is provided. However, it is worth noting that the second peak at 135 ppm, characteristic of the alkene in M (**Figure 4.10**), is absent in the 1D ^{13}C CP/MAS spectrum of M-treated GDNP – an observation consistent with the apparent loss of the bending modes at 693 cm^{-1} and 827 cm^{-1} seen earlier in the FTIR spectrum of EHM-treated GDNPs (**Figure 4.3**). While the occurrence of extra sp^3 -hybridized carbons (C1/red dot) at the nanodiamond surface upon binding of M is likely convoluted in the GDNP resonances at 34.5 and 47.3 ppm (**Figure 4.8c**), the 2D $^{13}\text{C}\{^1\text{H}\}$ HETCOR spectrum shown in **Figure 4.8d** indicates a new ^1H - ^{13}C correlation at 1.5(^1H) and 33(^{13}C) ppm, that is not initially present in the 2D $^{13}\text{C}\{^1\text{H}\}$ HETCOR spectrum of non-functionalized GDNPs (**Figure 4.8b**) – a result which confirms the occurrence of new sp^3 -hybridized carbons (C1/red dot) appended to the nanodiamond surface. The resonance at ca. 47(^{13}C) ppm is assigned to the CH_2 and CH groups that are initially present on the GDNP surface. Importantly, both the 1D ^{13}C CP/MAS and 2D $^{13}\text{C}\{^1\text{H}\}$ HETCOR spectra

of M-treated GDNP point to the occurrence of only one new type of sp^3 -hybridized carbon (CH or CH_2) at the nanodiamond surface upon binding of M. In **Figure 4.9c**, the 1H - 1H double-quantum (DQ) spectrum of M-treated GDNP shows a single autocorrelation peak for the proton resonance at 0.8 ppm, which corresponds to the CH_2 surface groups initially present at the nanodiamond outer shell. In contrast, the protons at 2.1 and 1.5 ppm (marked with red box) in **Figure 4.8d** do not show any autocorrelation footprint by 1H - 1H DQ analysis – a result which validates both the identity of the new sp^3 -hybridized carbons that occur upon binding: CH groups (C1/red dot, **Figure 4.8c**), and the binding scheme: a two-point binding reaction at the nanodiamond surface. This result was confirmed by examining the ^{13}C chemical shift anisotropy (CSA) of the C=O groups in M-treated GDNPs, which provides clear insight into the dynamics and the nature of the binding pattern.¹⁷⁵ In **Figure 4.8e**, the static ^{13}C NMR spectrum of M-GDNPs shows a broad structureless resonance in the region of interest (centered at *ca.* 173 ppm; circled red). While a one-point binding scheme would allow for axial rotations of M in the magnetic field, resulting in a sharp and isotropic C=O resonance (*i.e.* wide range of local orientations at the nuclear site), here the powder-like pattern observed in the static ^{13}C NMR spectrum of M-GDNPs indicate a fixed molecular orientation with respect to the external magnetic field. It can thus be concluded that a two-point binding scheme – most likely a concerted addition reaction – is taking place between maleimide and the outer shell of the nanodiamonds. The same demonstration applies to the GDNPs(800) treated with the functional maleimide derivative EHM, for which the 1D ^{13}C CP/MAS spectrum is provided as **Figure 4.8f**. Here, the large number of aliphatic carbons in EHM gives rise to several additional peaks (C3-C10/green dots) at lower chemical shift (11, 17, 10, 25 ppm) and changes the peak lineshape of the

broader resonance common to M-GDNPs (30-50 ppm); the 2D $^{13}\text{C}\{^1\text{H}\}$ HETCOR analysis in the (Figure 4.9d) allows for the detailed peak assignment. As in M-GDNPs, the 1D ^{13}C CP/MAS spectrum of EHM-treated GDNPs shows a peak of pronounced intensity at 173 ppm (C2/blue dot), characteristic of the C=O group pertaining to EHM, and is in agreement with the presence of bound EHM at the nanodiamond surface. This step shows that the protocol of direct functionalization with maleimide is applicable to other substituted derivatives, such as the solubilizing alkyls commonly used to improve the stability of a variety of nanoparticles in solution.¹⁷⁶

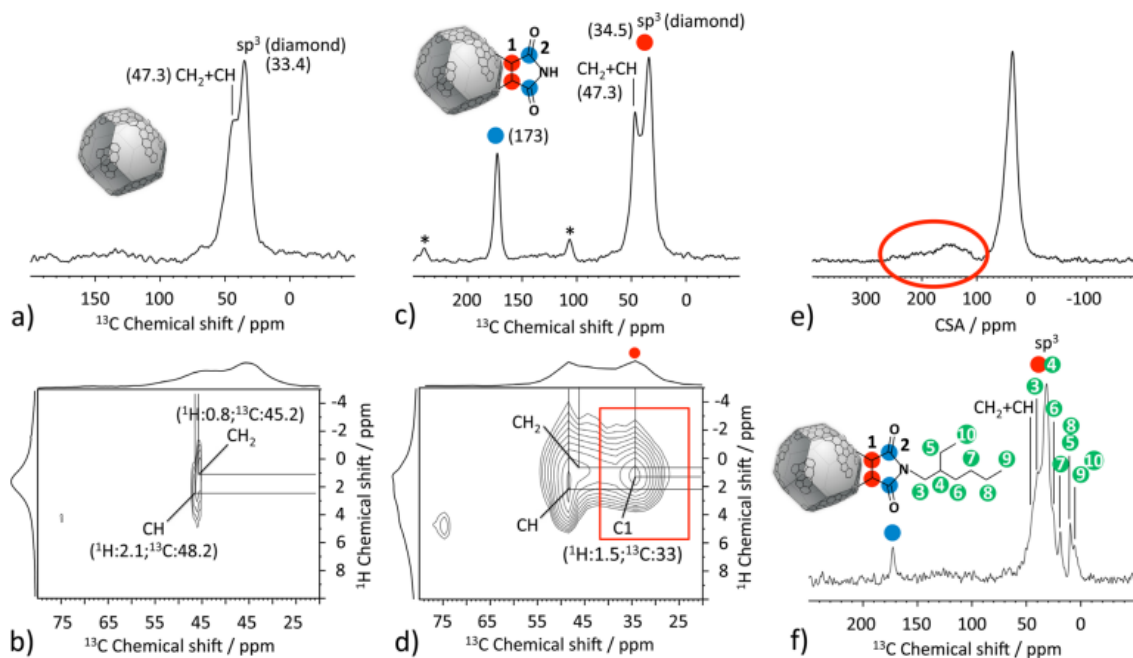


Figure 4.8 a) 1D ^{13}C CP/MAS solid-state NMR spectrum of thermally annealed GDNPs(800); b) 2D $^{13}\text{C}\{^1\text{H}\}$ HETCOR spectra of the GDNPs(800); c) 1D ^{13}C CP/MAS solid-state NMR spectrum of GDNPs(800) treated with the control unsubstituted maleimide M (M-GDNP); d) 2D $^{13}\text{C}\{^1\text{H}\}$ HETCOR spectra of the M-GDNPs; e) 1D ^{13}C CP/static solid-state NMR spectrum of the M-GDNPs; f) 1D ^{13}C CP/MAS solid-state NMR

spectrum of GDNPs(800) treated with the functional maleimide EHM (EHM-GDNP). The molecular structures and peak assignments are indicated on the spectra.

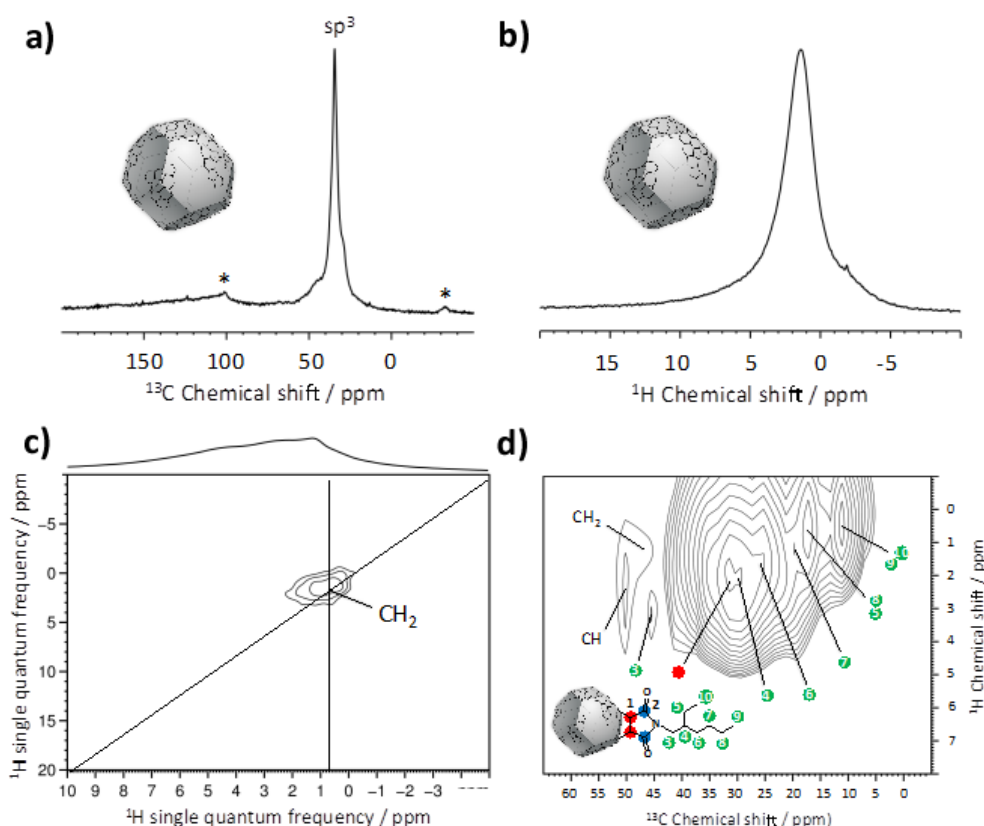


Figure 4.9 a) 1D ^{13}C MAS solid-state NMR spectrum of thermally annealed GDNPs(800). In the absence of ^1H decoupling, the resonance observed in Fig. 2a (at *ca.* 47.3 ppm) and pertaining to hydrogen-substituted carbons (CH, CH_2) cannot be observed. Here, a 1D ^{13}C CP/MAS analysis is required to account for the low content of hydrogen-substituted carbons located at the nanodiamond surface (also see Fig. 4.9b). b) 1D ^1H MAS solid-state NMR spectrum of thermally annealed GDNPs(800). c) ^1H - ^1H double-quantum (DQ) analysis of M-treated GDNPs(800) treated with the control unsubstituted maleimide M (M-GDNP). DQ signals in the w_1 dimension are observed at frequencies corresponding to the sum of single quantum (SQ) frequencies of protons that are close to one another in

space and will correlate in the w_2 dimension with the corresponding ordinary proton resonances. DQ correlation analyses can serve to identify equivalent protons, and is useful here to differentiate between CH and CH₂ moieties. **d)** 2D $^{13}\text{C}\{^1\text{H}\}$ HETCOR spectra of GDNPs(800) treated with the functional maleimide EHM (EHM-GDNP). The molecular structure (EHM) and peak assignments are indicated on the 2D spectrum.

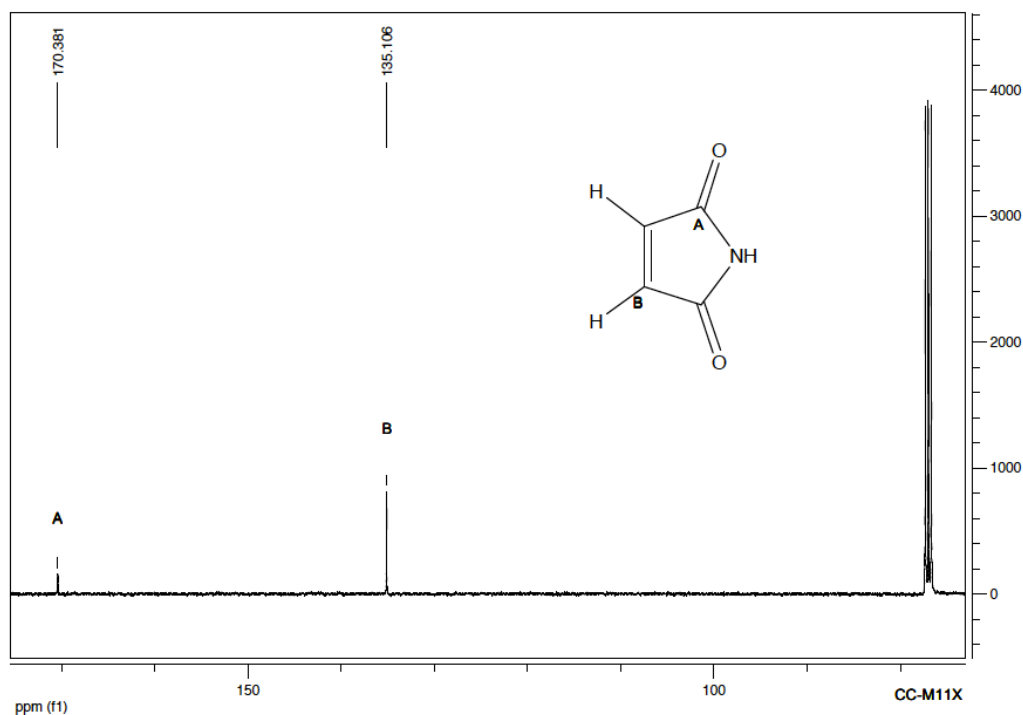


Figure 4.10 Solution ^{13}C NMR spectrum of maleimide M (free substituent).

4.3.4 Functionalization of Annealed DDNPs with Maleimide-derivatized Fluorescein Dye

In parallel, **Figure 4.11** shows that thermally annealed GDNPs labeled with a maleimide-derivatized fluorescein dye (**Figure 4.11a**) can yield fluorescent nanodiamonds (**Figure 4.11b**), which pave the path to the use of nanodiamond templates for sensing and

bioimaging.^{1a} FTIR, UV-Vis and fluorescence spectra, fluorescence microscopy images are provided in the **Figure 4.12**, **Figure 4.13** and **Figure 4.14**.

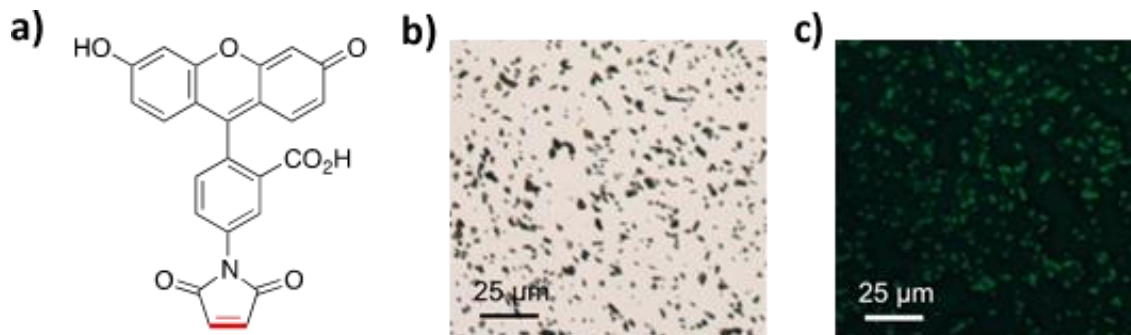


Figure 4.11 a) Fluorescein-5-maleimide (F5M); b) bright-field and c) fluorescence microscopy images of the GDNPs(800) treated with the fluorescent F5M dye (F5M-GDNP), and spun-coated on glass.

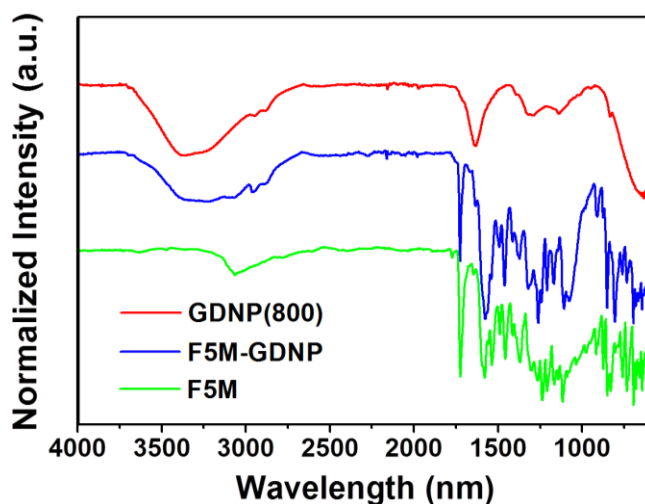


Figure 4.12 FTIR spectra of thermally annealed GDNPs(800) (red curve), the unfunctionalized fluorescein-5-maleimide (F5M) dye (green curve), and GDNPs(800) treated with F5M (F5M-GDNP) (blue curve).

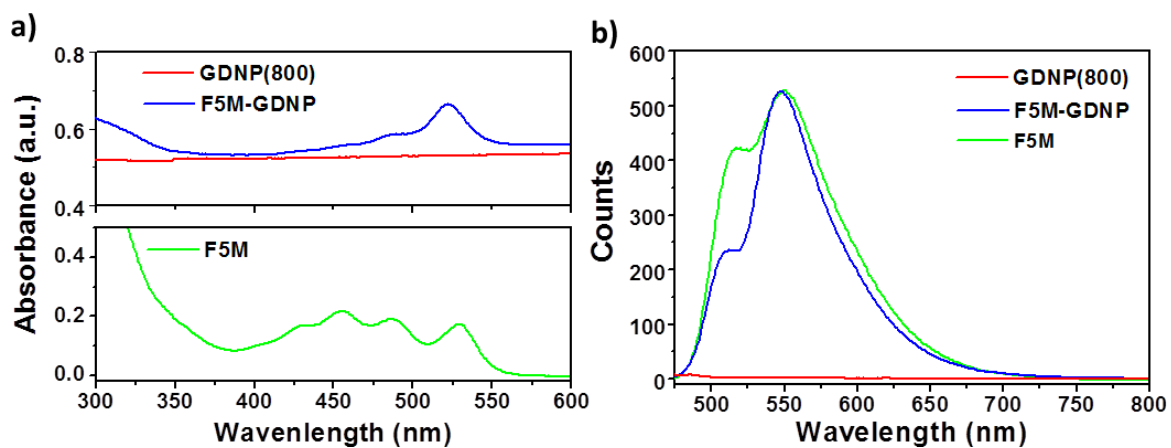


Figure 4.13 a) UV-Vis and b) Fluorescence spectra (in solution) of thermally annealed GDNPs(800) (red curve), the unfunctionalized fluorescein-5-maleimide (F5M) dye (green curve), and GDNPs(800) treated with F5M (F5M-GDNP) (blue curve).

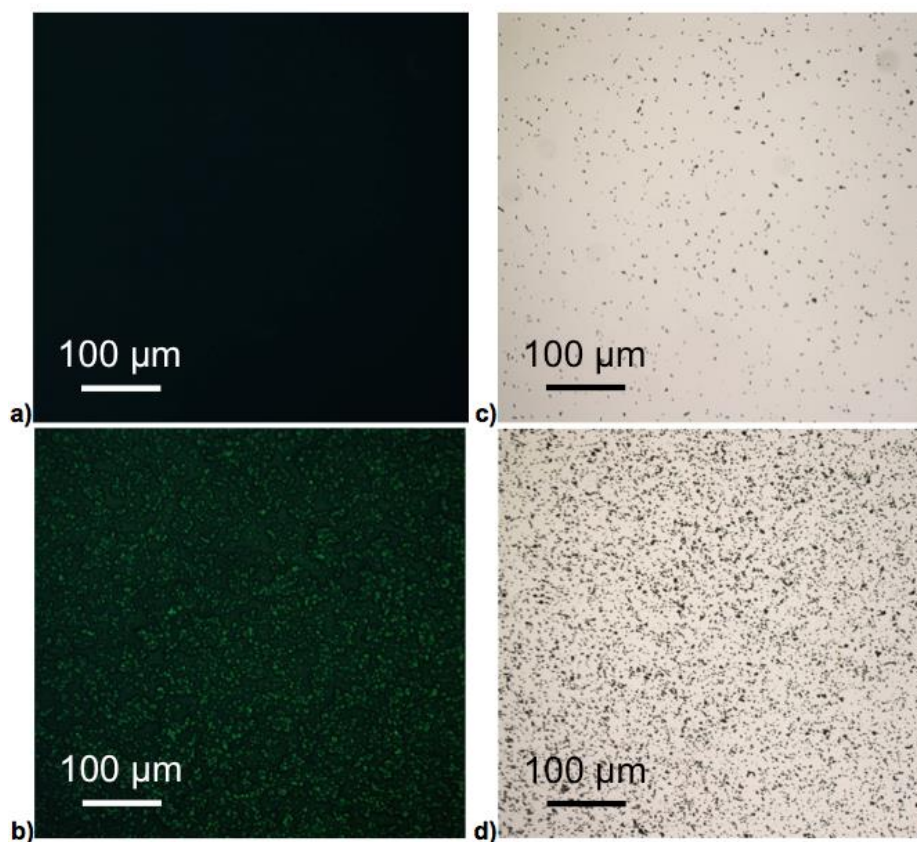


Figure 4.14 Fluorescence microscopy images of **a)** thermally annealed GDNPs(800) and **b)** the GDNPs(800) treated with the fluorescent F5M dye (F5M-GDNP); spun-coated on glass. **c)** and **d)** Bright-field microscopy images of the GDNPs(800) and F5M-GDNP, respectively.

4.4 Conclusion

In summary, using a combination of FTIR and SS-NMR analyses, we have shown that maleimide-derivatized substituents can be effectively appended to the *graphite-like* outer shell of thermally annealed nanodiamonds. From the 2D $^{13}\text{C}\{^1\text{H}\}$ HETCOR, $^1\text{H}\text{-}^1\text{H}$ DQ and CAS NMR analyses performed, the step of direct functionalization between maleimide and the nanodiamond surface can be described as a two-point binding reaction involving

the alkene of the functional imide. Taking our fluorescein-substituted GDNP as a model system, this direct approach to functionalizing nanodiamonds under ambient conditions is amenable to the preparation of nanomaterials with tunable functional substituents, as required in the development of nanocomposites, surface coatings, nanoscale photonic devices, and sensing/imaging nanoprobles.

REFERENCES

- (1) Yang, Z. G.; Zhang, J. L.; Kintner-Meyer, M. C. W.; Lu, X. C.; Choi, D. W.; Lemmon, J. P.; Liu, J., Electrochemical Energy Storage for Green Grid. *Chem. Rev.* **2011**, *111* (5), 3577-3613.
- (2) Dell, R. M.; Rand, D. A. J., Energy Storage - a Key Technology for Global Energy Sustainability. *J. Power Sources* **2001**, *100* (1-2), 2-17.
- (3) Hall, P. J.; Bain, E. J., Energy-Storage Technologies and Electricity Generation. *Energ Policy* **2008**, *36* (12), 4352-4355.
- (4) Kaempgen, M.; Chan, C. K.; Ma, J.; Cui, Y.; Gruner, G., Printable Thin Film Supercapacitors Using Single-Walled Carbon Nanotubes. *Nano Lett.* **2009**, *9* (5), 1872-1876.
- (5) Winter, M.; Brodd, R. J., What Are Batteries, Fuel Cells, and Supercapacitors? *Chem. Rev.* **2004**, *104* (10), 4245-4269.
- (6) Conway, B. E., Electrochemical Supercapacitors, Scientific, Fundamentals and Technological Applications. *Plenum Press* **1999**, New York.
- (7) Armand, M.; Tarascon, J. M., Building Better Batteries. *Nature* **2008**, *451* (7179), 652-657.
- (8) Simon, P.; Gogotsi, Y., Materials for Electrochemical Capacitors. *Nat. Mater.* **2008**, *7* (11), 845-854.

- (9) Rolison, D. R.; Long, J. W.; Lytle, J. C.; Fischer, A. E.; Rhodes, C. P.; McEvoy, T. M.; Bourga, M. E.; Lubers, A. M., Multifunctional 3d Nanoarchitectures for Energy Storage and Conversion. *Chem. Soc. Rev.* **2009**, *38* (1), 226-252.
- (10) Zhao, X.; Sanchez, B. M.; Dobson, P. J.; Grant, P. S., The Role of Nanomaterials in Redox-Based Supercapacitors for Next Generation Energy Storage Devices. *Nanoscale* **2011**, *3* (3), 839-855.
- (11) Stoller, M. D.; Park, S. J.; Zhu, Y. W.; An, J. H.; Ruoff, R. S., Graphene-Based Ultracapacitors. *Nano Lett.* **2008**, *8* (10), 3498-3502.
- (12) Dunn, B.; Kamath, H.; Tarascon, J. M., Electrical Energy Storage for the Grid: A Battery of Choices. *Science* **2011**, *334* (6058), 928-935.
- (13) Zhang, L. L.; Zhao, X. S., Carbon-Based Materials as Supercapacitor Electrodes. *Chem. Soc. Rev.* **2009**, *38* (9), 2520-2531.
- (14) Naoi, K.; Ishimoto, S.; Miyamoto, J.; Naoi, W., Second Generation 'Nanohybrid Supercapacitor': Evolution of Capacitive Energy Storage Devices. *Energ Environ Sci* **2012**, *5* (11), 9363-9373.
- (15) Jiang, J.; Li, Y. Y.; Liu, J. P.; Huang, X. T.; Yuan, C. Z.; Lou, X. W., Recent Advances in Metal Oxide-Based Electrode Architecture Design for Electrochemical Energy Storage. *Adv. Mater.* **2012**, *24* (38), 5166-5180.

- (16) Zhai, Y. P.; Dou, Y. Q.; Zhao, D. Y.; Fulvio, P. F.; Mayes, R. T.; Dai, S., Carbon Materials for Chemical Capacitive Energy Storage. *Adv. Mater.* **2011**, *23* (42), 4828-4850.
- (17) Candelaria, S. L.; Shao, Y. Y.; Zhou, W.; Li, X. L.; Xiao, J.; Zhang, J. G.; Wang, Y.; Liu, J.; Li, J. H.; Cao, G. Z., Nanostructured Carbon for Energy Storage and Conversion. *Nano Energy* **2012**, *1* (2), 195-220.
- (18) Wang, G. P.; Zhang, L.; Zhang, J. J., A Review of Electrode Materials for Electrochemical Supercapacitors. *Chem. Soc. Rev.* **2012**, *41* (2), 797-828.
- (19) Wu, X. L.; Xu, A. W., Carbonaceous Hydrogels and Aerogels for Supercapacitors. *Journal of Materials Chemistry A* **2014**, *2* (14), 4852-4864.
- (20) Nyholm, L.; Nystrom, G.; Mihranyan, A.; Stromme, M., Toward Flexible Polymer and Paper-Based Energy Storage Devices. *Adv. Mater.* **2011**, *23* (33), 3751-3769.
- (21) Hu, L. B.; Chen, W.; Xie, X.; Liu, N. A.; Yang, Y.; Wu, H.; Yao, Y.; Pasta, M.; Alshareef, H. N.; Cui, Y., Symmetrical MnO₂-Carbon Nanotube-Textile Nanostructures for Wearable Pseudocapacitors with High Mass Loading. *Acs Nano* **2011**, *5* (11), 8904-8913.
- (22) Chen, W.; Rakhi, R. B.; Hu, L. B.; Xie, X.; Cui, Y.; Alshareef, H. N., High-Performance Nanostructured Supercapacitors on a Sponge. *Nano Lett.* **2011**, *11* (12), 5165-5172.

- (23) Rakhi, R. B.; Chen, W.; Hedhili, M. N.; Cha, D.; Alshareef, H. N., Enhanced Rate Performance of Mesoporous Co₃O₄ Nanosheet Supercapacitor Electrodes by Hydrous RuO₂ Nanoparticle Decoration. *Acs Appl Mater Inter* **2014**, *6* (6), 4196-4206.
- (24) Xia, C.; Alshareef, H. N., Self-Templating Scheme for the Synthesis of Nanostructured Transition-Metal Chalcogenide Electrodes for Capacitive Energy Storage. *Chem. Mater.* **2015**, *27* (13), 4661-4668.
- (25) Chen, W.; Xia, C.; Alshareef, H. N., One-Step Electrodeposited Nickel Cobalt Sulfide Nanosheet Arrays for High-Performance Asymmetric Supercapacitors. *Acs Nano* **2014**, *8* (9), 9531-9541.
- (26) Snook, G. A.; Kao, P.; Best, A. S., Conducting-Polymer-Based Supercapacitor Devices and Electrodes. *J. Power Sources* **2011**, *196* (1), 1-12.
- (27) Gurunathan, K.; Murugan, A. V.; Marimuthu, R.; Mulik, U. P.; Amalnerkar, D. P., Electrochemically Synthesised Conducting Polymeric Materials for Applications Towards Technology in Electronics, Optoelectronics and Energy Storage Devices. *Mater. Chem. Phys.* **1999**, *61* (3), 173-191.
- (28) Zhang, Y.; Feng, H.; Wu, X. B.; Wang, L. Z.; Zhang, A. Q.; Xia, T. C.; Dong, H. C.; Li, X. F.; Zhang, L. S., Progress of Electrochemical Capacitor Electrode Materials: A Review. *Int. J. Hydrogen Energy* **2009**, *34* (11), 4889-4899.

- (29) Conway, B. E.; Birss, V.; Wojtowicz, J., The Role and Utilization of Pseudocapacitance for Energy Storage by Supercapacitors. *J. Power Sources* **1997**, *66* (1-2), 1-14.
- (30) Chuang, C. M.; Huang, C. W.; Teng, H. S.; Ting, J. M., Effects of Carbon Nanotube Grafting on the Performance of Electric Double Layer Capacitors. *Energ Fuel* **2010**, *24*, 6476-6482.
- (31) Zhi, M. J.; Xiang, C. C.; Li, J. T.; Li, M.; Wu, N. Q., Nanostructured Carbon-Metal Oxide Composite Electrodes for Supercapacitors: A Review. *Nanoscale* **2013**, *5* (1), 72-88.
- (32) Piao, Y. Z.; Kim, H. S.; Sung, Y. E.; Hyeon, T., Facile Scalable Synthesis of Magnetite Nanocrystals Embedded in Carbon Matrix as Superior Anode Materials for Lithium-Ion Batteries. *Chem. Commun.* **2010**, *46* (1), 118-120.
- (33) Jiang, J.; Zhu, J. H.; Ding, R. M.; Li, Y. Y.; Wu, F.; Liu, J. P.; Huang, X. T., Co-Fe Layered Double Hydroxide Nanowall Array Grown from an Alloy Substrate and Its Calcined Product as a Composite Anode for Lithium-Ion Batteries. *J. Mater. Chem.* **2011**, *21* (40), 15969-15974.
- (34) Chen, J. S.; Zhang, Y. M.; Lou, X. W., One-Pot Synthesis of Uniform Fe₃O₄ Nanospheres with Carbon Matrix Support for Improved Lithium Storage Capabilities. *Acs Appl Mater Inter* **2011**, *3* (9), 3276-3279.

- (35) Wang, Z. Y.; Chen, J. S.; Zhu, T.; Madhavi, S.; Lou, X. W., One-Pot Synthesis of Uniform Carbon-Coated Moo_2 Nanospheres for High-Rate Reversible Lithium Storage. *Chem. Commun.* **2010**, 46 (37), 6906-6908.
- (36) Kang, E.; Jung, Y. S.; Cavanagh, A. S.; Kim, G. H.; George, S. M.; Dillon, A. C.; Kim, J. K.; Lee, J., Fe_3O_4 Nanoparticles Confined in Mesocellular Carbon Foam for High Performance Anode Materials for Lithium-Ion Batteries. *Adv. Funct. Mater.* **2011**, 21 (13), 2430-2438.
- (37) Yang, S. B.; Feng, X. L.; Ivanovici, S.; Mullen, K., Fabrication of Graphene-Encapsulated Oxide Nanoparticles: Towards High-Performance Anode Materials for Lithium Storage. *Angew. Chem. Int. Ed.* **2010**, 49 (45), 8408-8411.
- (38) Jiang, J.; Zhu, J. H.; Feng, Y. M.; Liu, J. P.; Huang, X. T., A Novel Evolution Strategy to Fabricate a 3d Hierarchical Interconnected Core-Shell Ni/ Mno_2 Hybrid for Li-Ion Batteries. *Chem. Commun.* **2012**, 48 (60), 7471-7473.
- (39) Jiang, J.; Liu, J. P.; Zhou, W. W.; Zhu, J. H.; Huang, X. T.; Qi, X. Y.; Zhang, H.; Yu, T., Cnt/Ni Hybrid Nanostructured Arrays: Synthesis and Application as High-Performance Electrode Materials for Pseudocapacitors. *Energ Environ Sci* **2011**, 4 (12), 5000-5007.
- (40) Reddy, A. L. M.; Shaijumon, M. M.; Gowda, S. R.; Ajayan, P. M., Coaxial Mno_2 /Carbon Nanotube Array Electrodes for High-Performance Lithium Batteries. *Nano Lett.* **2009**, 9 (3), 1002-1006.

- (41) Xia, C.; Chen, W.; Wang, X. B.; Hedhili, M. N.; Wei, N. N.; Alshareef, H. N., Highly Stable Supercapacitors with Conducting Polymer Core-Shell Electrodes for Energy Storage Applications. *Advanced Energy Materials* **2015**, *5* (8).
- (42) Fan, L. Z.; Hu, Y. S.; Maier, J.; Adelhelm, P.; Smarsly, B.; Antonietti, M., High Electroactivity of Polyaniline in Supercapacitors by Using a Hierarchically Porous Carbon Monolith as a Support. *Adv. Funct. Mater.* **2007**, *17* (16), 3083-3087.
- (43) Hohnholz, D.; MacDiarmid, A. G.; Sarno, D. M.; Jones, W. E., Uniform Thin Films of Poly-3,4-Ethylenedioxythiophene (Pedot) Prepared by in-Situ Deposition. *Chem. Commun.* **2001**, (23), 2444-2445.
- (44) Yan, J.; Wang, Q.; Wei, T.; Fan, Z. J., Recent Advances in Design and Fabrication of Electrochemical Supercapacitors with High Energy Densities. *Advanced Energy Materials* **2014**, *4* (4).
- (45) Nagaraju, D. H.; Wang, Q. X.; Beaujuge, P.; Alshareef, H. N., Two-Dimensional Heterostructures of V₂O₅ and Reduced Graphene Oxide as Electrodes for High Energy Density Asymmetric Supercapacitors. *Journal of Materials Chemistry A* **2014**, *2* (40), 17146-17152.
- (46) Rakhi, R. B.; Chen, W.; Cha, D. Y.; Alshareef, H. N., Substrate Dependent Self-Organization of Mesoporous Cobalt Oxide Nanowires with Remarkable Pseudocapitance. *Nano Lett.* **2012**, *12* (5), 2559-2567.

- (47) Li, N. C.; Patrissi, C. J.; Che, G. L.; Martin, C. R., Rate Capabilities of Nanostructured LiMn_2O_4 Electrodes in Aqueous Electrolyte. *J. Electrochem. Soc.* **2000**, *147* (6), 2044-2049.
- (48) Liu, H.; Su, D. W.; Zhou, R. F.; Sun, B.; Wang, G. X.; Qiao, S. Z., Highly Ordered Mesoporous MoS_2 with Expanded Spacing of the (002) Crystal Plane for Ultrafast Lithium Ion Storage. *Advanced Energy Materials* **2012**, *2* (8), 970-975.
- (49) Liu, H.; Du, X. W.; Xing, X. R.; Wang, G. X.; Qiao, S. Z., Highly Ordered Mesoporous Cr_2O_3 Materials with Enhanced Performance for Gas Sensors and Lithium Ion Batteries. *Chem. Commun.* **2012**, *48* (6), 865-867.
- (50) Arico, A. S.; Bruce, P.; Scrosati, B.; Tarascon, J. M.; Van Schalkwijk, W., Nanostructured Materials for Advanced Energy Conversion and Storage Devices. *Nat. Mater.* **2005**, *4* (5), 366-377.
- (51) Miller, J. R.; Simon, P., Materials Science - Electrochemical Capacitors for Energy Management. *Science* **2008**, *321* (5889), 651-652.
- (52) Poizot, P.; Dolhem, F., Clean Energy New Deal for a Sustainable World: From Non- CO_2 Generating Energy Sources to Greener Electrochemical Storage Devices. *Energy Environ Sci* **2011**, *4* (6), 2003-2019.
- (53) Thompson, B. C.; Frechet, J. M. J., Organic Photovoltaics - Polymer-Fullerene Composite Solar Cells. *Angew. Chem. Int. Ed.* **2008**, *47* (1), 58-77.

(54) Beaujuge, P. M.; Reynolds, J. R., Color Control in Pi-Conjugated Organic Polymers for Use in Electrochromic Devices. *Chem. Rev.* **2010**, *110* (1), 268-320.

(55) Simon, P.; Gogotsi, Y.; Dunn, B., Where Do Batteries End and Supercapacitors Begin? *Science* **2014**, *343* (6176), 1210-1211.

(56) Lota, K.; Khomenko, V.; Frackowiak, E., Capacitance Properties of Poly(3,4-Ethylenedioxythiophene)/Carbon Nanotubes Composites. *J. Phys. Chem. Solids* **2004**, *65* (2-3), 295-301.

(57) Mastragostino, M.; Arbizzani, C.; Soavi, F., Polymer-Based Supercapacitors. *J. Power Sources* **2001**, *97-8*, 812-815.

(58) Rudge, A.; Davey, J.; Raistrick, I.; Gottesfeld, S.; Ferraris, J. P., Conducting Polymers as Active Materials in Electrochemical Capacitors. *J. Power Sources* **1994**, *47* (1-2), 89-107.

(59) Estrada, L. A.; Liu, D. Y.; Salazar, D. H.; Dyer, A. L.; Reynolds, J. R., Poly[Bis-Edot-Isoindigo]: An Electroactive Polymer Applied to Electrochemical Supercapacitors. *Macromolecules* **2012**, *45* (20), 8211-8220.

(60) Gottesfeld, S.; Redondo, A., On the Mechanism of Electrochemical Switching in Films of Polyaniline. *J. Electrochem. Soc.* **1987**, *134* (1), 271-272.

(61) Rudge, A.; Raistrick, I.; Gottesfeld, S.; Ferraris, J. P., A Study of the Electrochemical Properties of Conducting Polymers for Application in Electrochemical Capacitors. *Electrochim. Acta* **1994**, *39* (2), 273-287.

- (62) Mastragostino, M.; Arbizzani, C.; Paraventi, R.; Zanelli, A., Polymer Selection and Cell Design for Electric-Vehicle Supercapacitors. *J. Electrochem. Soc.* **2000**, *147* (2), 407-412.
- (63) Patra, S.; Munichandraiah, N., Supercapacitor Studies of Electrochemically Deposited Pedot on Stainless Steel Substrate. *J. Appl. Polym. Sci.* **2007**, *106* (2), 1160-1171.
- (64) Wang, K.; Wu, H.; Meng, Y.; Wei, Z., Conducting Polymer Nanowire Arrays for High Performance Supercapacitors. *Small* **2014**, *10* (1), 14-31.
- (65) Wang, G.; Zhang, L.; Zhang, J., A Review of Electrode Materials for Electrochemical Supercapacitors. *Chem. Soc. Rev.* **2012**, *41* (2), 797-828.
- (66) Yan, J.; Wang, Q.; Wei, T.; Fan, Z., Recent Advances in Design and Fabrication of Electrochemical Supercapacitors with High Energy Densities. *Adv. Energy Mater.* **2014**, *4* (4), 1300816-1300816.
- (67) Roncali, J., Synthesis and Properties of Polythiophenes. In *Conductive Electroactive Polymers*, CRC Press: **2008**, pp 197-230.
- (68) Wang, X.; Sjöberg-Eerola, P.; Eriksson, J.-E.; Bobacka, J.; Bergelin, M., The Effect of Counter Ions and Substrate Material on the Growth and Morphology of Poly(3,4-Ethylenedioxythiophene) Films: Towards the Application of Enzyme Electrode Construction in Biofuel Cells. *Synth. Met.* **2010**, *160* (13–14), 1373-1381.

- (69) Cheng, Q.; Tang, J.; Ma, J.; Zhang, H.; Shinya, N.; Qin, L.-C., Polyaniline-Coated Electro-Etched Carbon Fiber Cloth Electrodes for Supercapacitors. *J. Phys. Chem. C* **2011**, *115* (47), 23584-23590.
- (70) Liu, T.; Finn, L.; Yu, M.; Wang, H.; Zhai, T.; Lu, X.; Tong, Y.; Li, Y., Polyaniline and Polypyrrole Pseudocapacitor Electrodes with Excellent Cycling Stability. *Nano Lett.* **2014**, *14* (5), 2522-2527.
- (71) Bora, C.; Sharma, J.; Dolui, S., Polypyrrole/Sulfonated Graphene Composite as Electrode Material for Supercapacitor. *J. Phys. Chem. C* **2014**, *118* (51), 29688-29694.
- (72) Zhang, H.; Hu, L.; Tu, J.; Jiao, S., Electrochemically Assembling of Polythiophene Film in Ionic Liquids (ILs) Microemulsions and Its Application in an Electrochemical Capacitor. *Electrochim. Acta* **2014**, *120* (0), 122-127.
- (73) D'Arcy, J. M.; El-Kady, M. F.; Khine, P. P.; Zhang, L.; Lee, S. H.; Davis, N. R.; Liu, D. S.; Yeung, M. T.; Kim, S. Y.; Turner, C. L.; Lech, A. T.; Hammond, P. T.; Kaner, R. B., Vapor-Phase Polymerization of Nanofibrillar Poly(3,4-Ethylenedioxythiophene) for Supercapacitors. *ACS Nano* **2014**, *8* (2), 1500-1510.
- (74) Pandey, G. P.; Rastogi, A. C.; Westgate, C. R., All-Solid-State Supercapacitors with Poly(3,4-Ethylenedioxythiophene)-Coated Carbon Fiber Paper Electrodes and Ionic Liquid Gel Polymer Electrolyte. *J. Power Sources* **2014**, *245* (0), 857-865.

(75) Park, H.-W.; Kim, T.; Huh, J.; Kang, M.; Lee, J. E.; Yoon, H., Anisotropic Growth Control of Polyaniline Nanostructures and Their Morphology-Dependent Electrochemical Characteristics. *ACS Nano* **2012**, *6* (9), 7624-7633.

(76) Cooper, A. I., Conjugated Microporous Polymers. *Adv. Mater.* **2009**, *21* (12), 1291-1295.

(77) Xu, Y.; Jin, S.; Xu, H.; Nagai, A.; Jiang, D., Conjugated Microporous Polymers: Design, Synthesis and Application. *Chem. Soc. Rev.* **2013**, *42* (20), 8012-8031.

(78) Cherioux, F.; Guyard, L., Synthesis and Electrochemical Properties of Novel 1,3,5-Tris(Oligothieryl)Benzenes: A New Generation of 3d Reticulating Agents. *Adv. Funct. Mater.* **2001**, *11* (4), 305-309.

(79) Ponomarenko, S. A.; Tatarinova, E. A.; Muzafarov, A. M.; Kirchmeyer, S.; Brassat, L.; Mourran, A.; Moeller, M.; Setayesh, S.; de Leeuw, D., Star-Shaped Oligothiophenes for Solution-Processible Organic Electronics: Flexible Aliphatic Spacers Approach. *Chem. Mater.* **2006**, *18* (17), 4101-4108.

(80) Chahma, M. h.; Gilroy, J. B.; Hicks, R. G., Linear and Branched Electroactive Polymers Based on Ethylenedioxythiophene-Triarylamine Conjugates. *J. Mater. Chem.* **2007**, *17* (45), 4768-4771.

(81) Kearns, J. T.; Roberts, M. E., Enhanced Performance of Triarylamine Redox Electrodes through Directed Electrochemical Polymerization. *J. Mater. Chem.* **2012**, *22* (6), 2392-2394.

(82) Kearns, J. T.; Roberts, M. E., Synthesis of High-Charge Capacity Triarylamine-Thiophene Redox Electrodes Using Electrochemical Copolymerization. *J. Mater. Chem.* **2012**, *22* (48), 25447-25452.

(83) Roberts, M. E.; Wheeler, D. R.; McKenzie, B. B.; Bunker, B. C., High Specific Capacitance Conducting Polymer Supercapacitor Electrodes Based on Poly(Tris(Thiophenylphenyl)Amine). *J. Mater. Chem.* **2009**, *19* (38), 6977-6979.

(84) Kashiki, T.; Kohara, M.; Osaka, I.; Miyazaki, E.; Takimiya, K., Synthesis and Characterization of Benzo[1,2-B:3,4-B':5,6-B''']Trithiophene (Btt) Oligomers. *J. Org. Chem.* **2011**, *76* (10), 4061-4070.

(85) Nicolas, Y.; Blanchard, P.; Levillain, E.; Allain, M.; Mercier, N.; Roncali, J., Planarized Star-Shaped Oligothiophenes with Enhanced π -Electron Delocalization. *Org. Lett.* **2003**, *6* (2), 273-276.

(86) Taerum, T.; Lukyanova, O.; Wylie, R. G.; Perepichka, D. F., Synthesis, Polymerization, and Unusual Properties of New Star-Shaped Thiophene Oligomers. *Org. Lett.* **2009**, *11* (15), 3230-3233.

(87) Chen, G. Z., Understanding Supercapacitors Based on Nano-Hybrid Materials with Interfacial Conjugation. *Prog. Nat. Sci.: Mater. Int.* **2013**, *23* (3), 245-255.

(88) Bäerle, P.; Götz, G.; Synowczyk, A.; Heinze, J., Donor-Substituted Oligothiophenes, 1 Synthesis and Properties of a Series of Methylthio Oligothiophenes. *Liebigs Annalen* **1996**, *1996* (2), 279-284.

(89) Gotz, G.; Scheib, S.; Klose, R.; Heinze, J.; Bauerle, P., Synthesis and Properties of a Series of Regioregularly Amino-Substituted Oligo- and Polythiophenes. *Adv. Funct. Mater.* **2002**, *12* (10), 723-728.

(90) Anothumakkool, B.; Torris A. T, A.; Bhange, S. N.; Badiger, M. V.; Kurungot, S., Electrodeposited Polyethylenedioxythiophene with Infiltrated Gel Electrolyte Interface: A Close Contest of an All-Solid-State Supercapacitor with Its Liquid-State Counterpart.

Nanoscale **2014**, *6* (11), 5944-5952.

(91) Mike, J. F.; Lutkenhaus, J. L., Recent Advances in Conjugated Polymer Energy Storage. *J. Polym. Sci., Part B: Polym. Phys.* **2013**, *51* (7), 468-480.

(92) Ertas, M.; Walczak, R. M.; Das, R. K.; Rinzler, A. G.; Reynolds, J. R., Supercapacitors Based on Polymeric Dioxypyrroles and Single Walled Carbon Nanotubes. *Chem. Mater.* **2012**, *24* (3), 433-443.

(93) Zhou, H.; Han, G.; Xiao, Y.; Chang, Y.; Zhai, H.-J., Facile Preparation of Polypyrrole/Graphene Oxide Nanocomposites with Large Areal Capacitance Using Electrochemical Codeposition For supercapacitors. *J. Power Sources* **2014**, *263* (0), 259-267.

(94) Groenendaal, L.; Zotti, G.; Aubert, P. H.; Waybright, S. M.; Reynolds, J. R., Electrochemistry of Poly(3,4-Alkylenedioxythiophene) Derivatives. *Adv. Mater.* **2003**, *15* (11), 855-879.

(95) Rodríguez-Calero, G. G.; Lowe, M. A.; Kiya, Y.; Abruña, H. D., Electrochemical and Computational Studies on the Electrocatalytic Effect of Conducting Polymers toward the Redox Reactions of Thiadiazole-Based Thiolate Compounds. *J. Phys. Chem. C* **2010**, *114* (13), 6169-6176.

(96) Baur, J. E., 19 - Diffusion Coefficients. In *Handbook of Electrochemistry*, Zoski, C. G., Ed. Elsevier: Amsterdam, **2007**, pp 829-848.

(97) Creager, S., 3 - Solvents and Supporting Electrolytes. In *Handbook of Electrochemistry*, Zoski, C. G., Ed. Elsevier: Amsterdam, **2007**, pp 57-IV.

(98) Givehchi, M.; Tardi, M.; Polton, A.; Sigwalt, P., Influence of Monomer Concentration and Dielectric Constant on Transfer Reactions in the Carbocationic Polymerization of Indene. *Macromolecules* **2000**, *33* (3), 710-716.

(99) Matyjaszewski, K.; Lin, C.-H.; Bon, A.; Xiang, J. S., Salt and Solvent Effects in "Living" Carbocationic Polymerization. *Macromol. Symp.* **1994**, *85* (1), 65-78.

(100) Lu, W.; Fadeev, A. G.; Qi, B. H.; Smela, E.; Mattes, B. R.; Ding, J.; Spinks, G. M.; Mazurkiewicz, J.; Zhou, D. Z.; Wallace, G. G.; MacFarlane, D. R.; Forsyth, S. A.; Forsyth, M., Use of Ionic Liquids for Pi-Conjugated Polymer Electrochemical Devices. *Science* **2002**, *297* (5583), 983-987.

(101) Sellam; Hashmi, S. A., High Rate Performance of Flexible Pseudocapacitors Fabricated Using Ionic-Liquid-Based Proton Conducting Polymer Electrolyte with

Poly(3, 4-Ethylenedioxythiophene):Poly(Styrene Sulfonate) and Its Hydrous Ruthenium Oxide Composite Electrodes. *Acs Appl Mater Inter* **2013**, *5* (9), 3875-3883.

(102) Holbrey, J. D.; Seddon, K. R., Ionic Liquids. *Clean Products and Processes* **1999**, *1*.

(103) Wasserscheid, P.; Keim, W., Ionic Liquids - New "Solutions" for Transition Metal Catalysis. *Angew. Chem. Int. Ed.* **2000**, *39* (21), 3772-3789.

(104) Plechkova, N. V.; Seddon, K. R., Applications of Ionic Liquids in the Chemical Industry. *Chem. Soc. Rev.* **2008**, *37* (1), 123-150.

(105) Abbott, A. P.; McKenzie, K. J., Application of Ionic Liquids to the Electrodeposition of Metals. *PCCP* **2006**, *8* (37), 4265-4279.

(106) Endres, F.; Abbott, A.; MacFarlane, D. R., Electrodeposition from Ionic Liquids *Wiley-VCH* **2008**.

(107) Armand, M.; Endres, F.; MacFarlane, D. R.; Ohno, H.; Scrosati, B., Ionic-Liquid Materials for the Electrochemical Challenges of the Future. *Nat. Mater.* **2009**, *8* (8), 621-629.

(108) Heinze, J.; Frontana-Uribe, B. A.; Ludwigs, S., Electrochemistry of Conducting Polymers-Persistent Models and New Concepts. *Chem. Rev.* **2010**, *110* (8), 4724-4771.

(109) Earle, M. J.; Esperanca, J. M. S. S.; Gilea, M. A.; Lopes, J. N. C.; Rebelo, L. P. N.; Magee, J. W.; Seddon, K. R.; Widegren, J. A., The Distillation and Volatility of Ionic Liquids. *Nature* **2006**, *439* (7078), 831-834.

(110) MacFarlane, D. R.; Tachikawa, N.; Forsyth, M.; Pringle, J. M.; Howlett, P. C.; Elliott, G. D.; Davis, J. H.; Watanabe, M.; Simon, P.; Angell, C. A., Energy Applications of Ionic Liquids. *Energ Environ Sci* **2014**, *7* (1), 232-250.

(111) Pringle, J. M.; Forsyth, M.; MacFarlane, D. R.; Wagner, K.; Hall, S. B.; Officer, D. L., The Influence of the Monomer and the Ionic Liquid on the Electrochemical Preparation of Polythiophene. *Polymer* **2005**, *46* (7), 2047-2058.

(112) Snook, G. A.; Chen, G. Z., The Measurement of Specific Capacitances of Conducting Polymers Using the Quartz Crystal Microbalance. *J. Electroanal. Chem.* **2008**, *612* (1), 140-146.

(113) Laforgue, A.; Simon, P.; Sarrazin, C.; Fauvarque, J. F., Polythiophene-Based Supercapacitors. *J. Power Sources* **1999**, *80* (1-2), 142-148.

(114) Groenendaal, B. L.; Jonas, F.; Freitag, D.; Pielartzik, H.; Reynolds, J. R., Poly(3,4-Ethylenedioxythiophene) and Its Derivatives: Past, Present, and Future. *Adv. Mater.* **2000**, *12* (7), 481-494.

(115) Liu, K.; Hu, Z. L.; Xue, R.; Zhang, J. R.; Zhu, J. J., Electropolymerization of High Stable Poly(3,4-Ethylenedioxythiophene) in Ionic Liquids and Its Potential Applications in Electrochemical Capacitor. *J. Power Sources* **2008**, *179* (2), 858-862.

(116) Favre, C.; Abello, L.; Delabouglise, D., Effect of the Anion on the Level and Aging of the Conducting State of Electropolymerized 3-Methylthiophene Thin Films. *Adv. Mater.* **1997**, *9* (9), 722-725.

(117) Randriamahazaka, H.; Plesse, C.; Teyssie, D.; Chevrot, C., Electrochemical Behaviour of Poly(3,4-Ethylenedioxythiophene) in a Room-Temperature Ionic Liquid.

Electrochem. Commun. **2003**, *5* (7), 613-617.

(118) Randriamahazaka, H.; Plesse, C.; Teyssie, D.; Chevrot, C., Ions Transfer Mechanisms During the Electrochemical Oxidation of Poly(3,4-Ethylenedioxythiophene) in 1-Ethyl-3-Methylimidazolium Bis((Trifluoromethyl)Sulfonyl)Amide Ionic Liquid.

Electrochem. Commun. **2004**, *6* (3), 299-305.

(119) Wagner, K.; Pringle, J. M.; Hall, S. B.; Forsyth, M.; MacFarlane, D. R.; Officer, D. L., Investigation of the Electropolymerisation of Edot in Ionic Liquids. *Synth. Met.*

2005, *153* (1-3), 257-260.

(120) Ahmad, S.; Deepa, M.; Singh, S., Electrochemical Synthesis and Surface Characterization of Poly(3,4-Ethylenedioxythiophene) Films Grown in an Ionic Liquid.

Langmuir **2007**, *23* (23), 11430-11433.

(121) Sekiguchi, K.; Atobe, M.; Fuchigami, T., Electrooxidative Polymerization of Aromatic Compounds in 1-Ethyl-3-Methylimidazolium Trifluoromethanesulfonate

Room-Temperature Ionic Liquid. *J. Electroanal. Chem.* **2003**, *557*, 1-7.

(122) Damlin, P.; Kvarnstrom, C.; Ivaska, A., Electrochemical Synthesis and in Situ Spectroelectrochemical Characterization of Poly(3,4-Ethylenedioxythiophene) (Pedot) in

Room Temperature Ionic Liouids. *J. Electroanal. Chem.* **2004**, *570* (1), 113-122.

(123) Huddleston, J. G.; Visser, A. E.; Reichert, W. M.; Willauer, H. D.; Broker, G. A.; Rogers, R. D., Characterization and Comparison of Hydrophilic and Hydrophobic Room Temperature Ionic Liquids Incorporating the Imidazolium Cation. *Green Chem* **2001**, *3* (4), 156-164.

(124) Kitaoka, S.; Nobuoka, K.; Ishikawa, Y., Ionic Liquids for Tetraarylporphyrin Preparation. *Tetrahedron* **2005**, *61* (32), 7678-7685.

(125) Pringle, J. M.; MacFarlane, D. R.; Forsyth, M., Solid State Nmr Analysis of Polypyrrole Grown in a Phosphonium Ionic Liquid. *Synth. Met.* **2005**, *155* (3), 684-689.

(126) Randriamahazaka, H.; Plesse, C.; Teyssie, D.; Chevrot, C., Charging/Discharging Kinetics of Poly(3,4-Ethylenedioxythiophene) in 1-Ethyl-3-Methylimidazolium Bis-(Trifluoromethylsulfonyl)Imide Ionic Liquid under Galvanostatic Conditions. *Electrochim. Acta* **2005**, *50* (21), 4222-4229.

(127) Zotti, G.; Schiavon, G.; Zecchin, S., Irreversible-Processes in the Electrochemical Reduction of Polythiophenes - Chemical Modifications of the Polymer and Charge-Trapping Phenomena. *Synth. Met.* **1995**, *72* (3), 275-281.

(128) Wallace, G. G.; Innis, P. C., Inherently Conducting Polymer Nanostructures. *Journal of Nanoscience and Nanotechnology* **2002**, *2* (5), 441-451.

(129) Skompska, M., Alternative Explanation of Asymmetry in Cyclic Voltammograms for Redox Reaction of Poly(3-Methylthiophene) Films in Acetonitrile Solutions. *Electrochim. Acta* **1998**, *44* (2-3), 357-362.

- (130) Randriamahazaka, H.; Bonnotte, T.; Noel, V.; Martin, P.; Ghilane, J.; Asaka, K.; Lacroix, J. C., Medium Effects on the Nucleation and Growth Mechanisms During the Redox Switching Dynamics of Conducting Polymers: Case of Poly(3,4-Ethylenedioxythiophene). *J. Phys. Chem. B* **2011**, *115* (2), 205-216.
- (131) Chen, X. W.; Ingnas, O., Three-Step Redox in Polythiophenes: Evidence from Electrochemistry at an Ultramicroelectrode. *J. Phys. Chem.* **1996**, *100* (37), 15202-15206.
- (132) Mochalin, V. N.; Shenderova, O.; Ho, D.; Gogotsi, Y., The Properties and Applications of Nanodiamonds. *Nat. Nanotechnol.* **2012**, *7* (1), 11-23.
- (133) Schrand, A. M.; Hens, S. A. C.; Shenderova, O. A., Nanodiamond Particles: Properties and Perspectives for Bioapplications. *Crit. Rev. Solid State Mater. Sci.* **2009**, *34* (1-2), 18-74.
- (134) Krueger, A., Beyond the Shine: Recent Progress in Applications of Nanodiamond. *J. Mater. Chem.* **2011**, *21* (34), 12571-12578.
- (135) Dubois, M.; Guerin, K.; Petit, E.; Batische, N.; Hamwi, A.; Komatsu, N.; Giraudet, J.; Pirotte, P.; Masin, F., Solid-State Nmr Study of Nanodiamonds Produced by the Detonation Technique. *J. Phys. Chem. C* **2009**, *113* (24), 10371-10378.
- (136) Panich, A. M., Solid State Nuclear Magnetic Resonance Studies of Nanocarbons. *Diamond Relat. Mater.* **2007**, *16* (12), 2044-2049.

(137) Panich, A. M.; Shames, A. I.; Vieth, H. M.; Osawa, E.; Takahashi, M.; Vul', A. Y., Nuclear Magnetic Resonance Study of Ultrananocrystalline Diamonds. *Eur. Phys. J. B* **2006**, *52* (3), 397-402.

(138) Panich, A. M., Nuclear Magnetic Resonance Studies of Nanodiamonds. *Crit. Rev. Solid State Mater. Sci.* **2012**, *37* (4), 276-303.

(139) Dubois, M.; Guerin, K.; Batische, N.; Petit, E.; Hamwi, A.; Komatsu, N.; Kharbache, H.; Pirotte, P.; Masin, F., Solid State Nmr Study of Nanodiamond Surface Chemistry. *Solid State Nucl. Magn. Reson.* **2011**, *40* (4), 144-154.

(140) Shenderova, O.; Koscheev, A.; Zaripov, N.; Petrov, I.; Skryabin, Y.; Detkov, P.; Turner, S.; Van Tendeloo, G., Surface Chemistry and Properties of Ozone-Purified Detonation Nanodiamonds. *J. Phys. Chem. C* **2011**, *115* (20), 9827-9837.

(141) Mochalin, V. N.; Gogotsi, Y., Wet Chemistry Route to Hydrophobic Blue Fluorescent Nanodiamond. *J. Am. Chem. Soc.* **2009**, *131* (13), 4594-4595.

(142) Zhong, Y. L.; Loh, K. P.; Midya, A.; Chen, Z. K., Suzuki Coupling of Aryl Organics on Diamond. *Chem. Mater.* **2008**, *20* (9), 3137-3144.

(143) Yeap, W. S.; Chen, S.; Loh, K. P., Detonation Nanodiamond: An Organic Platform for the Suzuki Coupling of Organic Molecules. *Langmuir* **2009**, *25* (1), 185-191.

(144) Arnault, J.-C.; Petit, T.; Girard, H.; Chavanne, A.; Gesset, C.; Sennour, M.; Chaigneau, M., Surface Chemical Modifications and Surface Reactivity of Nanodiamonds Hydrogenated by Cvd Plasma. *PCCP* **2011**, *13* (24), 11481-11487.

(145) Liang, Y.; Meinhardt, T.; Jarre, G.; Ozawa, M.; Vrdoljak, P.; Schoell, A.; Reinert, F.; Krueger, A., Deagglomeration and Surface Modification of Thermally Annealed Nanoscale Diamond. *J. Colloid Interface Sci.* **2011**, *354* (1), 23-30.

(146) Hoh, H. Y.; Loh, K. P.; Sullivan, M. B.; Wu, P., Spatial Effect of C-H Dipoles on the Electron Affinity of Diamond (100)-2x1 Adsorbed with Organic Molecules. *Chemphyschem* **2008**, *9* (9), 1338-1344.

(147) Hossain, M. Z.; Aruga, T.; Takagi, N.; Tsuno, T.; Fujimori, N.; Ando, T.; Nishijima, M., Diels-Alder Reaction on the Clean Diamond (100) 2 X 1 Surface. *Japanese Journal of Applied Physics Part 2-Letters* **1999**, *38* (12B), L1496-L1498.

(148) Wang, G. T.; Bent, S. F.; Russell, J. N.; Butler, J. E.; D'Evelyn, M. P., Functionalization of Diamond(100) by Diels-Alder Chemistry. *J. Am. Chem. Soc.* **2000**, *122* (4), 744-745.

(149) Hoh, H. Y.; Ouyang, T.; Sullivan, M. B.; Wu, P.; Nesladek, M.; Loh, K. P., A Hreels and Dft Study of the Adsorption of Aromatic Hydrocarbons on Diamond (111). *Langmuir* **2010**, *26* (5), 3286-3291.

(150) Ouyang, T.; Gao, X. Y.; Qi, D. C.; Wee, A. T. S.; Loh, K. P., Cycloadditions on Diamond(100) 2x1: Observation of Lowered Electron Affinity Due to Hydrocarbon Adsorption. *J. Phys. Chem. B* **2006**, *110* (11), 5611-5620.

(151) Qi, D. C.; Liu, L.; Gao, X. G.; Ouyang, T.; Chen, S.; Loh, K. P.; Wee, A. T. S., Tuning the Electron Affinity and Secondary Electron Emission of Diamond (100) Surfaces by Diels-Alder Reaction. *Langmuir* **2007**, *23* (19), 9722-9727.

(152) Qi, D. C.; Gao, X. Y.; Wang, L.; Chen, S.; Loh, K. P.; Wee, A. T. S., Tailoring the Electron Affinity and Electron Emission of Diamond (100) 2 X 1 by Surface Functionalization Using an Organic Semiconductor. *Chem. Mater.* **2008**, *20* (21), 6871-6879.

(153) Jarre, G.; Liang, Y.; Betz, P.; Lang, D.; Krueger, A., Playing the Surface Game-Diels-Alder Reactions on Diamond Nanoparticles. *Chem. Commun.* **2011**, *47* (1), 544-546.

(154) Lang, D.; Krueger, A., The Prato Reaction on Nanodiamond: Surface Functionalization by Formation of Pyrrolidine Rings. *Diamond Relat. Mater.* **2011**, *20* (2), 101-104.

(155) Barras, A.; Lyskawa, J.; Szunerits, S.; Woisel, P.; Boulcherroub, R., Direct Functionalization of Nanodiamond Particles Using Dopamine Derivatives. *Langmuir* **2011**, *27* (20), 12451-12457.

(156) Kalgutkar, A. S.; Crews, B. C.; Marnett, L. J., Design, Synthesis, and Biochemical Evaluation of N-Substituted Maleimides as Inhibitors of Prostaglandin Endoperoxide Synthases. *J. Med. Chem.* **1996**, *39* (8), 1692-1703.

- (157) Pentecost, A.; Gour, S.; Mochalin, V.; Knoke, I.; Gogotsi, Y., Deaggregation of Nanodiamond Powders Using Salt- and Sugar-Assisted Milling. *Acs Appl Mater Inter* **2010**, *2* (11), 3289-3294.
- (158) Peng, W.; Mahfouz, R.; Pan, J.; Hou, Y. F.; Beaujuge, P. M.; Bakr, O. M., Gram-Scale Fractionation of Nanodiamonds by Density Gradient Ultracentrifugation. *Nanoscale* **2013**, *5* (11), 5017-5026.
- (159) Douglas, J. D.; Griffini, G.; Holcombe, T. W.; Young, E. P.; Lee, O. P.; Chen, M. S.; Frechet, J. M. J., Functionalized Isothianaphthene Monomers That Promote Quinoidal Character in Donor-Acceptor Copolymers for Organic Photovoltaics. *Macromolecules* **2012**, *45* (10), 4069-4074.
- (160) Bennett, A. E.; Rienstra, C. M.; Auger, M.; Lakshmi, K. V.; Griffin, R. G., Heteronuclear Decoupling in Rotating Solids. *J. Chem. Phys.* **1995**, *103* (16), 6951-6958.
- (161) Sakellariou, D.; Lesage, A.; Emsley, L., Spectral Editing in Solid-State Nmr Using Scalar Multiple Quantum Filters. *J. Magn. Reson.* **2001**, *151* (1), 40-47.
- (162) Blanc, F.; Coperet, C.; Lesage, A.; Emsley, L., High Resolution Solid State Nmr Spectroscopy in Surface Organometallic Chemistry: Access to Molecular Understanding of Active Sites of Well-Defined Heterogeneous Catalysts. *Chem. Soc. Rev.* **2008**, *37* (3), 518-526.

- (163) Kuznetsov, V. L.; Chuvilin, A. L.; Butenko, Y. V.; Malkov, I. Y.; Titov, V. M., Onion-Like Carbon from Ultra-Disperse Diamond. *Chem. Phys. Lett.* **1994**, 222 (4), 343-348.
- (164) Petit, T.; Arnault, J.-C.; Girard, H. A.; Sennour, M.; Bergonzo, P., Early Stages of Surface Graphitization on Nanodiamond Probed by X-Ray Photoelectron Spectroscopy. *PhRvB* **2011**, 84 (23).
- (165) Cebik, J.; McDonough, J. K.; Peerally, F.; Medrano, R.; Neitzel, I.; Gogotsi, Y.; Osswald, S., Raman Spectroscopy Study of the Nanodiamond-to-Carbon Onion Transformation. *Nanotechnology* **2013**, 24 (20).
- (166) Munirasu, S.; Albuerno, J.; Boschetti-de-Fierro, A.; Abetz, V., Functionalization of Carbon Materials Using the Diels-Alder Reaction. *Macromol. Rapid Commun.* **2010**, 31 (6), 574-579.
- (167) Mochalin, V.; Osswald, S.; Gogotsi, Y., Contribution of Functional Groups to the Raman Spectrum of Nanodiamond Powders. *Chem. Mater.* **2009**, 21 (2), 273-279.
- (168) Ishida, H.; Wellinghoff, S. T.; Baer, E.; Koenig, J. L., Spectroscopic Studies of Poly[N,N'-Bis(Phenoxyphenyl)Pyromellitimide] .1. Structures of the Polyimide and 3 Model Compounds. *Macromolecules* **1980**, 13 (4), 826-834.
- (169) Xiao, S. J.; Brunner, S.; Wieland, M., Reactions of Surface Amines with Heterobifunctional Cross-Linkers Bearing Both Succinimidyl Ester and Maleimide for Grafting Biomolecules. *J. Phys. Chem. B* **2004**, 108 (42), 16508-16517.

- (170) Panich, A. M.; Aleksenskii, A. E., Deaggregation of Diamond Nanoparticles Studied by Nmr. *Diamond Relat. Mater.* **2012**, 27-28, 45-48.
- (171) Fang, X.; Mao, J.; Levin, E. M.; Schmidt-Rohr, K., Nonaromatic Core-Shell Structure of Nanodiamond from Solid-State Nmr Spectroscopy. *J. Am. Chem. Soc.* **2009**, 131 (4), 1426-1435.
- (172) Espinas, J.; Pelletier, J. D. A.; Abou-Hamad, E.; Emsley, L.; Basset, J. M., A Silica-Supported Double-Decker Silsesquioxane Provides a Second Skin for the Selective Generation of Bipodal Surface Organometallic Complexes. *Organometallics* **2012**, 31 (21), 7610-7617.
- (173) Samantaray, M. K.; Callens, E.; Abou-Hamad, E.; Rossini, A. J.; Widdifield, C. M.; Dey, R.; Emsley, L.; Basset, J. M., Wme6 Tamed by Silica: Si-O-Wme5 as an Efficient, Well-Defined Species for Alkane Metathesis, Leading to the Observation of a Supported W-Methyl/Methylidyne Species. *J. Am. Chem. Soc.* **2014**, 136 (3), 1054-1061.
- (174) Chen, Y.; Callens, E.; Abou-Hamad, E.; Merle, N.; White, A. J. P.; Taoufik, M.; Coperet, C.; Le Roux, E.; Basset, J. M., [(Sio)(Tacl2me2)-Cl-V]: A Well-Defined Silica-Supported Tantalum(V) Surface Complex as Catalyst Precursor for the Selective Cocatalyst-Free Trimerization of Ethylene. *Angew. Chem., Int. Ed.* **2012**, 51 (47), 11886-11889.
- (175) Abou-Hamad, E.; Kim, Y.; Wagberg, T.; Boesch, D.; Aloni, S.; Zettl, A.; Rubio, A.; Luzzi, D. E.; Goze-Bac, C., Molecular Dynamics and Phase Transition in One-

Dimensional Crystal of C-60 Encapsulated inside Single Wall Carbon Nanotubes. *ACS Nano* **2009**, 3 (12), 3878-3883.

(176) Talapin, D. V.; Lee, J. S.; Kovalenko, M. V.; Shevchenko, E. V., Prospects of Colloidal Nanocrystals for Electronic and Optoelectronic Applications. *Chem. Rev.* **2010**, 110 (1), 389-458.

PUBLICATIONS

- Omar El Tall, **Yuan-Fang Hou** (co-first author), Edy Abou-Hamad, Inam U. Raja, Mohamed Hedhili, Wei Peng, Remi Mahfouz, Osman M. Bakr, Pierre M. Beaujuge, Direct Functionalization of Nanodiamonds with Maleimide. *Chemistry of Materials*, **2014**, 26 (9): 2766-2769.
- Wei Peng, Remi Mahfouz, Jun Pan, **Yuan-Fang Hou**, Pierre M. Beaujuge, Osman M. Bakr, Gram-Scale Fractionation of Nanodiamonds by Density Gradient Ultracentrifugation. *Nanoscale*, **2013**, 5: 5017-5026.
- Yang-Qin Gao, **Yuan-Fang Hou**, Pierre M. Beaujuge, Arrays of Hollow Silica Half-Nanospheres via the Breath Figure Approach. *Advanced Materials Interfaces*, **2015**, 2 (9).
- Andreas Ringk, Adrien Lignie, **Yuanfang Hou**, Husam N. Alshareef, and Pierre M. Beaujuge, Electropolymerized Star-Shaped Benzotrithiophenes Yield π -Conjugated Hierarchical Networks with High Areal Capacitance. *Submitted*.
- Adrien Lignie, Andreas Ringk, **Yuanfang Hou**, Jannic Wolf, Husam N. Alshareef, and Pierre M. Beaujuge, Thioether-substituted poly(*p*-phenylene)s for high power density electrochemical supercapacitors. *Submitted*.
- **Yuanfang Hou**, Andreas Ringk, Adrien Lignie, Husam N. Alshareef, and Pierre Beaujuge, How Doping Influences EDOT and its Derivative's Electrochemical Properties – the role of anions in the Electropolymerization process. *In preparation*.
- **Yuanfang Hou**, Andreas Ringk, Adrien Lignie, Husam N. Alshareef, and Pierre Beaujuge, Dendrimer-like 9,9'-Spirobi[9H-fluorene] 3, 4-Ethylenedioxythiophene Derivative as Crosslinker in the co-Electropolymerization of EDOT. *In preparation*.